Technical University of Denmark

DTU

Cu2ZnSnS4 Nanoparticle Absorber Layers for Thin-Film Solar Cells

Engberg, Sara Lena Josefin; Schou, Jørgen; Lam, Yeng Ming

Publication date:
2016

Document Version
Publisher's PDF, also known as Version of record

[Link back to DTU Orbit](#)

DTU Library
Technical Information Center of Denmark

Cu_2ZnSnS_4 Nanoparticle Absorber Layers for Thin-Film Solar Cells

by

Sara Lena Josefin Engberg

DTU Fotonik
Department of Photonics Engineering

Main supervisor: Senior scientist, dr. scient. Jørgen Schou
Co-supervisor: Professor Yeng Ming Lam
Submitted: October 14, 2016

Summary (English)

In the search for a new material for solar cells, the quaternary chalcogenide copper zinc tin sulfide (Cu_2ZnSnS_4 or CZTS) is one potential candidate. It is abundant, environmentally-friendly, inexpensive, and presently it has a mediocre record efficiency of around 10% with potential to reach above 15%.

This thesis is a part of the work done in making the prospects of solution-processed CZTS more fruitful. In addition to an inexpensive material, a cheap production pathway is also required for the material to be suitable for solar cells of the future. Solution-processing comprises either a nanoparticle ink or a precursor ink that can be printed, sprayed, or in another way coated on a substrate appropriate for mass production. For CZTS, the power conversion efficiency of these device are lagging behind the vacuum processed CZTS thin films, as certain challenges arise with solution-processing. The conversion of the as-deposited amorphous or nanocrystalline thin films into an almost "monocrystalline" material is not effective under the current sulfurization conditions.

In this work, means have been taken to improve the properties of the nanoparticles in order to make them easier to handle and better for the succeeding sulfurization step. For this objective, two main routes have been pursued. The first route was related to synthesizing larger nanoparticles than the typical outcome of the synthesis route used, as these could be a better starting material for grain growth. This was achieved by utilizing a two-step hot-injection method for synthesizing nanoparticles; it adds an extra step, but the desired particle sizes and particle size distributions were obtained. The second track concerned developing a type of nanoparticles without any hydrocarbon surface coatings, as these organic ligands have been challenging to remove in the succeeding annealing steps. By choosing suitable solvents and precursors, organic ligand-free nanoparticles were successfully synthesized in a facile one-step process. These particles further introduced the advantage that they could be dispersed in simple solvents such as water and ethanol.

To understand what happens to the as-synthesized material when it is heated, a range of analyses were carried out with some slightly uncommon techniques

for the field of CZTS: thermogravimetric analysis coupled with mass spectrometry. This characterization resulted in knowledge of how solvents and ligands evaporate or decompose as a function of temperature.

The final part of the work has been related to fabricating a thin-film absorber layer from the CZTS nanoparticles. It is a common obstacle that grain growth in these CZTS nanoparticle thin films is severely restricted, as the absorber layer remains very porous or an organic layer is present at the back interface, which was also seen here. Sodium in the form of NaCl salt was for the first time dissolved directly in the nanoparticle ink - again with focus on environmental friendliness and a low cost. The addition of sodium had a significant impact, and it greatly enhanced both structural and optoelectronic properties of the films.

Summary (Danish)

Denne ph.d. afhandling handler om materialet Cu_2ZnSnS_4 (CZTS) som består af de almindeligt forekommende og miljøvenlige elementer: kobber, zink, tin og svovl. CZTS skal bruges i lavteknologiske solceller, der forhåbentlig vil blive billigere end silicium-solceller i fremtiden. Udover et billigt materiale, er det også nødvendigt med en billig fremstillingsmetode. Med vådkemisk deponering er det muligt at spraye, printe, eller på andre måder coate store overflader, hvilket gør metoden egnet til industriel brug. Denne afhandling handler netop om fabrikation af CZTS tyndfilm ved vådkemisk deponering.

Det første trin i processen er at fremstille den "blæk", som skal bruges til deponering. Denne blæk kan enten bestå af CZTS nanopartikler eller en blanding af Cu-, Zn-, Sn- og S-salte i det rigtige forhold. Fokus i dette arbejde har været på at syntetisere CZTS nanopartikler med den rigtige sammensætning og med forskellige fysiske egenskaber. Det er blandt andet lykkedes os at lave CZTS nanopartikler der kan opløses i miljøvenlige opløsningsmidler så som vand og ethanol.

Den færdige blæk bliver efterfølgende deponeret enten gennem spray-coating, doctor blading eller drop-casting. Derefter skal tyndfilmene varmes op, så nanopartiklerne vokser sammen til større korn, da ladningstransporten i materialet formindskes, hver gang en elektron støder på en korngrænse. Denne kornvækst-proces er blevet undersøgt grundigt, da det ikke var tilstrækkeligt at sintre materialet ved en høj temperatur. Vi opdagede, at det ved at tilsætte natrium til blækken, var muligt at opnå den ønskede struktur i materialet. Desuden forbedredes materialets photoluminiscens væsentligt, hvilket betyder færre defekter hvor elektroner og huller kan rekombinere.

De første solceller er fremstillet, men kun for tyndfilm uden ekstra natrium tilsat. Disse film var stadig for porøse til, at effektive solceller kunne produceres.

PREFACE

This thesis is submitted as a partial fulfilment of the requirements to obtain a Ph.D. degree at the Technical University of Denmark (DTU). Most work was carried out at the Risø campus in The Optical Microsensors & Micromaterials (MIKRO) group, but part of the work was also done at Nanyang Technological University (NTU) in Singapore. The work started August 15, 2013, and ended October 14, 2016. The main supervisor has been senior scientist, dr. scient. Jørgen Schou from DTU Fotonik, together with co-supervisor professor Yeng Ming Lam from NTU.

The PhD project was part of the CHALSOL (Chalcogenide solar cell) project, which was funded by The Danish Council for Strategic Research with 16 Mdkkr or 2 M€. The aim of this project was to develop record efficiency devices and aid in the understanding of the charge-carrier physics of chalcogenide solar cells of CZTS by producing thin films by vacuum processing and wet-chemistry. It was one of the first project working with pulsed laser deposition (PLD) of thin-film solar cell absorber materials. The project was led by Jørgen Schou, in collaboration with professor Ole Hansen at DTU Nanotech, professor Nini Pryds at DTU Energy, and professor Peter Uhd Jepsen at DTU Fotonik. Two international partners were also participating: professor Yeng Ming Lam and professor Rafal Dunin-Borkowski at the Ernst Ruska Center in Julich, as well as one industrial partner, Ken Jensen, from Dansk Solenergi AS.

This PhD thesis is the outcome of the solution-processing track of the CHALSOL project. The initial end-goal was to fabricate a solar cell with a 4% efficiency by spray-coating. Other milestones included: (1) measuring a conversion efficiency from solution-processed CZTS solar cells, (2) producing the first CZTS films through spray-coating at DTU Fotonik, and (3) measuring a conversion efficiency from a spray-coated CZTS solar cell. The project Gantt chart is displayed in Appendix A, where also a list of all milestones is given.

At the start of this project, the MIKRO-group had no experience in either solar cell fabrication or solution-processing. During the preceding three years, the pipeline for solar cell production has been established. Regarding this, I have been responsible for setting up the chemistry lab and involved in building the

sulfurization oven.

Outline of this thesis

The main research in this work was divided into nanoparticle synthesis, thermal analysis of nanoparticle inks and powders, and sulfurization. The chapters on thin-film deposition and solar cells should be considered as an introduction to the field. Each chapter is built up with a general background and a description of the experimental procedure, followed by results, discussion, and an outlook section.

Chapter 1: Background   This chapter introduces the reader to the field of thin-film solar cells and solution processing, and in particular the material CZTS. The motivation behind the work including current advantages and challenges are presented. Physical properties of CZTS that are relevant for the succeeding chapters will also be introduced.

Chapter 2: Synthesis of Cu_2ZnSnS_4 Nanoparticles   In this chapter, nanoparticle synthesis is covered. The methods used are called the one-pot method and the hot-injection method. Phase evolution and particle size distribution are characterized, but the objective is mostly to obtain a suitable elemental composition. This chapter is restricted to syntheses that can be reproducibly prepared, so that rational adjustment of experimental conditions applies, along with a few comments on failed attempts.

Chapter 3: Thermal Analysis of Cu_2ZnSnS_4 Nanoparticles and Inks   This chapter contains thermal characterizations of nanoparticle inks and powders that aid in the understanding of what goes on during annealing. Thermal analysis describes how properties of materials change with temperature, and here we monitor the mass, heat flow, and crystallinity in different atmospheres. As an additional characterization tool, mass spectrometry is used for detection of volatile species leaving the sample.

Chapter 4: Thin-Film Deposition   The purpose of this chapter is to serve as an introduction to thin-film deposition. This chapter briefly presents the deposition techniques used to form thin films with a thickness of about 1 μm via solution-processing, including a description of the experimental setups, and general results and observations. Finally, ideas on how to improve the reproducibility of these coating methods will be given.

Chapter 5: Sulfurization of Solution-processed Cu$_2$ZnSnS$_4$ Thin Films   This chapter concerns sulfurization of CZTS nanoparticle and precursor thin films. The objective is to achieve a dense absorber with micron-sized grains. We found that the nanoparticle systems were very challenging to sinter, as a high temperature was not sufficient to start the sintering process. We solved this by eliminating the organic ligands that impeded the merging of the nanoparticles and by including a liquid-phase additive during annealing to enhance grain growth.

Chapter 6: Photovoltaic Behaviour of Solution-processed Cu$_2$ZnSnS$_4$ Thin–Film Devices   In this chapter, a few CZTS thin-film solar cells will be briefly presented. A useful measure to determine the quality of the bare absorber layers is photoluminescence (PL). We found that the annealed ligand-free CZTS nanoparticle thin films exhibited a high PL signal when sodium was included, which indicates that radiative recombination is dominating, and thus fewer defect states exist.

Chapter 7: Conclusion   Here, the main findings will be collected, as well as suggestions to what should be done next.

Risø, October 2016

Sara Lena Josefin Engberg

Acknowledgements

There are many people I would like to thank for their participation in my project during the last three years. First of all, my main supervisor, Jørgen Schou, for the opportunity to carry out this work and for encouraging me no matter how things were looking. I know I have had a lot of demands, and I appreciate his time and consideration. I am also very thankful to Jørgen that he sent me to a wide range of conferences, both in Europe and in the US. This is where I learned what other groups were working with, what their challenges were, and this is where I got most ideas of which direction I wanted this PhD project to go.

I would also like to acknowledge my co-supervisor, professor Yeng Ming Lam, for always being very pro-active and eager to try out new things. It definitely influenced me whenever we got the chance to meet.

My fellow PhD student, Andrea Crovetto, has been a huge help, and I want to thank him for always prioritizing my samples for characterization, for spreading joy during CdS-deposition, and for completing the devices (and also all the Master and Bachelor students who worked with him: Edo, Philip, Tobias, Tomas, and Lasse).

I was fortunate to get the chance to collaborate with Naghmeh Mirbagheri during some months in 2015. It was a great experience to work together with her, and the synthesized nanoparticles really were a turning point for my PhD.

One of the best times research-wise was while I spent my external stay in Singapore. During this time, I want to thank Zhenggang Li and Jun Yan Lek at NTU for their friendship and for teaching me the hot-injection method; for making me feel at home in Singapore while at the same time helping me on the right track in my research. In particular, I am grateful to Zhenggang for characterizing all the nanoparticles I synthesized, and for completing and measuring the solar cells we prepared.

The colleagues I worked the closest with on a daily basis are the MIKRO-group members, and I feel truly lucky for each one of them. I want to thank my fellow PhD students Andrea Cazzaniga and Rebecca Bolt Ettlinger, for making me question everything I do, and for making everything fun. I also appreciate

LIST OF PUBLICATIONS

PUBLICATIONS INCLUDED IN THIS THESIS

[Paper I] Sara Engberg, Zhenggang Li, Jun Yan Lek, Yeng Ming Lam, and Jørgen Schou. Synthesis of large CZTSe nanoparticles through a two-step hot-injection method. *RSC Advances.* 2015, 5, 96593.

[Paper II] Naghmeh Mirbagheri, Sara Engberg, Andrea Crovetto, Søren B. Simonsen, Ole Hansen, Yeng Ming Lam, and Jørgen Schou. Synthesis of ligand-free CZTS nanoparticles via a facile hot injection route. *Nanotechnology.* 2016, 27, 185603.

[Paper III] Sara Engberg, Karsten Agersted, Andrea Crovetto, Ole Hansen, Yeng Ming Lam, and Jørgen Schou. Investigation of CZTS nanoparticle inks for thin-film solar cell applications. *Submitted.* 2016.

[Paper IV] Sara Engberg, Andrea Crovetto, Stela Canulescu, Ole Hansen, Yeng Ming Lam, and Jørgen Schou. Na-assisted grain growth in CZTS nanoparticle thin films for solar cell applications. *Submitted.* 2016.

PUBLICATIONS NOT INCLUDED IN THIS THESIS

[Paper V] Visweswara Chakravarthy Gudla, Kirill Bordo, Sara Engberg, Kristian Rechendorff, and Rajan Ambat. High frequency pulse anodising of magnetron sputtered Al–Zr and Al–Ti Coatings. *Materials & Design.* 2016, 95, 340-347.

[Paper VI] Martin Aggerbeck, Stela Canulescu, Kai Dirscherl, Villads E. Johansen, Sara Engberg, Jørgen Schou, and Rajan Ambat. Appearance of anodised aluminium: Effect of alloy composition and prior surface finish. *Surface and Coatings Technology.* 2014, 254, 28-41.

XII

CONFERENCE CONTRIBUTIONS

[C.1] Sara Engberg, Naghmeh Mirbagheri, Søren Bredmose Simonsen, Yeng Ming Lam, Jørgen Schou. *Large CZTS Nanoparticles Synthesized by Hot-injection for Thin Film Solar Cells.* Oral presentation at 2016 E-MRS Spring Meeting, Lille, France.

[C.2] Sara Engberg, Karsten Agersted, Andrea Crovetto, Ole Hansen, Yeng Ming Lam, Jørgen Schou. *Thermal analysis of CZTS nanoparticles and inks.* Poster presented at 2016 E-MRS Spring Meeting, Lille France.

[C.3] Sara Engberg Yeng Ming Lam, Jørgen Schou. *Optimized Packing Density of Large CZTS Nanoparticles Synthesized by Hot-injection for Thin Film Solar Cells.* Poster presented at 2015 MRS Spring Meeting, San Francisco, California, United States.

[C.4] Sara Engberg, Yeng Ming Lam, Jørgen Schou. *Large CZTS Nanoparticles Synthesized by Hot-Injection for Thin Film Solar Cells.* Poster presented at 2015 E-MRS Spring Meeting, Lille, France.

[C.5] Sara Engberg, Naghmehalsadat Mirbagheri, Andrea Crovetto, Edoardo Bosco, Ole Hansen, Jørgen Schou. *Spray-coated CZTS Nanoparticles in Water for Environmetnally-friendly, Inexpensive Solar Cell Absorber Material.* Poster presented at DTU Sustain Conference 2015, Lyngby, Denmark.

[C.6] Sara Engberg, Andrea Crovetto, Bosco, Edoardo; Rasmussen, Philip; Ole Hansen, Jørgen Schou. *Annealing in Sulfur of Doctor Bladed CZTS Nanoparticles.* 2014. Poster presented at 5th European Kesterite Workshop, Tallinn, Estonia.

[C.7] Sara Engberg, Zhenggang Li, Yeng Ming Lam, Jørgen Schou. *Controlling the Ratio of CZTS to CZTSe Nanocrystals by Hot Injection of Selenium.* 2014. Poster presented at 29th of the European Photovoltaic Energy Conference and Exhibition, Amsterdam, Netherlands.

[C.8] Sara Engberg, Andrea Crovetto, Ole Hansen, Jørgen Schou. *Study of Grain Growth of CZTS Nanoparticles Annealed in Sulfur Atmosphere.* Poster presented at DTU Sustain Conference 2014. Lyngby, Denmark.

CONTENTS

SUPER-SHORT INTRODUCTION TO SOLAR CELLS

This page is a very basic introduction to solar cells, and the terminology used in this field will be presented. The central part of a solar cell is a p-n junction, *i.e.* a junction between a material that has a Fermi energy below the the middle of the band gap and a material that has a Fermi energy above the middle of the band gap. The former material has a surplus of free holes, *i.e.* it lacks electrons, and the latter material has a surplus of free electrons. When these two materials are brought into contact, the Fermi energy will align, and close to the junction the valence and conduction bands will bend accordingly (Fig. I(a)). This in turn creates an electrostatic field across the junction - the depletion region, which allows carriers to drift under illumination. If the band gaps of the materials are suitable for light absorption, *i.e.* absorb irradiation with wavelengths up to the short end of infrared spectrum, and if the materials in other ways satisfy the requirements for photovoltaic activity, for example, that it can be produced with few defects and with a small amount of secondary phases, a solar cell can be formed by connecting the p-n junction to an external circuit.

For *thin-film solar cells*, direct band gap materials with high absorption coefficients are used as either the p- or the n-type material, as only a film of a thickness around 1 μm is required to absorb enough light. This layer is called the *absorber*, as its purpose is to absorb all light. The n-type layer consists of the *buffer* and the transparent conductor, and its function is to provide the interface for the p-n junction. Fig. I(b) displays a typical solar cell architecture for a thin-film solar cell.

This thesis is about the absorber material.
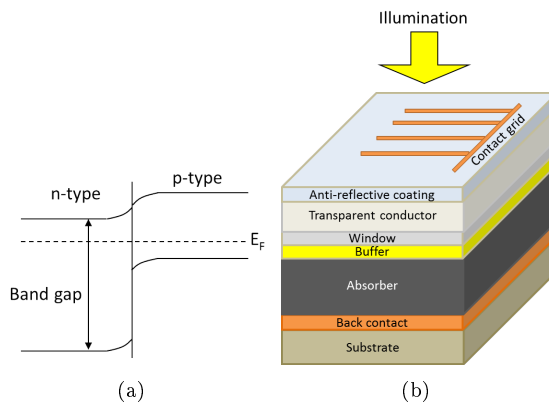
Figure I: Schematics (a) of p-n junction, where V_{OC} is the maximum voltage that can be generated in the solar cell, and a model (b) of typical thin-film solar cell structure.

CHAPTER 1

BACKGROUND

The goal of this chapter is to introduce the reader to the field of thin-film solar cells and in particular the material CZTS. The motivation behind the work including current advantages and challenges are presented. Physical properties of CZTS that are relevant for the succeeding chapters will also be introduced. The chapter is concluded with a description of the solution-processing method.

1.1 SOLAR ENERGY

The Earth is not an isolated system; human actions can perturb the equilibrium state we are in, and eventually bring us out of balance. Our modern lifestyle would not be possible without energy for producing and preparing food, reading books in the dark at night, working on solving problems in medicine, and research at the university. As living standards increase, more people can afford to buy meat, cars, flight tickets, and all of which requires energy. *"We have gone from being a small world on a large planet, to a large world on a small planet"*, as Johan Rockström put it. Any kind of man-made change can influence parameters we often think of as constant, such as the Earth's environment, temperature, sea water level, and biodiversity, and thereby destabilize this planet. Taking all parameters into account results in an extremely complicated system and simplified models are necessary to make predictions of the future. One such model is the concept of planetary boundaries - an attempt to create a safe operating space for global civilizations [1, 2]. Rockström *et al.* identify and assess the main fields of change within the Earth system, and define related biophysical thresholds that should protect humanity from disastrous consequences. According to the UN, the solution to avoid these disasters is named "sustainability" and sustainable development comprises "*development which meets the needs of the present without compromising the ability of future generations to meet their own needs*" [3]. We need energy, but from sustainable sources like solar energy.

1.1.1 PRESENT STATUS AND FUTURE PROSPECTS OF SOLAR ENERGY

Solar energy is the only form of renewable energy that by itself can provide for the growing energy demand of the future [4, 5]. It has great potential as it is basically unlimited, and therefore well worth exploring. The compound annual growth rate (CAGR) of solar cell installations has grown by 41% from 2000 to 2015 [6]. In 2015, the price for solar energy in Southern and Central Europe was 5-8 €c/kWh, and depending on annual sunshine, power cost of 4-6 €c/kWh are expected by 2025, reaching 2-4 €c/kWh by 2050 according to a conservative estimate [7].

Today, silicon (Si) solar cells is the leading commercial photovoltaic (PV) technology. The reasons for this are high efficiency and low cost due to its high abundance on earth, low toxicity, and well-established production methods. A new report suggests that by 2040, 35% of the extra installed electricity generated will be solar energy [8]. Whether Si technology is the ultimate PV solution to lead the industry through this growth is arguable [9], and there are many alternative PV materials such as CdTe, $CuIn_xGa_{1-x}Se_2$ (CIGS), organic, dye-sensitized, and the up-and-coming perovskites.

An important measure when comparing solar cell technologies is the energy pay-back time (EPBT). The PV modules produce environmentally-friendly electricity, without polluting, without emitting greenhouse gases, and without utilizing fossil fuels, but energy and resources go into making the modules. The EPBT accounts for the time it takes the solar cell to generate the energy required to produce the PV system, and is therefore a time frame of how long the module needs to be working to pay back and be worthy of the investment. The EPBT depends on the geographical location, and for multi-crystalline Si it is around 2.5 years in Northern Europe versus 1.5 years or below in Southern Europe. For such a solar cell with a 2 year EPBT and a 20 year lifetime, the PV module can generate ten times the energy needed to fabricate it. Certain PV technologies even have a lifespan of 30 years and an EPBT of 0.7 years at some locations [6]. The family of solar cells called *thin-film solar cells* have a lower EPBT than Si solar cells [10], which makes them a good alternative for future needs.

1.1.2 THE AREA OF THIN-FILM SOLAR CELLS

From a materials-saving perspective, *thin-film solar cells* are appropriate as they only need a thickness of around 1 μm for sufficient light absorption. The first thin-film solar cells were developed in the 1960s, and consisted of either $Cu_{2-x}S/CdS$, $Cu_{2-x}Te/CdTe$, or CdS/CdTe, with power conversion efficiencies up to 6%. In 1977, the first $CuInSe_2$ (CIS)/CdS solar cell was fabricated with an efficiency of 4-5%. In 1994, 9.7% efficiency was achieved with a In_2O_3/CdS/CIS structure, and in 1997 it was found that alloying CIS with a small amount of

Ga would improve the efficiency to over 10% efficiency. This finding was the start of the CIGS material research.

Within the last 20 years, six thin-film solar cell materials have achieved an efficiency, η, higher than 10%: CdTe ($\eta = 22.1\%$), CIGS ($\eta = 22.6\%$), CuInGaS$_2$ ($\eta = 13\%$), GaAs ($\eta = 28.8\%$), Cu$_2$ZnSn(S$_x$Se$_{1-x}$)$_4$ (CZTSSe) ($\eta = 12.6\%$), and Cu$_2$ZnSnSe$_4$ (CZTSe) ($\eta = 11.6\%$), whereof the first three are on the PV market [11, 12, 13, 14].

This thesis concerns the quaternary material copper-zinc-tin-sulfide, Cu$_2$ZnSnS$_4$, abbreviated CZTS, *i.e.* it does not contain selenium. The interest in this material has increased rapidly in recent years, as can be seen from the number of publications in Fig. 1.1(a), compared to CIGS in (b).

(a)   (b)
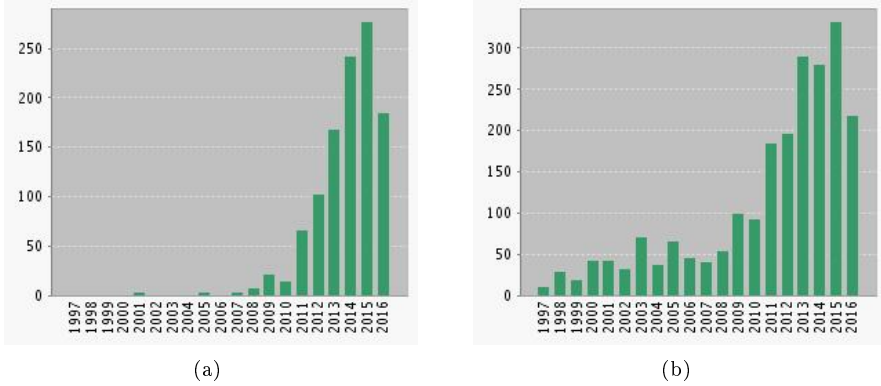
Figure 1.1: Number of published papers and patents on CZTSSe (a) and CIGS (b) within the last 20 years (taken from Web of Science [15]).

1.1.3 RECORD CZTS EFFICIENCIES THROUGHOUT TIME

The work on CZTS started around 1988, when Ito and Nakazawa synthesized the first CZTS solar cell [16]. From this point, the power conversion efficiency of CZTS solar cells has been constantly rising, and some selected device efficiencies are showed in Fig. 1.2 for various deposition methods. Squares mark that the CZTS absorber is deposited through solution-processing, and circles mark vacuum processing.

To shortly summarize the evolution since 1996, a few key discoveries will be mentioned: The group of Katagiri and co-workers made improvements within vacuum processing, increasing the efficiency of co-evaporated and sulfurized films [17, 18], and later by Schubert *et al.* [19]. In recent years, sputtering

Figure 1.2: Evolution of CZTS efficiencies for various deposition methods, where circles represent vacuum deposition and squares solution-processing.

has produced the champion CZTS devices [20, 21, 22], and applying a high-temperature annealing after CdS deposition has led to the current record of 9.4% [23]. Another technique which is being explored is pulsed laser deposition (PLD) [24], where an efficiency of 5% was recently achieved.

Progress has also been made for solution-processed CZTS solar cells made by wet-chemical means. In 1996, Nakayama and Ito made the first CZTS solar cell through spray pyrolysis and annealing in H_2S [25]. The first CZTS nanoparticle solar cell was produced in 2009 by Steinhagen *et al.* with an efficiency of 0.23% [26], and since then a few devices has been made with around 2% efficiency [27, 28, 29, 30]. In 2015, Liu *et al.* developed the current record device of 4.83% [31]. Another popular approach within solution-processing is utilizing a precursor ink, which has led to the highest efficiency for solution-processed CZTS films of 5.7% for metal salts in dimethyl-formamide and propanol [32], and 5.14% for milled precursors [33], and other devices at 5% for metal salts in ethanol and water [34, 35]. Of other techniques used, common ones include the sol-gel method [36, 37], electrodeposition [38, 39], combustion method [24], and sulfurization of binary and ternary nanoparticles [40].

1.1.3.1 INCLUSION OF SELENIUM

In literature, the abbreviation "CZTS" is interchangeably used for the quinary semiconductor CZTSSe. The record efficiency of the selenium-containing CZTSSe

is 12.6% and was fabricated through the hydrazine-mediated route [41]. Other solution-processed devices are also performing better when they contain both S and Se; the best nanoparticle device with an efficiency of 9.0% [42], the best precursor device with 8.6% (compared to 5% when annealed in only sulfur atmosphere) [43]. The record power conversion efficiency of the pure selenide CZTSe is 11.6% [14], and was fabricated by evaporation.

The reason why adding Se improves the efficiency could be explained by some of the differences between S and Se:

- CZTSe has a band gap of 0.95-1.05 eV [44], while CZTS has 1.45-1.51 eV [45], so by alloying the two, the band gap can be tuned according to the solar spectrum [43].
- The conventional device structure with CdS as the buffer layer, might work better with low-band gap materials [44].
- The size of Se (1.98 Å) is larger than S (1.84 Å), so when Se replaces S in the crystal lattice during annealing, a volume expansion occurs. This in turn leads to the elimination of voids and results in the formation of a dense film with fewer grain boundaries [46].
- Sulfur vacancies (V_S) have a significantly lower formation energy than selenium vacancies (V_{Se}), which gives rise to deep V_S donor defects in the sulfide compound [47].
- A lower population of isolated deep defect states in the form of Sn_{Zn} exist in CZTSe, and also lower electron trapping of $[2Cu_{Zn}+Sn_{Zn}]$ defect clusters in CZTSe when compared to CZTS [47].
- MoS_2 formation at the back contact during sulfurization [48], could be damaging the the solar cell performance [49, 50].

Nonetheless, since Se is toxic and more rare than S, the pure-sulfide CZTS should be more environmentally-friendly.

1.2 Physical properties of CZTS

CZTS is a chalcogenide material, which means that the anion is a chalcogen from Group 16 in the periodic table that includes oxygen, sulfur, selenium, tellurium, or polonium. It exists naturally on Earth as a mineral named kesterite, from which the crystal structure is also named [45].

1.2.1 Crystal structure

The periodic array of ordered elements makes up the crystal structure. CZTS exists in four different phases: stannite, kesterite, wurtz-stannite, and wurtz-kesterite, and an overview of differences between the stannite and kesterite structures can be found in Table 1.1. All crystal structures appear in the Inorganic

Crystal Structure Database (ICSD) [51], with X-ray diffraction (XRD) patterns determined from single-crystal XRD, and the phases are also confirmed by theoretical calculations. More information in the crystal structure can be found in the book *Copper Zinc Tin Sulfide-Based Thin-Film Solar Cells* [45].

Table 1.1: Overview of the four different crystal structures CZTS exists in, including total energy, experimental and theoretical band gap, crystal structure, cation ordering, and anion position [45, 44, 51, 52].

	Crystal structures	
	Kesterite	Stannite
Cation ordering ($z = 0, \frac{1}{4}, \frac{1}{2}, \frac{3}{4}$)	Tetragonal (Diamond) CuSn, CuZn, CuSn, CuZn	Tetragonal (Diamond) ZnSn, Cu_2, ZnSn, Cu_2
Energy (meV/atom)	0	2.8
Energy (meV/cell)	0	50
a (Å)	5.427	5.450
c (Å)	10.871	10.878
c/a	2.003	1.996
Band gap (exp.) (eV)	1.45-1.51	
Band gap (theo.) (eV)	1.47-1.65	1.27-1.42
Absorption coefficient (cm^{-1})	$> 10^4$	

The crystallographic unit cell is the smallest building block and it is different for the kesterite and stannite crystal structure. The relative difference lies in the cation position, where kesterite has Cu in each plane, while stannite has Zn-Sn at the $z = 0$ and $z = \frac{1}{2}$, and Cu_2 at the $z = \frac{1}{4}$ and $z = \frac{3}{4}$, (as described in Table 1.1). In both structures, Sn is located at the same site [45]. Density functional theory (DFT) calculations have given the total energy of the CZTS system for different crystal structures, and have showed that the kesterite crystal structure is the ground state, but stannite is only 2.8 meV/atom above it (wurtz-kesterite is 6.0 meV/atom and wurtz-stannite 7.2 meV/atom are of the Lonsdaleite family, with monoclinic and ortorombic structure, respectively). This means that kesterite CZTS has a total energy per primitive cell that is 50 meV lower than the stannite CZTS, and kesterite is therefore slightly more stable. Kesterite will be formed under equilibrium growth conditions, but since the energy difference is small, both phases may coexist [44].

1.2.2   DEFECTS

High-efficiency CZTS devices are always off-stoichiometric with a composition that is Cu-poor (Cu/(Zn+Sn)<2) and Zn-rich (Zn/Sn> 1), while still maintaining the kesterite structure [22, 31, 33]. This can be realized from the formation of desired defects while avoiding unwanted ones and secondary phases. Especially Cu-on-Zn antisites (Cu_{Zn}) have very low formation energies, and are believed to be the main acceptor-defects responsible for the p-type conductivity of CZTS
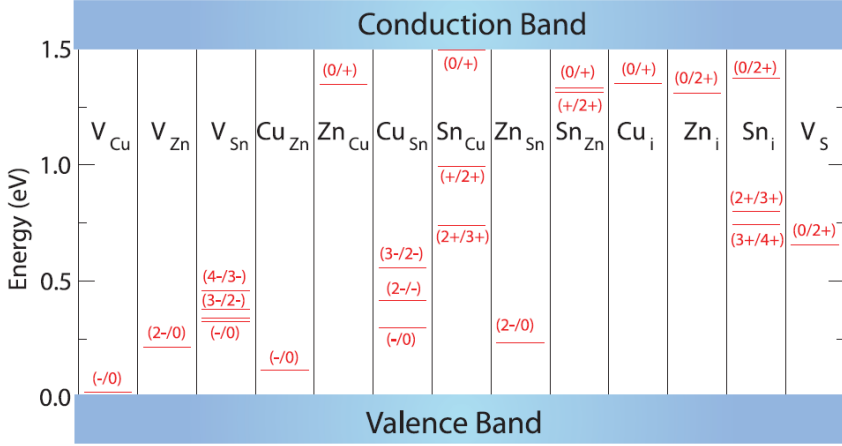
Figure 1.3: Calculated defect states in CZTS from Walsh *et al.* [53]. (Red numbers correspond to charge of defect).

[47]. An overview of possible defect state energies are displayed in Fig. 1.3. In particular, the defect cluster $[2Cu_{Zn}+Sn_{Zn}]$ induces electron-trapping states in the solar cell absorber, and its population increases dramatically when Zn becomes poor. This is why Cu-poor and Zn-rich conditions results in the higher solar cell efficiencies [47].

1.2.2.1 Cation ordering

Disordering among the Cu and Zn cations in the kesterite $z = 1/4$ and $z = 3/4$ layers can also occur. Disorder is caused by thermal fluctuations in the crystal lattice from the crystal being in a dynamic equilibrium. Scragg *et al.* investigated CZTS thin films with near-resonant Raman spectroscopy, and determined the order-disorder transition temperature to be $260°C \pm 10°C$ [54]. The order-disorder transition phenomenon has also been characterized by neutron diffraction where the heating/cooling rate was found to be important for the degree of ordering [55]. Different levels of ordering/disordering has been calculated to result in band gap variations in the order of 100 meV [56]. The effect ordering has on power conversion efficiency is not however clear, as different results have been reported.

1.2.3 Secondary phases

A popular way to present the composition is with the ternary phase diagram (Fig. 1.4), in which the sulfur concentration is kept constant. Very good compositional control is required to obtain the CZTS phase in the narrow phase
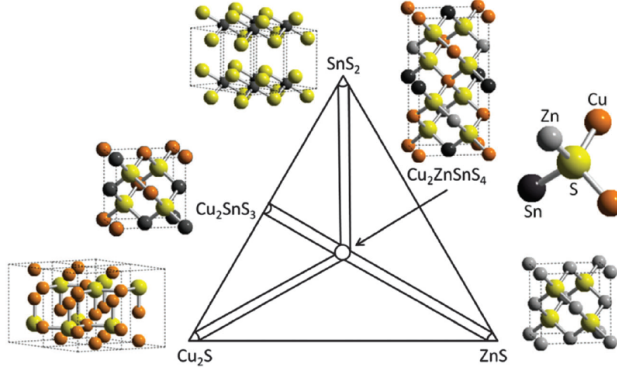
Figure 1.4: Ternary phase diagram illustrating the narrow region of interest where CZTS formation is favourable. Typical secondary phases are also illustrated. Figure from Du *et al.* [57].

Table 1.2: Selected physical properties for common secondary phases found in CZTS solar cells (inspired by [58, 59, 60]). *Indirect/direct.

	ZnS	Cu$_2$S	SnS	SnS$_2$	Cu$_2$SnS$_3$
Band gap (eV)	3.7	1.2	1.0/1.3*	2.5	0.9
Electrical behaviour	Insulator	p-type, metal like, highly defective	p-type	n-type	p-type
Impact on η	Insulating, reduces device active area	Metallic, creates shorts		Forms diodes and barriers for carrier collection	Affects carrier collection efficiency

region indicated in the center of the phase diagram, and secondary phases are very common. It is not always certain how a secondary phase affects the absorber layer and the solar cell performance, but some physical properties of secondary phases that are believed to be potentially present in CZTS solar cells are listed in Table 1.2.

1.2.4 CHALLENGES RELATED TO CZTS

The above sections have introduced defects, disorder and secondary phases in the Cu-Zn-Sn-S system, and the narrow phase region where CZTS is formed. A Cu-poor and Zn-rich composition is required for a high-efficiency solar cell absorber. Furthermore, there is consensus in literature that the low open-circuit

voltage, V_{OC} in all devices, is one main limitation for CZTS solar cells [61]. The loss in V_{OC} is explained by too much recombination.

1.3   Motivation behind CZTS thin-film solar cells

The optical properties of CZTS are one straightforward reason for further investigation. The absorption coefficient of 10^5 cm^{-1} of this direct band-gap material, results in that 99% of the light is absorbed within an absorption depth of 1 μm of the material. The band gap of 1.45-1.51 eV is close to the optimal value for a single junction solar cell, which was calculated by Schockley-Queisser to be 1.34 eV [62], and the maximum efficiency only varies a few percentages some tenth of an eV around this value.

Good optical properties are not enough to make a good p-type absorber for a solar cell. In addition to this, good band alignment, a high carrier mobility, and high carrier lifetime are also required [63], but since CZTS has a good resemblance to CIGS, it is believed that these properties can be tuned accordingly.

Furthermore, CZTS consists of abundant materials, which makes it comparably in-expensive, and environmentally-friendly. These features are explored further in the following sections.

1.3.1   Material abundance

Thin-film solar cells of CdTe and CIGS are already on the market and contain scarce materials. Indium and gallium are on the list of critical materials for the EU [64] and indium, gallium, and tellurium on a similar list in the U.S. [65]. The abundance of the elements is important to take into account when considering the long-term target of providing continued growth and cost reduction of solar energy installations in the future. For this, natural resource limitations could be bottlenecks that hamper the production. If all of the scarce materials reserves were used for solar cells in 2100, all current mature technologies (silicon, thin-film and concentrator solar cells) would only meet 2% (upper limit) of the predicted energy demand [66]. Particularly, the scarcity of indium and tellurium would limit scale-up of CdTe and CIGS and the scarcity of silver for electrodes would limit scale-up for silicon solar cells to terawatt level deployment [67]. Some do not believe material availability is a problem, at least as long as the demand and thus the price for indium and tellurium does not escalate severely [68, 69].

Estimating the world-wide availability of materials is tricky, and tellurium and indium are both by-products from mainly copper recovery and zinc production, respectively, but can also be mined from other minerals' ores as well. Data are gathered from countries' own assessments, company reports, trade journals, and

academic papers, and these are used to estimate the already known and yet to be found reserve volumes [69]. As the methods, assumptions and data in all scarcity assessment papers vary, uncertainty on whether material availability becomes a constraint arises. Nonetheless, a co-existence of different PV technologies would mitigate the risks related to dependency on only one type of solar cell structure, and choosing more abundant elements when developing this material has its advantages.

Copper, zinc, tin and sulfur are all considered abundant materials. The least abundant elements, Zn and Sn, are 1500 times and 45 times, respectively, more present in the earth's crust than In, and the price of In is almost two orders-of-magnitude higher than that of Zn and Sn [70].

1.3.2 ENVIRONMENTAL IMPACT

An operating solar cell does not cause any negative environmental impact, but there could however be greenhouse gas emission during manufacture, toxic materials included in the solar cell, and a high amount of energy and water consumed during manufacturing [68, 71].

Environmental impacts can be assessed from a life cycle analysis. This model considers all environmental impacts for a product's life span from cradle to grave, including raw material acquisition, material's processing, manufacture, distribution and usage, recycling and waste management [72]. One such study comparing the replacement of CIGS with CZTS, finds that the ecotoxicity would be significantly reduced by avoiding Ga [71]. However, for the current technologies the global warming effect, the water usage and the energy required for production are slightly higher for CZTS. These assessments should - just like the material availability assessments - be interpreted with caution, as many assumptions are used for the analysis.

Heavy-metals are of special concern because they can have a high ecotoxicity, and the typical CIGS and CZTS solar cells normally contain a CdS buffer layer. Cadmium is classified as carcinogenic and it is on the list of the ten chemicals with major public concern for the World Health Organization [73]. Cadmium could leak out into the environment either during fires or if the PV panels are abandoned as landfill. Tests have shown that 99.50-99.96% of the cadmium contained in a CdTe panel would be safely encapsulated during a fire, and that combining this with the risk of a residential fire in a wood-frame building in the US, the probability of cadmium emission is close to zero [74]. Also, landfill under controlled circumstances should not present a safety concern [68]. For CZTS solar cells, work is being done to replace CdS with an alternative inorganic buffer layer [75, 76, 77, 78], or even fullerenes [79], as CdS in true does not have the best band alignment to CZTS.

The highest environmental impact related to the absorber layer was found to be the total electricity used for fabrication [71]. More focus on improvement of the manufacturing process would therefore be the greatest contributor to decreasing the environmental impacts of these thin-film absorber materials, which is why solution-processing is of interest.
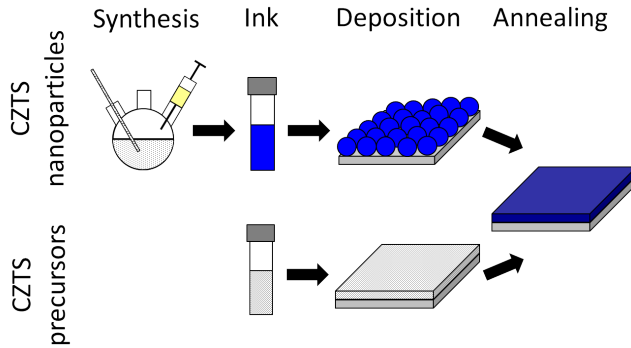

Figure 1.5: The CZTS solution-processing route, illustrating that the starting ink either consists of nanoparticles or precursors. Thin-film deposition is typically done in a multilayer fashion, with *pre-annealing* treatments in between each step. Annealing (also called sulfurization) is done at a higher temperature to merge the nanoparticles into larger grains or to crystallize the precursors into the CZTS phase.

1.4 SOLUTION-PROCESSING

In this thesis, CZTS absorber layers will be fabricated through solution-processing. For large-scale semiconductor fabrication to be useful in the future, a low-cost, solution-processable fabrication method is of great importance [9, 80]. The ideal process to construct an environmentally-friendly, cheap solar cell, should include solution-processing of all layers potentially on a flexible substrate, without the use of toxic solvents/chemicals or expensive elements, under ambient processing conditions, and with a high degree of recycability [81]. Several good reviews exist on liquid coating methods to produce low-cost solar cells [82].

Solution-processing is a *bottom-up* approach where a small building block is utilized to design and build a system. Using nanoparticles is an easy and convenient way to assemble a device, and parallels can be drawn to a printer ink, paint, or even Lego blocks. The chemistry offers infinite possibilities; for example new properties can be obtained by changing the number of carbon chains in the solvent molecule. The general route of solution-processing involves several steps, including ink formation (precursors choice and preparation), deposition, and heat treatments [83]. A sketch is showed in Fig. 1.5, where it can be seen

that the ink is prepared either from precursors or nanoparticles, and sulfurized to form larger CZTS grains.

CHAPTER 2

SYNTHESIS OF CU$_2$ZNSNS$_4$ NANOPARTICLES

In this chapter, nanoparticle synthesis is covered. The methods used are called the one-pot method and the hot-injection method. Phase evolution and particle size distribution are characterized, but the objective is mostly to obtain a suitable elemental composition. This chapter is restricted to syntheses that can be reproducibly prepared, so that rational adjustment of experimental conditions applies, along with a few comments on failed attempts.

2.1 INTRODUCTION

The term *nanoparticles*[1] refers to particles in the size range between of 1 nm and 100 nm (10^2 atoms to 10^7 atoms). For these systems surface properties become important compared to their bulk counterparts, as the surface-to-volume ratio is $3/r$, where r is the radius. When the nanoparticle size decreases, the optical and electronic properties of the colloidal system can change. For example, the band gap changes when the particle size is below the exciton Bohr radius. For the case of CZTS, the exciton Bohr radius is estimated to 2.5-3.3 nm [85], which is well below the size range we synthesize. Therefore, the electronic properties of the nanoparticles are not expected to be size-dependent. One general research objective for nanoparticle synthesis has been to obtain a monodisperse size distribution. This is because a uniform size distribution would result in uniform optoelectrical properties of the whole system. However, the sole purpose of the

---

[1]The term *nanoparticle* is used to describe nano-sized particles. The word *nanocrystal* implies that the complete particle consists of one nano-sized crystalline domain, while nanoparticle would then be used to denote amorphous or multi-domain inorganic cores [84]. Due to a lack of investigations with sufficient amount of samples, since there is no urgent need for crystallinity in the particles that that will be annealed at a later stage, we will use the term "nanoparticles".

CZTS nanoparticles synthesized here is to be used as the starting material for grain growth. Therefore, the aim is not to achieve a uniform size distribution.

Nanoparticles synthesis can be done in liquid phase, gas phase or solid phase [86]. CZTS nanoparticles have been synthesized with many different methods. To mention a few, from the solid state there is milling [87, 88], and solid solution reactions [89]. The liquid phase is the most frequently used for synthesis, as it allows for the best control of the reaction and serves as a medium for nanoparticle dispersion after synthesis. Liquid phase synthesis routes include arrested precipitation[2] [90], the solvothermal (or hydrothermal) approach [91, 92, 93, 94, 95, 96], microwave assisted synthesis [97, 98], and the organometallic/reduction route (including the hot-injection and one-pot method) [26, 42, 46]. The difference between the one-pot and the hot-injection methods is that the for the one-pot method, reactants are mixed at a lower temperature and heated up to the reaction temperature, while for the hot-injection method reactants are mixed at the reaction temperature.

The organometallic/reduction route was developed by Bawendi's group [99]. It is a widely applied nanoparticle synthesis approach where selected reagents in a solution are injected into a mixture of other reagents and/or solvents that are kept at a certain temperature. The isothermal temperature ensures that undesired phases can be minimized, and a relatively high temperature results in higher reaction rates and better crystallinity with less defects. The hot-injection approach is used for controlling optoelectronic material properties, with applications within light emitting diodes (LEDs), display technologies (quantum dot displays), medicine, catalysis, *etc.* The method is fast, up-scalable and ensures low material loss which makes it an interesting approach for synthesizing nanoparticles for solar cell absorber materials, and is why it was chosen to be used for this work.

2.1.1   THEORY OF NUCLEATION AND GROWTH

In this section, a presentation of nanoparticle nucleation and growth in solution is given. The process starts with homogeneous nucleation, and is followed by homogeneous growth, Ostwald ripening, and aggregation.

The formation of a new crystalline entity from a solution starts with the precursor salts transforming to active monomers which initiate the *nucleation* process. Nucleation is a thermodynamic process describing the first step in a first order phase transition[3]. Two different types of nucleation exist: homogeneous and heterogeneous, where the former refers to uniform formation of nuclei within a

---

[2]Synthesis in water at room temperature.
[3]Kinetics models also exist that describe the non-equilibrium reactions towards equilibrium, see [100] for a detailed model.

solution, and the latter to nucleation on a different media, such as other particles or the reaction beaker. Here we are interested in homogeneous nucleation. Nanoparticle nucleation in solution can be modelled with the *Classical Nucleation Theory* (CNT), which was originally developed for two-phase systems (*i.e.* gas/solid, solution/solid, melt/solid) in 1926-1943 [86, 101].
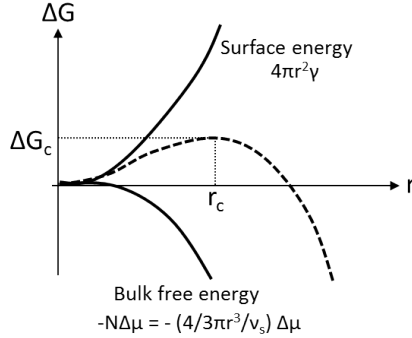
Figure 2.1: Model of total free energy, ΔG, as a function of nucleus radius, r. The curve has a maximum, ΔG_c, at the critical radius, r_c, which marks the first stable particle - the nucleus. Inspired from [102].

The driving force for nucleation is the difference in chemical potential, $\Delta \mu$, between a molecule in a solution with chemical potential, μ_s, and a molecule in the bulk of a crystal with chemical potential, μ_c, defined as

$$\Delta \mu = \mu_s - \mu_c \tag{2.1}$$

Thermodynamics tells us that

$$\Delta \mu = kT \ln S \tag{2.2}$$

where k is the Boltzmann constant, T the temperature, and S the supersaturation ratio. For nanoparticle growth in solution, the supersaturation ratio has been given as

$$S = \frac{C_{ss}}{C_s} \tag{2.3}$$

where C_{ss} is the supersaturation concentration and C_s the saturated concentration [86]. The difference in free energy, ΔG, can in its simplest form be

determined as the chemical potential between the final and the initial state for N monomers, and an additional term that takes the formation of an interface into account, as

$$\Delta G = \overbrace{4\pi r^2 \gamma}^{\text{Surface term}} - \overbrace{N\Delta\mu}^{\text{Volume term}} \qquad (2.4)$$

where r is the radius of the nucleus, γ the surface energy per unit area of the nucleus. N can be expressed as

$$N = \frac{\frac{4}{3}\pi r^3}{\nu_s} \qquad (2.5)$$

i.e. the volume of a nucleus divided by the volume of a monomer in the nucleus, ν_s. The surface term in Eq. (2.4) is positive, and the volume term negative, which results in that the curve for the nuclei free energy has a maximum at a critical radius, r_c (see Fig. 2.1). For a stable nuclei to form, a nuclei size of

$$r_c = \frac{2\gamma\nu_s}{\Delta\mu} \qquad (2.6)$$

must be exceeded. The corresponding activation energy (free energy barrier) becomes

$$\Delta G_c = \frac{16\pi\gamma^3\nu_s^2}{3\Delta\mu^2} \qquad (2.7)$$

The spontaneous process is characterized by a decrease in the free energy, and thus the particles with a size larger than r_c will grow while the smaller ones will dissolve again. The above derivation shows that a supersaturated solution is required for nuclei formation.

Once the nuclei are formed, *homogeneous growth* will proceed. During this step, nuclei grow by consuming monomers. Monomers will diffuse to the nucleus surface where they adsorb and can be incorporated. The driving force for particle growth is to minimize the surface free energy.

At some point the concentration of monomers in the solution will be exhausted, and the concentration falls below the supersaturated threshold. No further nucleation will occur, and homogeneous growth will also be reduced. Now growth

by *Ostwald ripening* can take place. Larger particles grow and smaller particles dissolve and disappear, to reduce the surface energy of the system [86].

The final growth mechanism is *aggregation*, where the large surface area and surface energy can cause particles to merge together. Most times smaller particles will be absorbed/engulfed by larger particles, instead of same size particles merging. The barrier for aggregation increases with particle size, which makes it more dominant for smaller particle sizes. The growth rate is higher than for homogeneous growth, but the process is also less controllable. Stabilizing agents, such as ligands, can be used to minimize aggregation. However, in solution the ligands are constantly adsorbed/desorbed on the surface of the particles, which anyway can lead to aggregation.
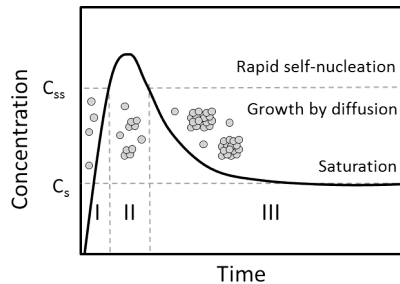

Figure 2.2: La Mer model of nucleation and growth . I: prenucleation phase, II: nucleation phase, and III: growth phase, where C_s is the saturation concentration of monomers, and C_{ss} the supersaturation concentration.

2.1.1.1 LA MER MODEL

In the 1950s, La Mer and co-workers developed a method for obtaining monodisperse nanoparticles. They found that separating the nucleation and the growth events was the cue for controlling the particle size. The well-known La Mer model is displayed in Fig. 2.2(a) [103, 104]. In phase (I), the monomer concentration, C, is quickly increased to above the supersaturated threshold, C_{ss}, where the energy barrier (activation energy) for nucleation can be overcome and nucleation can occur in phase (II). When the monomer concentration again reaches C_{ss}, the nucleation comes to an end. This ensues the final stage (III), where particle growth proceeds as homogeneous growth, Ostwald ripening or aggregation, and can be interpreted as heterogeneous nucleation/growth, until the monomer concentration is lowered to the solubility limit [84, 102, 105]. If the concentration stays above C_{ss} for an extended period of time, *i.e.* if the nucleation rate is too low, then growth will occur at the same time. This will make a monodisperse size distribution less likely.
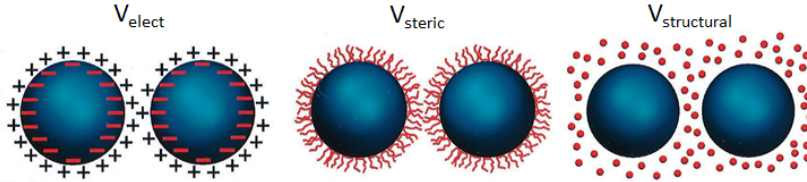
Figure 2.3: Types of repulsive forces between particles, including electrostatic, steric and sturctural forces (adapted from [106]).

2.1.1.2 INTERPARTICLE FORCES

Once the nanoparticles are formed, a stable ink is desired to facilitate homogeneous growth as well as uniform deposition. A stable ink is one where the nanoparticles are dispersed in a solvent and do not precipitate. Once particles are in direct contact with each other, irreversible adhesion will often occur which is followed by precipitation. Therefore it is necessary to avoid coagulation. This is achieved by balancing the attractive van der Waals forces between particles with repulsive interparticle forces. The total interparticle potential energy, V_{total}, of a particle in a solution is governed by

$$V_{total} = V_{vdW} + V_{elect} + V_{steric} + V_{structural} \qquad (2.8)$$

where V_{vdW} is the attractive van der Waals potential energy between particles, V_{elect} the electrostatic repulsive potential energy from particles with charges of the same sign, V_{steric} the steric repulsive potential energy resulting from polymer species adsorbed on the surface of the particles, and $V_{structural}$ the structural potential energy from non-adsorbed species in the solution that could either increase or decrease the stability of the suspension (Fig. 2.3). Expressions for all these forces can be found in [105, 106]. The most used route to keep CZTS nanoparticles apart, when synthesized via the organometallic/reduction route, is sterical stabilization by ligands. Ligands can also have other effects such as to passivate and protect the surface against oxidation and electronic traps from surface defects [102, 106]. The type of stabilization mechanism dictates the type of solvent that can be used. For example, long, bulky hydrocarbon chains can typically only be dispersed in non-polar solvents, while electrostatically stabilized particles would be dispersed in polar solvents. Examples on exchanging the long ligands to shorter ones exist, and is one route that has been examined for CZTS nanoparticles [84, 107].

2.1.2 REACTION CONDITIONS FOR CZTS NANOPARTICLE GROWTH

Numerous studies on the influence of the reaction conditions for CZTS nanoparticle synthesis have already been conducted, and this section will present a short

overview of some relevant findings. In particular, studies on the effect of synthesis temperature, synthesis time, precursor concentration, solvent, and injection rate are presented. All examples concern the hot-injection method, except when otherwise stated.

- The *reaction temperature* is limited by the boiling point of the solvent, and a higher temperature should provide more thermal energy for each atom to find an energetically favorable bonding position and thus reduce defects in the crystal lattice. Furthermore, different phases evolve at different temperatures. For the one-pot method, Cu-S is typically formed below 180°C, followed by incorporation of Sn to create Cu-Sn-S by cation exchange or ionic diffusion and nucleation of Zn-S as the temperature is increased. Finally, the CZTS phase will form as the binary and ternary particles will dissolve or fuse together [108, 109, 110]. Larger particles can be achieved at higher temperature [85, 108].
- The influence of *reaction time* is important for the formation of wurtzite CZTS, and several secondary phases were detected for reaction times below 2 h and 4 h, respectively [27, 111], whereas kesterite CZTS was formed already after 10 min [111]. For small particles (less than 7 nm), reaction time did not affect the synthesized product [85].
- The *precursor concentration* can be used to tune the composition in the CZTS nanoparticles [112].
- The *choice of solvent* should affect the growth rate, and different solvents have been seen to result in different XRD peak sharpness (particle sizes) [29]. The particle shape can be tuned with the solvent [108], as well as the phase (wurtzite/kesterite) [111, 113, 114]. Furthermore, the *amount of solvent* used can affect the particle size (less solvent results in larger particles) [85], as a higher ligand concentration makes it harder for particles to grow, and inhibits nucleation.
- Finally, the *injection rate* should affect the particle size distribution [84]. This was studied once, and very slow injection rates were used (inject 5 ml with speeds between 2.5 ml/h and 20 ml/h). The particle size increases and size distribution widens for faster injection rates[4] [56].

The complete process of nanoparticle synthesis depends on a wide range of parameters such as the surfactant molecules, the precursors and the solvent, and this is still not completely understood [115]. The theoretical description in Section 2.1.1 should aid in the understanding of the process, but cannot easily be directly applied to the experiments.

---

[4]Their injections take between 2 h and 15 min (except for "quick injection"), and nucleation can occur in the sub-picosecond time scale [86], so they are more likely studying growth with constant addition of monomers (maybe some re-dissolution of particles or the alike.).

2.2   EXPERIMENTAL DETAILS

Synthesis of air-sensitive compounds is normally done with a so called *Schlenk line*, which allows for pumping and purging with an inert gas [116].
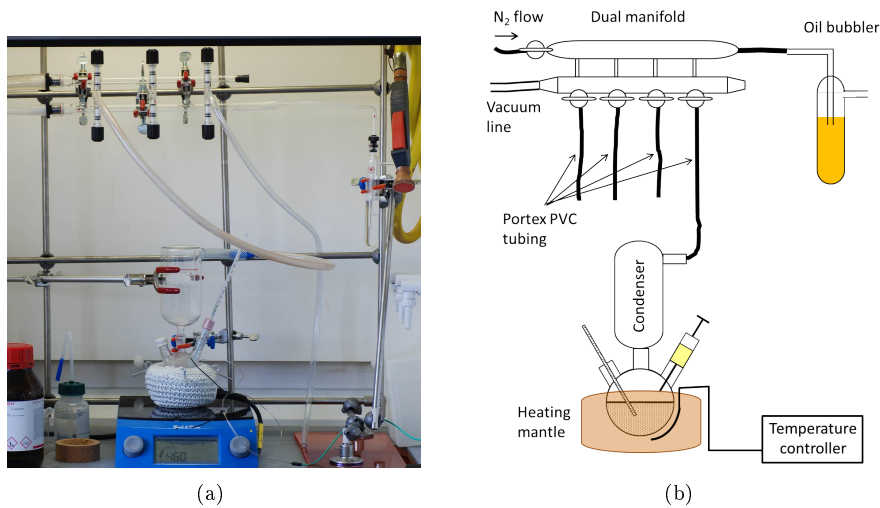

Figure 2.4: Image (a) and schematics (b) of experimental setup.

2.2.1   EXPERIMENTAL SETUP

The Schlenk line was purchased from Sigma Aldrich and placed in a fume hood with flow velocities between 0.3 m/s and 0.5 m/s. An image and schematics of the setup can be seen in Fig. 2.4. The Schlenk line consists of a dual manifold, with one compartment connected to a vacuum pump from Pfeiffer Vacuum (model MVP 070-3 2013/12, base pressure approx. 10^{-2} mbar) and the other to a flow of nitrogen. The nitrogen flow is stopped with an oil bubbler, which allows a slight overpressure of nitrogen inside the system and is a convenient way to monitor the gas flow. A 100 ml three-necked reaction flask can be connected to the manifolds via PVC tubing, and by the valves it can be controlled whether the system should pump or purge. Additional equipment includes a rubber stopper that a syringe can perforate, a thermometer immersed in the reaction mixture, a condenser, and a heating mantle (maximum temperture 450°C, Ø150 mm from Buch & Holm). The heating mantle was placed on a magnetic stirrer from Schott Geräte GMBH.

The temperature of the reaction mixture was controlled by a home-made system, since the heating mantle only could be turned on and off. A K-type thermo-couple from Thermocoax (inconel 600 sheat material, Ø1 mm, length = 80 cm)

was placed between the heating mantle and the reaction flask, and connected to a temperature controller from Intercontrol Regutherm. The temperature controller will set the temperature, but due to varying positions of the thermocouple inside the heating mantle, the temperature in the reaction mixture has to be monitored simultaneously.

To aid mixing of solvents and dispersing particles, a sonicator from Branson, Bransonic Ultrasonic Cleaner was used (model 2510E-MT, 100 W with a frequency of 42 kHz).

2.2.1.1 PARTICLE CLEANING AND COLLECTION

Synthesized particles can be cleaned and collected via centrifugation. As described above, particle aggregation takes place when the repulsive forces from *e.g.* the capping ligands cannot balance the attractive van der Waals forces between particles. The energetic barrier to aggregation depends upon the energy of mixing between the capping ligands and the solvent. By adding a non-solvent that is miscible with the original solvent, this barrier is lowered and the nanoparticles are destabilized in the dispersion and will aggregate. Furthermore, centrifuging this mixture increases precipitation of the particles. Large particles have larger attractive forces, and will aggregate first. Smaller nanoparticles, excess capping molecules and salts will be left in the supernant, and these synthetic by-products can be dispensed. The precipitate can be redispersed in solvents if the capping ligands are well-bound [84]. A centrifuge purchased from Thermo Fischer (model Megafuge 8, with a HIGHConic rotor, a capacity for 6×50 mL, and a maximum speed of 8,700 rpm), was used with capped conical test tubes from Corning (Sterile, 50mL, PP, 17000xg, 29 mm×114 mm).
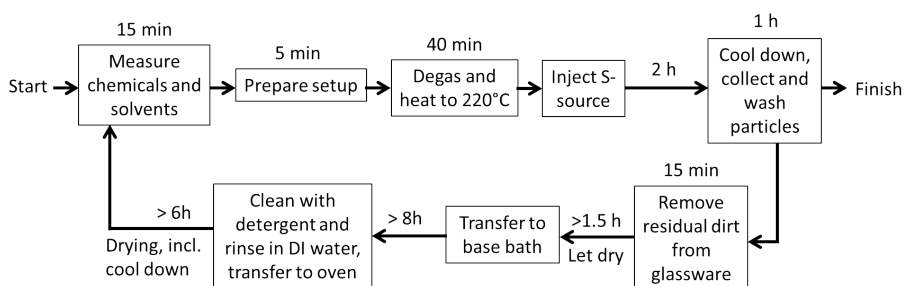

Figure 2.5: Process flow diagram of tasks related to one synthesis.

2.2.2 EXPERIMENTAL PROCEDURE

The typical salts used for CZTS synthesis are acetates, acetylacetonates and chlorides, and these are not expensive [117]. All chemicals used are listed in

Papers I-III, together with the nanoparticle synthesis recipes used. An illustration of the tasks required for a typical synthesis is depicted in Fig. 2.5, where time estimates also are given. The total time is about 20 h, and the active working time is about 4 h.

As an example of a hot-injection synthesis procedure, the recipe for ligand-free nanoparticles (**Paper II**) will be given here. Calculated amounts of CuCl$_2$·2H$_2$O, Zn(OAc)$_2$ and SnCl$_4$·5H$_2$O were mixed with 7 ml diethylene glycol (DEG) in the three-necked flask. The reaction mixture was degassed for 20 min under stirring at room temperature and then the temperature was increased to 220°C while purging with nitrogen[5]. The color of the mixture evolved from green to transparent at 210°C (Fig. 2.6). Afterwards, a solution containing 1 mmol S, 0.5 ml triethylenetetramine (TETA) and 1 ml DEG was quickly injected to the flask while stirring the solution (S was first dissolved in TETA and then DEG was added to this solution). The mixture now turned black. The reaction solution was kept under stirring at 220°C for 2 h, and thereafter the resulting mixture was allowed to naturally cool down to room temperature.

10 ml deionized (DI) water and 10 ml ethanol were added to the mixture, and it was transferred to a 50 ml conical centrifuge tube. After 10 min ultrasonication, the mixture was centrifuged at 6000 rpm for 10 min and the supernatant was decanted. The precipitate was subsequently rinsed through dispersing in a solution mixture containing 5 ml DI water and 5 ml ethanol, followed by centrifuging at 6000 rpm for 10 min.

| 25°C | 70°C | 150°C | 180°C | 210°C | 220°C |
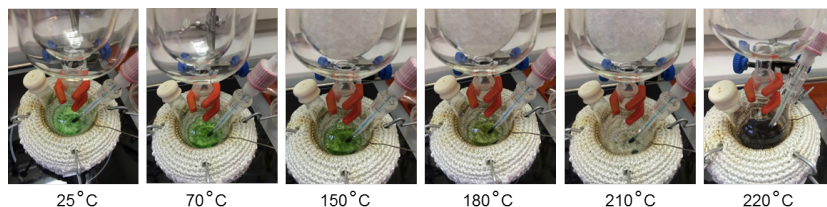
Figure 2.6: Color evolution of ligand-free nanoparticle synthesis: From green at room temperature to transparent at 210°C. At 220°C the S-TETA/DEG solution is injected, which causes the color change from transparent to black.

2.2.3 CHARACTERIZATION

The experimental techniques used for characterization of the Cu-Zn-Sn-S colloidal systems include (in descending order of amount used): Energy-dispersive

---

[5]TETA has a boiling point of 260°C and DEG of 245°C. In practice, the mixture of the two solvents started to boil at 220°C, and the reaction temperature was kept just below this point (216-218°C).

X-ray spectroscopy (EDX or EDS), X-ray diffraction (XRD), Raman spectroscopy, transmission electron microscopy (TEM), Fourier transformed infrared spectroscopy (FTIR) , and X-ray photoelectron spectroscopy (XPS). Here, focus is put upon the most used techniques, the reliability of the results, and which references were used. For typical measurement conditions, see **Papers I-III**.

2.2.3.1 Energy dispersive X-ray spectroscopy (EDX)

The elemental composition is determined with the technique "EDX". A sample is bombarded with a beam of electrons which excite the inner electrons in the material, and when they relax into the ground state, characteristic X-rays are emitted. Qualitative analysis can be done on elements with atomic number from $Z = 10$ ($Z = 4$ for some equipment) to $Z = 92$, but for a precise quantitative analysis calibration is recommended. Certain elements have very similar energies, which led to difficulties particularly in **Paper IV**, where Na was included. The K_α energy of Na (1.041 eV) is very close to the L_α energy of Zn (1.012 eV) and Cu (0.930 eV). Likewise, S (2.307 eV) and Mo (2.293 eV) have very similar energies, which made them hard to distinguish.

The measurements carried out in this work were not calibrated, since the nanoparticle samples contain various amounts of organic materials and different grainsizes. Calibration would require a sample with a precise amount of cations, but adding an unknown quantity of *e.g.* carbon would change the matrix correction (*i.e.* ZAF (atomic number, absorption, and fluorescence) correction) of the material.

To obtain reliable measurements, film thickness of more than 1 µm as well as a sufficient measurement time should be used. Due to lack of calibration, there could be a systematic error related to these measurements, so that some elements are always overestimated and some always underestimated. Thus, these measurements should not be considered as absolute values, but rather serve as a comparison between similar samples.

2.2.3.2 X-ray diffraction (XRD)

Diffraction is based upon a principle of constructive interference, and follows Bragg's law: $n\lambda = 2d\sin(\theta)$, where n is an integer, λ the wavelength of the incoming X-rays, d the spacing between crystal planes, and θ the angle of incoming light. Peaks appear for XRD at certain 2θ angles because of constructive interference: X-rays are scattered in all directions, but the signal is weak except for when crystal planes reflect the X-rays constructively. The XRD pattern thus gives us the d-spacings in the crystal. To assign a phase to pattern with
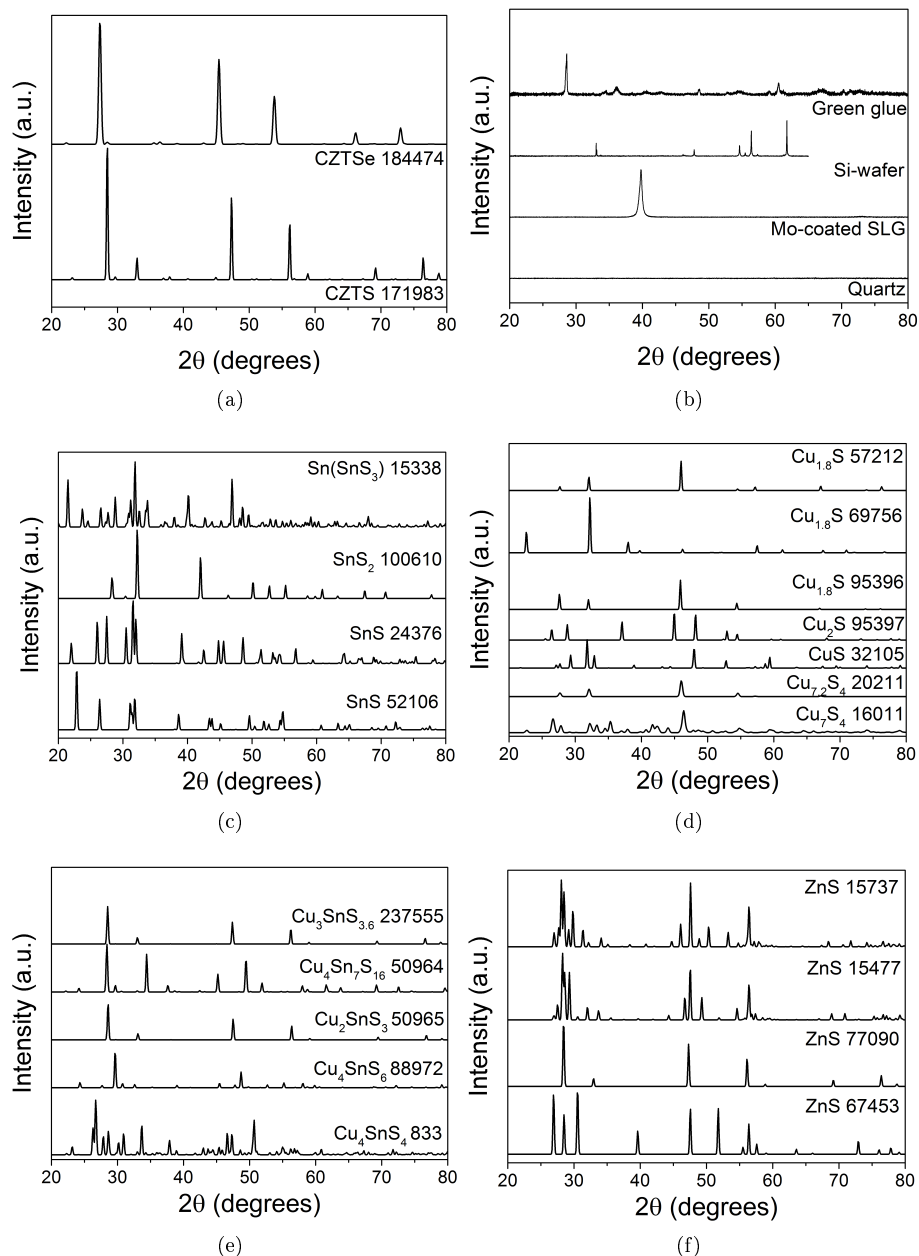
Figure 2.7: XRD reference patterns of CZTS and CZTSe (a), substrate signals (b), and potential secondary and ternary phases in the Cu-Zn-Sn-S system (c), (d), (e), and (f). Some of the measurements in (b) were done by Naghmeh Mirbagheri. Corresponding ICSD coll. codes are also noted.

certainty more than three peaks should be present. The peak intensity can vary depending on preferential orientation.

All XRD peaks were matched manually to the references from the ICSD, most of which are displayed in Fig. 2.7 with corresponding collection codes. The diffraction patterns for kesterite[6] CZTS and CZTSe are showed in Fig. 2.7(a). The 2θ diffraction peak positions for CZTS are at $28.5°$, $32.9°$, $47.4°$ and $56.3°$; and for CZTSe, the peak positions shifted to lower values, $27.3°$, $36.2°$, $45.3°$ and $53.7°$. These peaks correspond to the (112), (200), (220), and (312) plane reflections for CZTS, and (112), (105), (204), and (312) for CZTSe, respectively. The Bragg angles for CZTSe are shifted to lower values compared to CZTS because CZTSe has a larger lattice-spacing than CZTS due to the larger Se atoms (120 pm) replacing the S atoms (100 pm). One explanation for the occasionally seen broadening of the main kesterite (112)-reflection is the existence of wurtzite (100) and (101) planes [111]. Similar broadening features have also been seen in CIGS, where the broadening and the sharp shoulder on the left side of the peaks were attributed to planar defects in the lattice [118].

The XRD patterns of the bare substrates are displayed in Fig. 2.7(b). "Green glue" denotes the glue used to hold the samples in position, which could be detected for small samples.

Some selected secondary phases in the Cu-Zn-Sn-S system are showed in Fig. 2.7(c)-(f). CZTS, Cu_2SnS_3 (ICSD coll. code 50965) and ZnS (ICSD coll. code 77090) have the same d-spacings, and can therefore not be easily distinguished with XRD[7]. There are a few small peaks, e.g. one peak at $23.1°$ in the CZTS pattern that is not present for Cu_2SnS_3 or ZnS, which is why we start the measurements at $20°$. However, this peak could of course stem from other phases such as SnS (ICSD coll. code 52106) or Cu_4SnS_4 (ICSD coll. code 833).

Figure 2.8: Optical micrograph used for determining where to do a Raman measurement. A typical "bright spot" and "dark spot" are indicated.

2.2.3.3 Raman spectroscopy

Raman modes are strongly affected by the crystal structure and chemical composition, which is why it is useful for detecting secondary phases. Raman spec-

---

[6]Stannite and kesterite CZTS cannot be distinguished with conventional XRD [45].
[7]Similarly for CZTSe, its peaks overlap with ZnSe and Cu_2SnSe_3.

Table 2.1: Raman shifts for common secondary phases, where bold marks the most intense peaks. Inspired by [119].

Phase	Raman shift (cm^{-1})	Reference
CZTS	68, 82, 97, 140, 164, 255, 263, 271, **287**, 302, 316, 332, **338**, 347, 353, 367, 374	[120, 121, 122]
Cu_3SnS_4 (orthor.)	295, **318**, 348	[123, 124]
Cu_2SnS_3 (tetragonal)	297, **337**, 352	[123, 124]
Cu_2SnS_3 (cubic)	267, **303**, **356**	[123, 124]
Cu_2SnS_3 (monoclinic)	**290**, **352**, 314, 374	[125, 126]
$Cu_{2-x}S$	264, **475**	[124]
ZnS (cubic)	275, **352**	[124]
SnS (orthor.)	96, **163**, **189**, **220**, 288	[124, 127, 128]
SnS_2 (hexagonal)	312	[124, 127, 128]
Sn_2S_3 (orthor.)	87, 183, 234, 251, **307**	[127, 128]
MoS_2 (hexagonal)	288, 384, **410**	[121, 124]

troscopy is based on inelastic scattering of incident light. It probes the Stokes- and anti-Stokes-shifts in an excited semiconductor. The Stokes shift results in the creation of a phonon, and a loss in energy. The anti-Stokes shift requires annihilation of a phonon for a gain in energy. The Stokes shift is more likely, since it does not require energy, and therefore has a higher intensity and is what we probe for. The difference in frequency between the incident light and scattered light, is called the Raman shift.

In this work, the Raman spectra are generally acquired by analyzing a sample in several places, and choosing a representative spectrum. This spectrum is affected by scattering (surface roughness) and the measurement conditions, so the same conditions were used for all samples. The Raman effective analysis depth can be estimated from $d_\alpha = \frac{1}{2\alpha}$ [129], and this gives 500 nm [130], when the absorption coefficient of CZTS is $10^4 cm^{-1}$. In fact the absorption coefficient can go up to $10^5 cm^{-1}$, which results in a laser penetration depth of 50 nm. The optical micrograph used to determine where to do a Raman measurement can be used to detect suspiciously looking phases (Fig. 2.8). Most times bright spots were holes in the CZTS nanoparticle layer and a a peak shift at 402 cm^{-1} could be detected, which corresponds to MoS_2. The dark spots also indicated in the image had similar spectra as the surrounding material. The Raman peaks used for peak identification are collected from different references, and listed in Table 2.1.
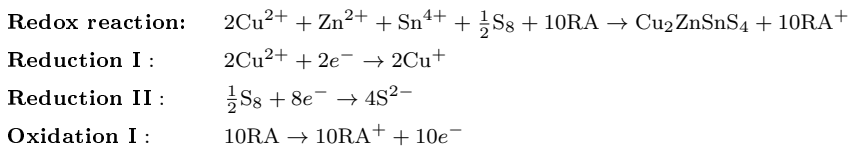
2.3   RESULTS AND DISCUSSION

In the search for the best CZTS nanoparticles for a solar cell ink, I have worked on creating and optimizing several different syntheses: both for kesterite and

wurtzite nanoparticles, with and without organic ligands, and via both the one-pot and hot-injection method, as well as making CZTS thin films directly from precursors. Some of them were successful, some of them not. Here, I will present the results I obtained and why I gave up the one-pot method in Section 2.3.2, and the more useful results for the large CZTSe kesterite nanoparticles in Section 2.3.3, and finally the ligand-free kesterite CZTS nanoparticles in Section 2.3.4.

2.3.1 GENERAL REACTION PATHWAY

The CZTS nanoparticles are formed through a redox reaction, where the oxidation states of the chemical species change during the reaction. This is necessary *e.g.* for Cu, since its oxidation state in the salts is +2 but in CZTS it is +1. The reaction pathway for all syntheses is:

Redox reaction:	$2Cu^{2+} + Zn^{2+} + Sn^{4+} + \frac{1}{2}S_8 + 10RA \rightarrow Cu_2ZnSnS_4 + 10RA^+$
Reduction I :	$2Cu^{2+} + 2e^- \rightarrow 2Cu^+$
Reduction II :	$\frac{1}{2}S_8 + 8e^- \rightarrow 4S^{2-}$
Oxidation I :	$10RA \rightarrow 10RA^+ + 10e^-$

where RA denotes reducing agent. The reducing agent is required for donation of additional electrons. The oxidation states of the metal salts are either unchanged or reduced, and the reducing agent is oxidized. In the syntheses, either oleylamine (OLA) or DEG/TETA were used as reducing agents. These solvents are well-known reducing agents for CZTS synthesis [131, 132]. OLA participates in the reaction mechanism, where it in the presence of a Cu precursor is oxidized above 130°C and cause Cu reduction. Even metallic Cu was detected after synthesis [133]. We have also seen metallic Cu nanoparticles with TEM EDX for some syntheses. Accordingly, the presence of DEG/TETA can reduce Cu^{2+} to Cu^+ [132].

To confirm the oxidation state of copper, zinc, tin, and sulfur elements in the synthesized nanoparticles, the ligand-free nanoparticles (see Section 2.3.4) were analyzed with XPS (Fig. 2.9). As explained in **Paper II**, the oxidation states found were Cu^+, Zn^{2+}, Sn^{4+}, and S^{2-} which is in agreement with the oxidation states of Cu, Zn, Sn and S in the CZTS phase.
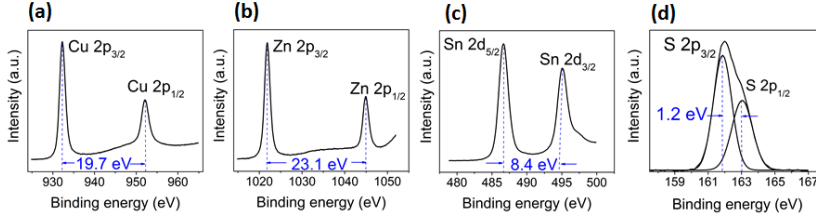
Figure 2.9: XPS spectra of the as-synthesized sample P6 (see Section 2.3.4), with (a) Cu 2p, (b) Zn 2p, (c) Sn 2d, and (d) S 2p signals. Figure adapted from **Paper II**. XPS measurements taken by Andrea Crovetto.

2.3.2 LIGAND-COATED CZTS NANOPARTICLES (ONE-POT SYNTHESIS)

In August 2013, only few sulfide CZTS nanoparticle solar cells had been developed. The earliest working device (which was produced by spray-coating[8]), by Steinhagen *et al.* seemed like a good place to start [26]. Steinhagen *et al.* used the one-pot method. Therefore, the outcome of trying to repeat this synthesis is presented in this section.

Table 2.2: Effect of varying metal salt concentration on elemental composition. The percentages are average atomic percentages of at least five measurements with corresponding standard deviations. The Cu-salt used is $Cu(acac)_2$, the Zn-salt is $Zn(OAc)_2$, and the Sn-salt is $SnCl_4 \cdot 5H_2O$. The composition is showed as CZTS, but could in fact be a mixture of different phases.

Sample	Cu-salt (mmol)	Zn-salt (mmol)	Sn-salt (mmol)	Cu (at.%)	Zn (at.%)	Sn (at.%)	S (at.%)	Composition
A1	0.50	0.39	0.24	29.6±2.7	13.2±1.8	9.6± 1.2	47.6±3.2	$Cu_{3.1}Zn_{1.4}SnS_{5.0}$
A2	0.50	0.39	0.24	27.1±1.6	15.8±2.4	10.2±1.3	46.9±3.2	$Cu_{2.6}Zn_{1.5}SnS_{4.6}$
A3	0.40	0.40	0.26	24.5±2.6	15.6±2.8	11.6±1.4	48.3±2.7	$Cu_{2.1}Zn_{1.4}SnS_{4.2}$
A4	0.40	0.43	0.28	21.0±2.4	18.8±1.2	12.4±1.4	47.9±3.3	$Cu_{1.7}Zn_{1.5}SnS_{3.9}$
A5	0.40	0.36	0.26	25.7±0.7	15.3±1.0	11.3±0.2	47.6±0.8	$Cu_{2.3}Zn_{1.4}SnS_{4.2}$
A6	0.40	0.36	0.31	24.4±0.9	13.5±0.9	13.7±0.7	48.4±1.5	$Cu_{1.8}Zn_{1.0}SnS_{3.5}$
A7	0.40	0.38	0.31	23.8±1.1	13.7±0.5	13.4±0.8	49.1±1.1	$Cu_{1.8}Zn_{1.0}SnS_{3.7}$
A8	0.40	0.38	0.28	24.6±0.7	16.0±0.4	10.7±0.9	48.7±1.6	$Cu_2Zn_{1.1}SnS_{4.3}$

2.3.2.1 REPRODUCIBILITY

An example of how difficult controlling the EDX measured composition of the nanoparticles with the one-pot synthesis has been, can be seen in Fig. 2.10. Here, the Cu- and Zn-ratios in the synthesized products are plotted as a function of added salt concentrations. One should in principle be able to tune the composition by changing the salt concentration, but the reproducibility issue

---

[8]The goal for this project was, as stated in the Preface, to produce CZTS solar cells by spray-coating technique.
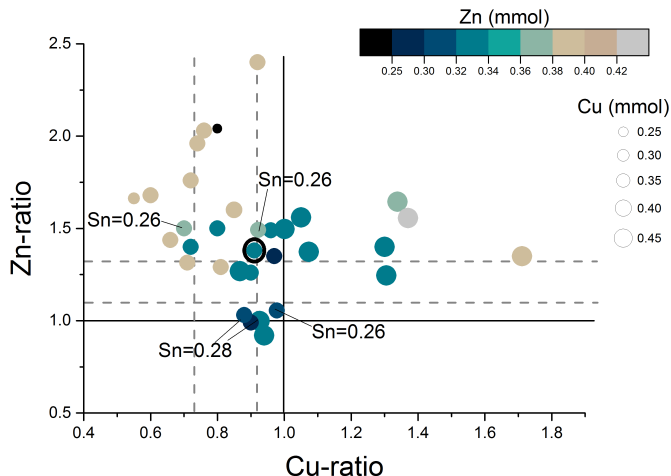
Figure 2.10: Composition in terms of Zn-ratio (*i.e.* Zn/Sn) and Cu-ratio (*i.e.* Cu/(Zn+Sn)) as a function of changing the added Zn and Cu metal salt concentration. The Sn-amount was mostly fixed to 0.24 mmol except when marked, and the S amount to 1.01 mmol. There are some general trends: Adding more Zn (greyish colors), on average results in a higher Zn-ratio than adding less Zn (blueish colors). Likewise, adding more Cu (larger circles) results in a higher Cu-ratio than adding less Cu (smaller circles). However, the main point of the plot is that it is difficult to control the composition with the one-pot method under the conditions used here.

suggests that another factor is at play. The difference between the one-pot (or the *heat-up* method) and the hot-injection method depends on the temperature at which the S-source is added, and this could explain the scattering of the measured data. During the heat-up phase of the one-pot reaction, different phase formations become favorable: at 180°C $Cu_{2-x}S$ is formed, which transforms into a Cu-Sn-S phase at 200°C, and subsequently incorporates Zn to form CZTS at 220°C [108]. Maintaining the reaction in one phase formation regime for a time period longer would bring the reaction into formation of more or less of a particular secondary phase. Furthermore, the one-pot method does not separate the nucleation and growth events. This has conventionally been considered as a detrimental state towards achieving control over particle formation. However, there are recent examples of where monodisperse CZTS nanoparticles have been synthesized in this way, by choosing suitable precursors, stabilizers, and heating rates [134, 135]. Admittedly, the typical heating rates in our experimental setup were not very carefully controlled, and the main goal was to reproduce the results of Steinhagen *et al.* so that no other precursors or stabilizers were used.

The large spread of the measurements could also stem from other errors. These include: (1) weighing the salts, especially the tin chlorides, which easily absorb a lot of water, (2) uneven stirring and particles left on the edge of the flask, (3) errors from measuring the composition with EDX, whether from varying sample thickness or different amount of organic material left in the films.
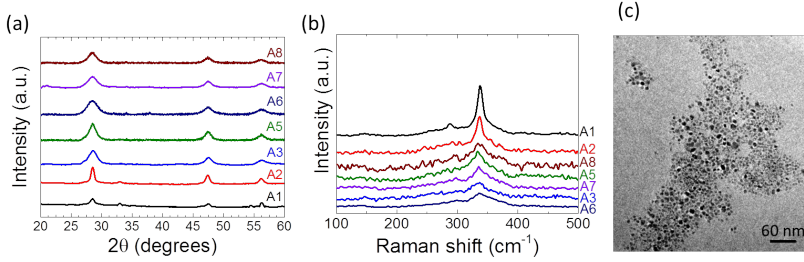

Figure 2.11: XRD patterns (a) and Raman spectra (b) of selected syntheses from the one-pot method. TEM micrograph (c) of particles from the circled synthesis in Fig. 2.10 (*i.e.* A3).

The compositions of a few selected syntheses are showed in Table 2.2, and some addition characterization in Fig. 2.11, including XRD patterns, Raman spectra, and a TEM micrograph of nanoparticles A3 (the circled point in Fig. 2.10). The synthesized material never reached the desired composition, but this does not have to be detrimental, as the composition can change during annelaing. For example, the atomic percentage of Sn can be increased by adding SnS-salt during sulfurization [136]. The XRD patterns of most syntheses show the main CZTS peaks, and no other phases could be detected (Fig. 2.11(a)), and similarly the Raman spectra only display the main CZTS peaks (Fig. 2.11(b)). The XRD peaks are broad, which indicates small crystallites. An estimate of the average crystallite diameter can be obtained by using the Scherrer equation,

$$D = \frac{K\lambda}{\text{FWHM}\cos(\theta)} \tag{2.9}$$

where K is a constant depending on the particles shape (for spherical particles, $K = 0.9$ is typically used), λ the wavelength of incident X-rays ($\lambda = 0.154$ nm), FWHM the full width at half maximum of the peaks, and θ the angle [137]. For sample A3, D becomes 5.7 nm, which is similar to the particle sizes in the TEM micrograph (Fig. 2.11(c)). The broad Raman peaks have also been linked to small particle sizes [85].

2.3.2.2 Outcome

When the composition was satisfactory, these nanoparticles were used for thermal analysis, to optimize the deposition condition, and for studying the annealing conditions. Furthermore, it is important with a precise temperature control when working with the one-pot synthesis, since minimal changes in ramp rate could potentially result in different nanoparticles created. Interestingly, XRD and Raman characterization only show the desired CZTS peaks, while the EDX measurements suggest a very off-stoichiometric CZTS. For instance for A1, the measured EDX composition appear unrealistic for the CZTS phase. Either the material contains secondary phases, or the synthesized material was close to having the correct composition, but the EDX measurements simply had a lot of variations from different amount of organic residue in the films.

2.3.3 Ligand-coated CZTSe nanoparticles

This section concerns our results on how one can synthesize nanoparticles larger than what is typically obtained with the hot-injection method. The motivation for this work was manifold. The main goal in the literature until now has been to achieve a narrow size distribution in order to form a compact film [138]. However, perhaps a better packing density can be achieved from having a mixture of large and small nanoparticles, as predicted by theoretical models for bidisperse random packings [139, 140, 141, 142]. A better packing density with larger particles could mean a better starting point for grain growth during annealing, which means savings in terms of lower sulfurization temperature or shorter time. Perhaps, if the particles are micron-sized, no annealing would be necessary, as have been seen in other systems [143]. In this project, we made an exception and used selenium to study particle growth. This section gives a summary of the main findings in **Paper I**, as well as presents a few un-published results.

2.3.3.1 Summary of findings in paper

In **Paper I**, a new approach to the typical synthesis procedure is presented. In short, a solution of Se-trioctylphosphine (TOP) was injected into a dispersion of CZTS nanoparticles in hexadecane at a suitable synthesis temperature. This allowed the transformation from CZTS nanoparticles to CZTSe nanoparticles. The resulting material was characterized by XRD, Raman, EDX, and TEM. The interesting finding was that the CZTSe nanoparticles were significantly larger than other CZTSe nanoparticles synthesized by the hot-injection method in the literature[9].

---

[9] The co-called "CZTSe" nanoparticles actually contained about 10% S, but are called CZTSe for simplicity.

First, we demonstrated that it was possible to transform CZTS nanoparticles into CZTSe nanoparticles by injecting Se. We studied the effect of synthesis temperature, time, and injected Se-concentration for the conversion from CZTS to CZTSe. There was no significant correlation with the transformation temperature. The injected Se-concentration dictated the transformation rate from CZTS to CZTSe, since the nanoparticles contain a higher atomic percentage of Se the higher Se-concentration is injected (after 30 min of reaction). Finally, by imaging particles as a function of synthesis time, particle growth was found to occur.
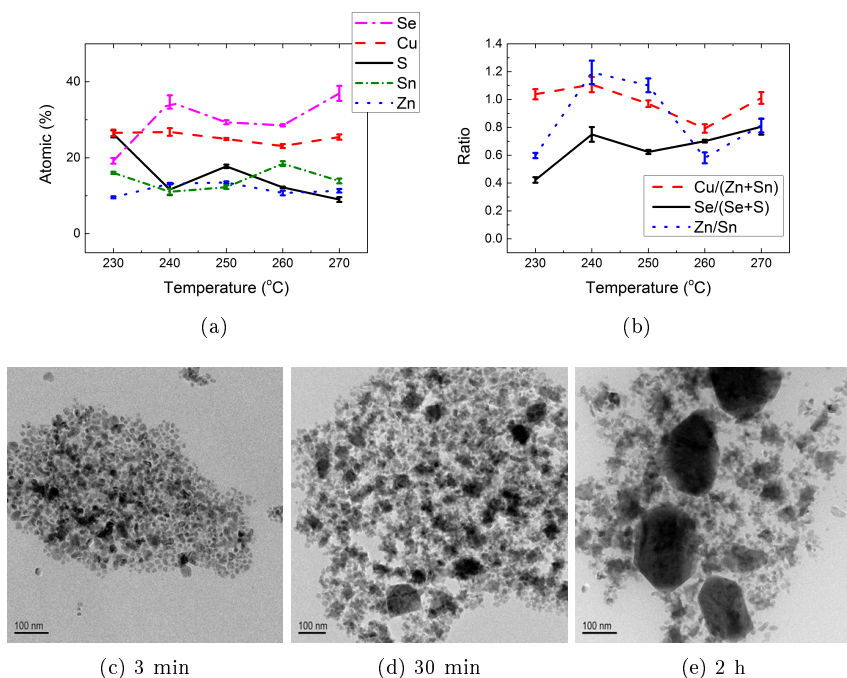

(a)   (b)

(c) 3 min   (d) 30 min   (e) 2 h

Figure 2.12: Atomic (a) percentages and (b) ratios versus reaction temperature for 30 min and 1.33 M Se. TEM micrographs (c)-(e) of particles as a function of time at 230°C and 0.66 M. Large particles exist already after 3 min under these conditions, but fewer than for longer times. EDX measurements taken together with Zhenggang Li, and images taken by Zhenggang Li.

2.3.3.2   The effect of synthesis temperature

The transformation was optimized with respect to reaction temperature, and the composition after transformation can be seen in Fig. 2.12. No significant correlation was found in terms of temperature. The elemental ratios in the material is not very well-controlled (Fig. 2.12(b)), as the Cu- and Zn-ratios

fluctuate. This is a consequence of a few percentage variation in the measured atomic percentages (Fig. 2.12(a)), and a good example of how sensitive the final composition is on slight variations in reaction conditions. Another outcome from this study is that more S is exchanged by Se as the reaction temperature increases. A reaction temperature of 250°C was used for the main experiments, and **Paper I** displays how particle growth occurs at this temperature.

Fig. 2.12(c-e) show particle size evolution at a lower temperature of 230°C, where particle growth also is observed. Note that also less Se is injected than in **Paper I**. A very wide size distribution is seen in Fig. 2.12(e), however this could also depend on the amount of washing the particles.
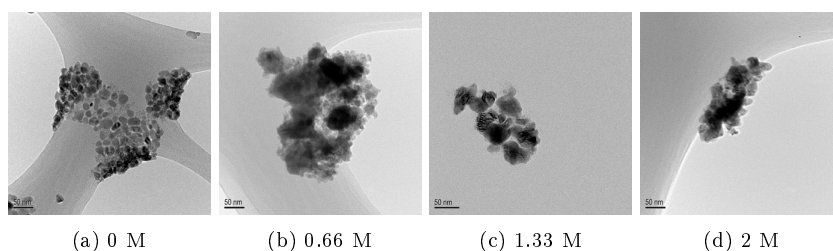

(a) 0 M   (b) 0.66 M   (c) 1.33 M   (d) 2 M

Figure 2.13: TEM micrographs of different injected Se-concentration for 30 min of reaction at 250°C. Images taken by Zhenggang Li.

2.3.3.3   The effect of injected Se-concentration

The optimal concentration of injected Se was determined based on measuring the composition of the particles (Fig. 4 in **Paper II**). We found that more S is exchanged by Se as the injected Se-concentration increases, and that the Cu, Zn and Sn atomic percentages remain rather constant. After 30 min of reaction time, the ratio of CZTS converted to CZTSe increases at higher injected Se-concentrations. Moreover, the substitution of S to Se seems to approach saturation after 2 M of Se. In order to observe changes on a suitable time scale, a concentration of 1.33 M was chosen for the main study.

The particle sizes were preliminary investigated (Fig. 2.13(a)-(d)), and when no Se was injected, no significant particle growth was observed. On the other hand, when Se was injected large particles were seen, but with no clear difference between the different Se-concentrations.

2.3.3.4   Proposed formation mechanism

A few different formation mechanisms could be used to explain the results. These include (1) ion exchange by diffusion in the lattice, or (2) nucleation and

growth of a new CZTSe phase. The XRD patterns (Fig. 2 in **Paper I**) showed the presence of either CZTS or CZTSe (with a small amount of S included), which rules out anion exchange by lattice diffusion. Therefore, the new CZTSe phase would be formed from the added Se-precursor and cations dissolved from he surface of the nanoparticles. The CZTSe phase nucleates and grows because it is more stable since it has a lower enthalpy of formation than the CZTS phase, and because the Se-amount made up 200% of the initial S-amount.

2.3.3.5   OUTCOME

The usefulness and relevance of this study can be discussed. Hopefully, it can be used as inspiration in the future if a system with a wide size distribution is needed. A polydisperse size distribution is normally a sign of lack of control in a colloidal system, as it can be difficult to control the size distribution in combination with the particle phase and composition. The synthesis route presented here, allows control of particle phase and composition while obtaining a wide particle size distribution. No matter what, we would like to avoid Se in our solar cells, so no more work on these particles was conducted.

2.3.4   LIGAND-FREE CZTS NANOPARTICLES

The aim of this project was to fabricate CZTS solar cells by spray-coating. A synthesis of good quality, ligand-free CZTS nanoparticles by the hot-injection method was therefore interesting to develop. First of all, the ink would be free from toxic constituents such as toluene, pyridine, and thiol-based solvents, and polar solvents in the form of water/ethanol mixtures can be used instead. In addition, polar solvents have the advantage that they permit direct solubilization of additional precursor chloride salts and beneficial dopants such as sodium, potassium, and antimony in controllable amounts [144]. Therefore, post-incorporation of dopants is circumvented. Furthermore, these particles would be "ligand-free", and no organic material from the ligands will remain in the film after deposition as was our main challenge when annealing the ligand-coated nanoparticle films (Chapter 5).

Ligand-free CZTS nanoparticles can be obtain either by ligand-exchange, or by synthesizing CZTS directly in suitable solvents. There exist examples of ligand-exchange with CZTS [107, 145], and it adds an extra step to the reaction. Ligand-free CZTS nanoparticles have previously been synthesized via the hydrothermal route. However, this synthesis approach is not suitable for safe, large scale production, as the synthesis is carried out in a stainless steel autoclave with an extremely high vapor pressure [30, 146]. Ligand-free CZTS nanoparticles have also been synthesized in a scalable manner, but without any significance whether the they are useful for a device-quality absorber layer [91].

To synthesize ligand-free CZTS, you need a solvent with a high boiling point as CZTS is formed around 220°C [108]. Some potential solvents are listed in Table 2.3. Inspiration for designing a new synthesis recipe was gathered from the hydrothermal synthesis, where glycols are typically used. In addition, one hot-injection synthesis recipe in the solvent TETA existed, but the resulting particles were not thoroughly investigated and the TETA solvent is expensive (374€ for 50 ml at Sigma Aldrich) [147]. Furthermore, TETA was used to successfully synthesize $Cu(In_{1-x}Al_x)Se_2$ nanoparticles [148].

Hence, mixing TETA and DEG could be a good place to start, as the boiling point of this mixture would likely be above 220°C. Chloride salts can be dissolved in ethylene glycol, but sulfur cannot, so we prepared the reaction flask with the cation chloride salts in DEG, and injected a S-TETA/DEG solution. The following section will present some of the work done leading up to the results in **Paper II**.

Table 2.3: Solvents considered for synthesis/dispersion of ligand-free nanoparticles [149, 150]. "DMSO" denotes dimethyl sulfoxide.

	Solvent	Boiling point (°C)	Polarity
Non-polar	Toluene	111	0.099
	Anisole	154	0.198
	Hexane	68	0.009
	Oleylamine	348-350	
Polar	Ethanol	78	0.654
	Water	100	1
	DMSO	189	0.444
	Ethylene glycol (EG)	197	0.790
	DEG	245	0.713
	TETA	266-267	

2.3.4.1 COMPOSITIONAL TUNING

Changing the type and amount of the metal salts used allowed us to tune the elemental composition. The influence of metal salt type and concentration on composition is showed in Table 2.4. Samples P7 and P8 both have satisfactory compositions. The composition cannot always be predicted based on the initial salt concentrations, but in certain cases the colloidal system behaves as expected. For example, by increasing the amount of Zn-salt from synthesis P3 to P4, an increase in Zn-amount in the synthesized product is seen. The final synthesis recipe, P8, was used for the annealing studies in **Paper IV**. Note that the molar concentration of the initial Zn-salt exceeds that of the Cu-salt, and the synthesized product still ends up with more Cu than Zn. This can be explained by different reactivities of the salts, where chlorides in principle should be more reactive than acetates.

The yield of synthesis P7 was calculated to 80 mg, when assuming that all Cu (which is the limiting constituent) is used for the reaction. The powder was dried in air for one day, and the mass of the dried powder was 150 mg. The difference is due to residual solvent molecules. If all powder including the residual solvents was used for deposition of 1 μm thin film, it would result in an area of 0.36 m^2.

The reproducibility of the synthesis was determined by repeating the same synthesis five times, and another one four times. This resulted in elemental ratio variations listed in Table 2.5. Here, quite large standard deviations occur for the synthesis repeated five times, and this measurement batch also contained one outlier. The errors stem from EDX measurement uncertainty, weighing of chemicals (especially tin chloride but also copper chloride salt tend to absorb water), and temperature control. The relative standard deviation (RSD) is also associated with the repeatability, and the RSD of the two syntheses are listed in Table 2.6. If RSD≤20% the measurement is said to be in good agreement, which in this case they are.

Table 2.4: Effect of varying metal salt on elemental composition. The composition is presented as if the synthesized phase is CZTS, but in fact it could be a combination of binary and ternary phases as well. Most of these syntheses and corresponding data was carried out and collected by Naghmeh Mirbagheri.

Sample	Cu-salt (mmol)	Zn-salt (mmol)		Sn-salt (mmol)		Composition
	CuCl$_2$·2H$_2$O	ZnCl$_2$	Zn(OAc)$_2$	SnCl$_4$·5H$_2$O	SnCl$_2$·2H$_2$O	
P1	0.5	0.32		0.25		Cu$_{2.5}$Zn$_{0.2}$SnS$_{3.2}$
P2	0.5	0.32			0.2	Cu$_{2.8}$Zn$_{0.3}$SnS$_{3.0}$
P3	0.5		0.4	0.25		Cu$_{2.7}$Zn$_{0.6}$SnS$_{3.9}$
P4	0.5		0.6	0.25		Cu$_{2.1}$ZnSnS$_{2.9}$
P5	0.4		0.6	0.2		Cu$_{2.3}$Zn$_{1.4}$SnS$_{4.1}$
P6	0.4		0.45	0.2		Cu$_{2.3}$Zn$_{1.3}$SnS$_{4.1}$
P7	0.35		0.5	0.23		Cu$_{1.9}$Zn$_{1.3}$SnS$_{3.6}$
P8	0.35		0.55	0.23		Cu$_{1.9}$Zn$_{1.2}$SnS$_{4.3}$

Table 2.5: Reproducibility of synthesis. The elemental ratios are average of x measurements, and the standard deviations are calculated as the standard deviations of the averages.

Repetitions x	Cu (at.%)	Zn (at.%)	Sn (at.%)	S (at.%)
5	23.95 ± 1.25	14.08 ± 2.18	14.47 ± 3.36	47.50 ± 2.03
4	24.51 ± 0.59	14.88 ± 1.55	13.33 ± 0.82	47.26 ± 0.70

Table 2.6: RSD of two syntheses repeated 4 and 5 times. If the RSD is less than 20%, the measurement is said to be reproducible. The RSD are calculated like the standard deviation for the measurement divided by the total mean (Table 2.5).

Synthesis number	Synthesis 1				Synthesis 2			
	Cu (%)	Zn (%)	Sn (%)	S (%)	Cu (%)	Zn (%)	Sn (%)	S (%)
1	5.6	7.7	4.4	3.9	4.5	4.5	6.9	3.1
2	3.1	3.5	3.7	1.7	4.1	3.9	10.3	2.6
3	0.6	2.8	2.8	1.6	3.1	12.4	10.4	3.3
4	1.4	2.7	3.7	0.5	1.5	3.0	17.0	5.0
5	4.1	17.9	8.3	4.2				

2.3.4.2 Crystal phase determination

We determined the crystal phase of the material in two ways: X-ray diffraction and electron diffraction. One main difference between these techniques is the sample volume, where XRD can probe samples of several millimeter in diameter, while for TEM diffraction a single nanoparticle is investigated. The XRD patterns of sample P2-P8 are displayed in Fig. 2.14, where P5, P6, and P8 appear to be phase-pure (and possibly P4). Many different peaks are seen for sample P2, and in addition to CZTS the suggested phases include SnS, $Cu_3SnS_{3.6}$, Cu_4SnS_4, and ZnS. One of the samples with the best composition according to EDX (sample P7) contained a SnS_2 secondary phase, and Sn-S phases were quite often observed in near-optimal composition samples.

Sample P6 was chosen for further investigation (*i.e.* sample E in **Paper II**), and its selected area diffraction (SAD) pattern is showed in Fig. 3.e in **Paper II**. The *d*-spacings could be measured from the SAD pattern, and the results are listed in Table 2.7 as *Measured*. The *d*-spacings were also determined by extracting the numbers from a radial intensity plot (*Extracted from software*). To assign Miller indices, the *d*-spacings were calculated for the planes in the CZTS crystal. For tetragonal crystal structures,

$$\frac{1}{d^2} = \frac{h^2 + k^2}{a^2} + \frac{l^2}{c^2} \tag{2.10}$$

where h, k, and l signifies the Miller indices. Given the lattice constants in Table 1.1, the resulting *d*-spacings and lattice planes found can be seen in Table 2.7 as *Calculated*. These data are consistent with the obtained XRD pattern of this sample and the CZTS phase.
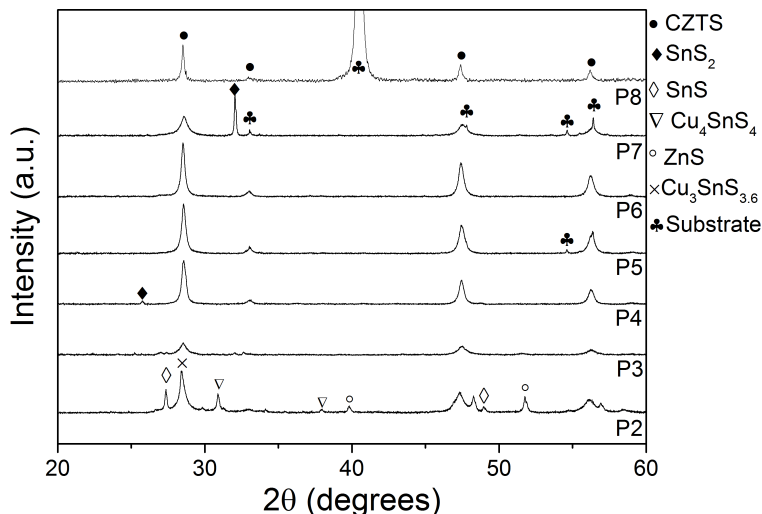
Figure 2.14: XRD patterns of selected nanoparticles. All samples display the typical CZTS peaks, but in sample P2 and P3 many other peaks are detected. XRD measurements taken together with Naghmeh Mirbagheri.

2.3.4.3 Secondary phase determination

Fig. 2.15 shows the Raman spectra of sample P2-P8. Sample P2 displays a Raman shift of 314 cm^{-1} and a broader peak at 337 cm^{-1}. The peak at 314 cm^{-1} could be either a Cu-Sn-S compound or the SnS$_2$ phase (refer Table 2.1), and the broad peak could be CZTS. The remaining samples all have the main CZTS peaks, but shifted between 331 and 337 cm^{-1}, which indicates the existence of Cu–Zn disorder within the CZTS lattice of the peaks shifted from 337 cm^{-1} [151]. Samples P3, P7, and P8 furthermore show the presence of SnS. In accordance with the best XRD pattern and elemental composition, Cu-rich sample P6 have the sharpest Raman peaks.

When observed in a scanning electron microscope (SEM) for EDX, some of the samples showed plate-like features (Fig. 2.15(b)) that after further characterization were found to be Sn-rich. Accordingly, SnS typically grows in this manner [127]. For sample P8, SnS appeared on both the Raman spectrum and could be detected with EDX, but was not detected on the corresponding XRD pattern, which could be because SnS is located only on the surface.

Table 2.7: *d*-spacings and Miller indices extracted from the SAD pattern of sample P6, and calculated for the kesterite.

Miller indices	*d*-spacings (Å)		
	Calculated	Measured	Extracted from software
(112)	3.136	3.1293	3.1361
(220)	1.921	1.9131	1.9229
(312)	1.638	1.6302	1.6355
(224)	1.568	1.5568	1.5845
(008)	1.357		1.3568
(332)	1.247	1.2385	1.2457

(a)   (b)
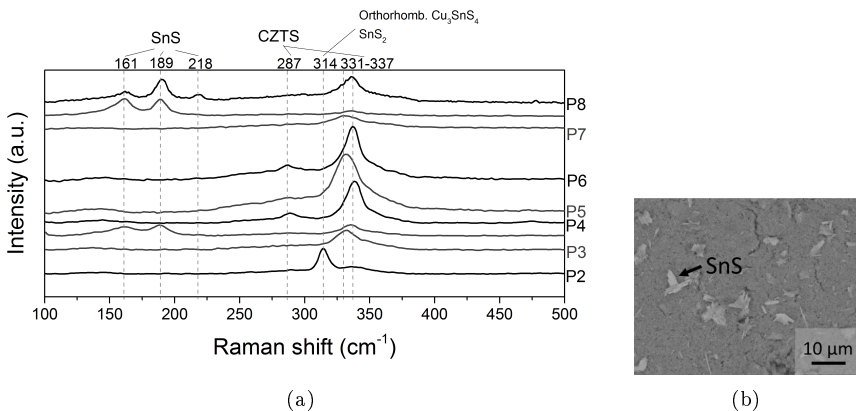
Figure 2.15: (a) Raman spectra of selected nanoparticles with potential secondary phases. Raman measurements taken by Andrea Crovetto and Stela Canulescu. (b) SnS flakes in the as-synthesized P8 nanoparticles, but seen for several samples.

2.3.4.4 SIZE DISTRIBUTION OF NANOPARTICLES

The size distribution is a useful characteristic of the synthesis product. It is relevant for coating techniques such as spray-coating, where the nozzle size should be determined from the particle size. With this in mind, the size distribution of the P6 nanoparticles was determined by measuring the diameter of 287 particles. This was done by manually outlining the particle perimeters in Image J, and by assuming a spherical shape to calculate the diameter. Typical particles used for determining the sizes are indicated in Fig. 2.16. The measurements were challenged by particles aggregate so the particle perimeter was not always clearly defined. We therefore compiled a list of considerations on how to obtain a representative size distribution, which can be seen in Appendix B.

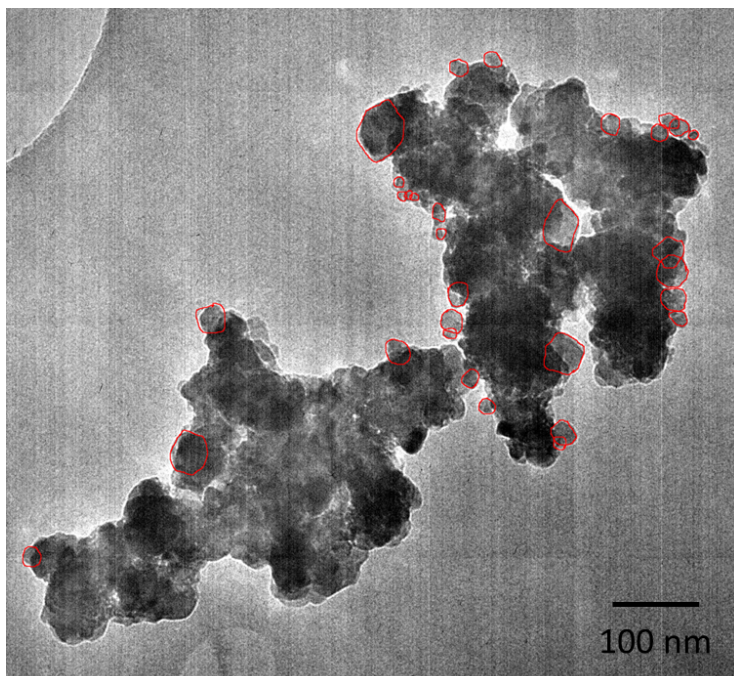The synthesized nanoparticles are irregular and have faceted morphologies. The

Figure 2.16: Example of how the areas of the nanoparticles were determined in Image J.

diameter of the synthesized nanoparticles was found to be within the range of 2.5-81.5 nm with an average particle size of 23 nm and a standard deviation of 11 nm, which is among the largest CZTS nanoparticles synthesized in an organic polar solvent [91, 93, 96, 97, 30]. The particle size distribution was constructed with an optimum bin size calculated according to the work reported by Diaconis *et al.* [152]. The error on the average particle size was estimated to be 13% by considering 10% TEM magnification calibration error and the error that arose from the manual determination of the particle sizes[10].

2.3.4.5   EFFECT OF SYNTHESIS TIME

To investigate the effect of synthesis time, two syntheses were carried out and particles were extracted after 2 min, 5 min, 10 min, 20 min, 40 min, 80 min, and 120 min. The XRD patterns are displayed in Fig. 2.17. Of the examined samples, sample P4 in (a) appears phase-pure CZTS, while sample P7 in (b) displays a SnS_2 secondary phase. Already after 2 min, the CZTS phase is detected. From this point, the peaks sharpen. The crystallite size, which was

---

[10]The error on the manual determination of particle sizes was determined by two people measuring the same 15 particles, and comparing the results.
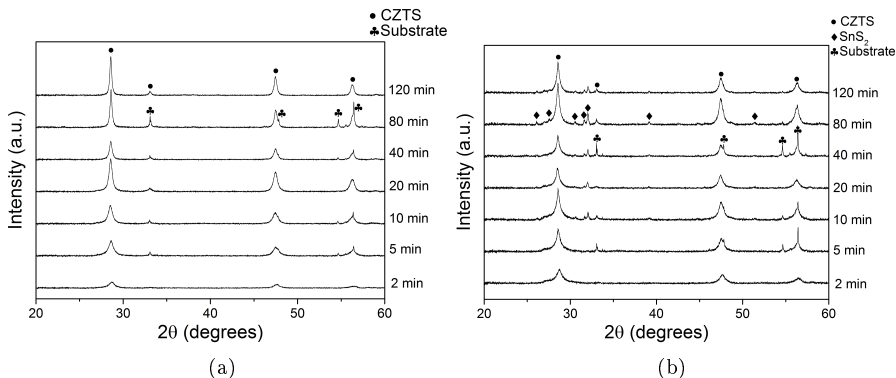
Figure 2.17: XRD patterns as a function of reaction time, for samples similar to (a) P4 and (b) P7. All samples display the typical CZTS peaks, but a SnS_2 phase could also be detected in (b). Synthesis and XRD measurements by Naghmeh Mirbagheri.

calculated with the Scherrer equation and the FWHM of the main kesterite (112) Bragg reflection, is plotted in Fig. 2.18. The particles appear to grow within the first 10 min of reaction, whereafter the growth saturates around 25 nm, which is close to the 23 nm determined from TEM characterization. This is a good demonstration of that under normal synthesis conditions, the particle size saturates, and perhaps a shorter synthesis time would be sufficient[11].
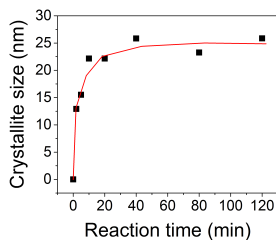

Figure 2.18: Crystallite size as determined from the Scherrer equation as a function of synthesis time for sample P7.

2.3.4.6 OUTCOME

The novel nanoparticle recipe developed here results in cheap, reasonably reproducible nanoparticles with a desired composition and phase. The average size was determined to be 23 nm from TEM characterization and a similar result

---

[11]I did not change the synthesis time accordingly, since all characterization was done for the nanoparticles synthesized for 2 h.

was found from the Scherrer equation of the XRD peaks. There is still some difficulties in controlling the formation of a Sn-S phase in the synthesized material, and it is only seen for some syntheses. Limiting the Sn-amount could potentially help. Besides, Sn-S is prone to evaporate during annealing, so having more Sn is not necessarily detrimental. Therefore, the synthesized product was acceptable, and other parts of the solution-processing route to fabricating thin-film solar cells were investigated.

2.3.5   NANOPARTICLE SURFACE COATING

The presence or absence of hydrocarbon ligands on the surface of the nanoparticles was investigated with FTIR. The ligand-coated nanoparticle sample in Fig. 2.19(a) shows a strong signal in the range of 2800-3000 cm^{-1}, which corresponds to the C-H vibrational frequency of oleylamine [131, 153]. The peaks at 1625 cm^{-1}, 1465 cm^{-1}, and 1375 cm^{-1} could also be matched with oleylamine. The broad band at 3000-3700 cm^{-1} is attributed to O-H stretching of water molecules in the solvent, but could also stem from N-H stretching. In comparison, the ligand-free nanoparticle samples (zoom-in in Fig. 2.19(b)) show no strong signal for C-H stretching, and confirm their ligand-free nature. To be more specific about the term "ligand-free", I would like to point out that we actually mean "hydrocarbon ligand-free". Both water and amines could be regarded as ligands, and could potentially occupy the surface of the nanoparticles. The broad band at 3000–3700 cm^{-1} is also present in this sample, and it can be attributed to O–H stretching of ethanol or water residues. However, this zone overlaps with N-H stretching (3200-3500 cm^{-1}), and we cannot eliminate the possibility that we have amine functional groups from TETA surrounding the nanoparticles. The remaining peaks are also close to peaks observed for FTIR spectra of ethanol, TETA and DEG [153].

The amount of washing the ligand-free nanoparticles influenced the FTIR spectra. For example, more intense peaks were seen when washed only twice, compared to three times (Fig. 2.19(b)). It is hard to give a number on the optimal number of washes. On one hand, it is good to have as little contaminants on the surface of the particle as possible, but on the other hand, this makes it more difficult to disperse the particles in a solvent. Depending on for what the particles should be used, different treatments should be considered.
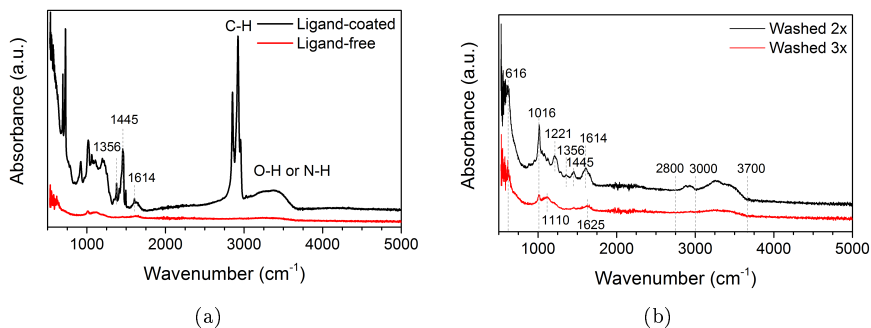
Figure 2.19: FTIR spectra of (a) ligand-coated and ligand-free sample, and (b) the effect of washing the ligand-free nanoparticles (sample P7). FTIR measurements acquired with assistance from Jean-Claude Grivel.

2.4 OUTLOOK

In this chapter, several different recipes and methods to synthesize CZTS(Se) nanoparticles, each with a different objective, have been presented. To start with, the one-pot method was attempted, but due to lack of reproducibility and ergo lack of control, no significant improvements could be achieved. These nanoparticles were nonetheless used for thermal analysis, thin-film coating and sulfurization experiments, for samples where the composition was satisfactory. Improvements to the temperature control could be done either by using a heating mantle with included temperature-control, or by making a compartment such that the thermocouple can be placed in the same position every time.

The work on synthesis of CZTSe nanoparticles through a two-step hot-injection method provided some insight into an alternative way to get large particles and a wide size distribution, with a relatively good control over the composition. However, as we would like to avoid Se in the solar cells, this material was not used to make any devices.

As the aim of the project was to fabricate thin films by spray-coating, we wanted to have nanoparticles dispersed in a water/ethanol-solution. In addition, this would limit the organic material residue in the films. This was achieved by choosing suitable salts and solvents. The composition could be tuned to the optimal range, but the corresponding XRD patterns and Raman spectra of these samples showed some Sn-S secondary phases. However, the elemental composition and phases can change during annealing, so the material presented here was used for further analysis.

Finally, we confirmed the hydrocarbon ligand-coated and ligand-free nature of the particles synthesized by the one-pot method and the ligand-free synthesis, respectively.

Looking back, improvements to the setup would have made the experimental work more efficient. Higher through-put screening of synthesis conditions could be obtained by setting up several reaction flasks to run simultaneous reactions. This requires more heating mantles and glassware, but would also allow investigation of more of the parameters.

Chapter 3

Thermal Analysis of Cu₂ZnSnS₄ Nanoparticles and Inks

This chapter contains thermal characterizations of nanoparticle inks and powders that aid in the understanding of what goes on during annealing. Thermal analysis describes how properties of materials change with temperature, and here we monitor the mass, heat flow, and crystallinity in different atmospheres. As an additional characterization tool, mass spectrometry is used for detection of volatile species leaving the sample.

3.1 Introduction

Once the nanoparticle or precursor ink has been formed, it should be deposited as a thin film. This is normally done by multilayer depositions, with separate *pre-annealing* steps in between. The goal of the pre-annealing step is to remove residual solvent and capping ligands. The following techniques were chosen for the investigation:

- **Thermogravimetric analysis (TGA)** provides a correlation between temperature and mass, and thus gives a temperature of when the solvent/ligands decompose.
- **Differential thermal analysis (DTA)** can reveal whether the thermal events were exothermic or endothermic, *i.e.* whether sintering/crystallization or thermal decomposition occurs[1].
- **Mass spectrometry (MS)** provides information on which gases decomposes at which temperature, and perhaps also on how they decompose.

---

[1] The sintering signal from the DTA measurement would be very hard to detect, as it is a slow process that does not use large amounts of energy.

- **In-situ annealing in XRD** can reveal whether the crystal phase changes, whether any secondary phases are formed and at what temperature, and furthermore if grain growth occurs.

One important parameter is believed to be the annealing atmosphere, and all TGA-MS characterizations were carried out in three different atmospheres: oxidizing (air), inert (N_2), and reducing (forming gas, *i.e.*, 4.5% H_2 in Ar). Both ligand-free and ligand-coated nanoparticles were studied, as well as both inks and powders.

3.2 Experimental details

3.2.1 Thermogravimetric and differential thermal analysis

TGA and DTA were carried out on a Netzsch STA 409CD. A corundum (Al_2O_3) crucible was used with a pierced lid for liquid samples, and without a lid for powder samples. The flow rate was set to 100 ml/min. The temperature profile was chosen to resemble a typical annealing done in practice, with a heating rate of 12 K/min up to 550°C, followed by an isothermal step at this temperature for 1 h. Considerations on choosing the right experimental conditions for a measurement are described in Appendix C, together with a check-up on the temperature accuracy and calibration of the heat flow. The data was analyzed with the Proteus61 software.

3.2.2 Mass spectrometry

Mass spectrometry was carried out with a Netzsch QMS 403 C Aëolos. It can measure a mass range from 1 to 300 amu (resolution >0.5 amu), with electron impact ionization of 70 eV, detector type Channeltron SEM with detection limit of >1 ppm, and a scan rate of 2 s/amu. The temperature of the entire gas transfer system was heated to its maximum, 300°C, before the start of the measurement.

3.2.3 In-situ X-ray diffraction

The crystallinity of the nanoparticle powders as a function of temperature in air and nitrogen was determined with XRD from Bruker D8 Advance, with a $\theta/2\theta$ scan speed of 0.01°/min in between 20-80°, and Cu K_α- radiation (λ=0.15418 nm). The temperature profile chosen was with a heating rate of 5°C/s, and with a 300 s delay time at every reached new temperature. A measurement was carried out every 50°C from 50°C to 550°C, whereafter it was cooled to 30°C. The total scan time at each temperature was 56 min. The peaks are not corrected for K_{α_2} splitting at this stage.

3.3   RESULTS AND DISCUSSION

The main results from the thermal analysis of the nanoparticle inks and powders can be seen in **Paper III**. A summary of the these findings as well as relevant non-published data will be presented in this section.

3.3.1   SUMMARY OF FINDINGS IN PAPER

In the paper you will find a comparative study of the thermogravimetric behavior or nanoparticles with and without hydrocarbon ligands. We find that the mass of a ligand-free nanoparticle powder decreases continuously from room temperature to about 500°C in inert and reducing atmosphere. In the isothermal step, the mass continues to decrease at a lower rate, and slightly more in reducing atmosphere indicating its slight superiority as a more reactive gas. The mass loss of about 10% of the initial mass is linked to evaporation of residual solvent molecules in the dry power. According to the yield calculations in Section 2.3.4.1, the CZTS mass should be approximately 80 mg, while the weighted mass was 150 mg. In this respect, a 10% mass loss only lowers the mass to 135 mg, and thus some residual organics should still remain.

For a ligand-coated nanoparticle powder we see a total mass loss of about 20% in inert and reducing atmosphere, which begins at 250°C. From this temperature two main mass loss steps are seen, one with an onset at 350°C and one at 425°C. This is owing to the thermal decomposition of the oleylamine ligands and other residual organic species. Oleylamine has a boiling point of 364°C, but as it is bound to the nanoparticles, more energy is required for its decomposition. Since the transfer line was 300°C, whole oleylamine molecules would be difficult to detect. As for the ligand-free nanoparticle powder, the decomposition in reducing atmosphere occurs at a higher rate than in inert atmosphere.

With a mass spectrometer, water, organic fragments, alcohol and amine functional groups were detected. This was expected, apart from the amine in the ligand-free nanoparticle powder. The FTIR spectrum did not show any signs of this, but an amine is used in the synthesis and could very well partly functionalize the surface. In addition, sulfur dioxide and carbon dioxide were found. The signal from sulfur dioxide was particularly present for the ligand-free ink at a higher temperature. It is slightly worrying for the correctness of the interpretation that the oxides are seen, because it could mean that the partial pressure of oxygen in the chamber is not sufficiently low. On the other hand, the oxygen could also come from the solvents or an oxide on the surface of the nanoparticles, and it was seen in a similar study [154].

Finally, **Paper III** shows SEM images of the powder that remains after analysis. These were interesting as they resemble typical thin films after annealing in

Chapter 5 in terms of grain growth formation and porosity. In short, for the ligand-coated nanoparticle powders, grains grow on the surface of the films, which means that the ligand decomposition occurs mainly at the surface. For the ligand-free nanoparticle powders, large grains are formed[2]. When ink samples were imaged, a high degree of porosity was seen as a characteristic consequence of solvent evaporation.
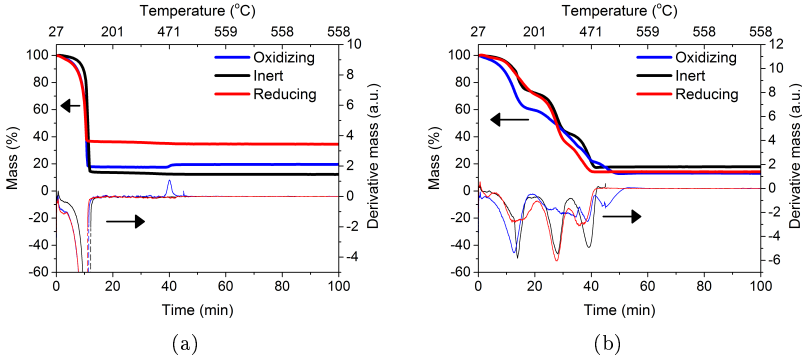

Figure 3.1: TGA curves for ligand-free (a) and ligand-coated (b) nanoparticle inks in different atmosphere. The temperature increases with 12 K/min until 560°C, where the temperature is kept for 1 h. The different base-levels stem from slight variations in concentration of the particles in the inks.

3.3.2 THERMOGRAVIMETRIC AND DIFFERENTIAL THERMAL ANALYSIS

To gain more insight into how the solvents evaporate, inks consisting of roughly 10% nanoparticles were characterized. The ligand-free nanoparticle inks in Fig. 3.1(a) only show one sharp mass loss stage between room temperature and approximately 96°C, with an onset between 63-69°C. The solvent consisted of 10% ethanol and 90% water, with boiling points of 78°C and 100°C, respectively. The onset of solvent removal for the ligand-free nanoparticle ink in inert atmosphere is later than in oxidizing and reducing atmosphere, but this could be due to higher mass of the sample in inert atmosphere.[3] Once the ink samples have reached the isothermal step, no significant mass change can be detected,

---

[2]The large grains were also seen for some ligand-free nanoparticle thin films that will be showed in Chapter 5, but only when sodium was added. The result here is therefore slightly questionable since no further characterization was done on the sample, but it is possible that the annealing conditions in the TGA could result in CZTS grains.

[3]The samples masses used were: m_{air}=13.02 mg, m_{N_2}=28.62 mg, and m_{H_2}=16.16 mg. The sample mass should be similar when comparing two experiments, as a low mass will have a higher resolution for TGA but lower DTA signal than a high mass. For high mass samples, the heat distribution takes time, and this will smear out the kinetics, and thus give lower resolution, but the signal will increase and provide a better signal-to-noise ratio.

except for the sample in oxidizing atmosphere that experience a 10% gain in mass.

Similarly, TGA was carried out on inks consisting of the ligand-coated nanoparticles in oleylamine (Fig. 3.1(b)). The decomposition occurs in three steps. Initial solvent decomposition takes place with the highest rate in air up till $250°C$. At $250°C$ the mass loss in inert and reducing atmosphere appears very similar, while above $350°C$, the rate of decomposition in reducing atmosphere exceeds that in inert atmosphere. From this we can see that initial annealing in oxidizing atmosphere, followed by a high-temperature annealing in reducing atmosphere would be most effective in removing the organics/leftover solvent for a ligand-coated nanoparticle ink.

The DTA curves did not reveal a crystallization signal, and are showed in Appendix C.
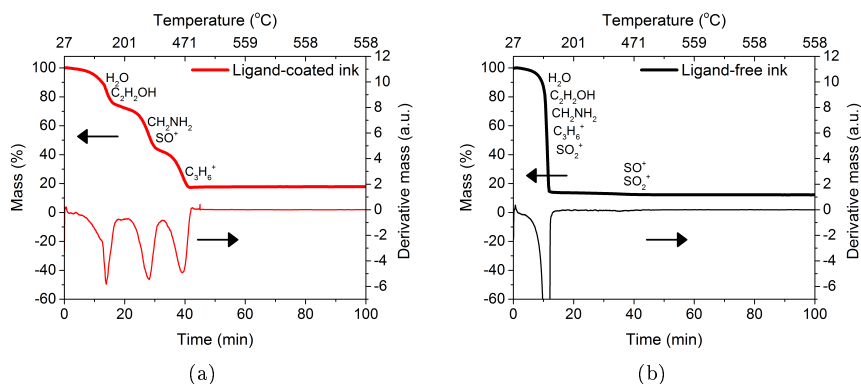

Figure 3.2: Ligand-coated (a) and ligand-free (b) nanoparticle inks with MS detected signals. Each species is placed at the mass loss step where the MS signal is highest. For the ligand-free ink, SO_2 is detected around $450°C$.

3.3.3   MASS SPECTROMETRY

Thermal decomposition is an endothermic chemical process, where energy in the form of heat is used to break up chemical bonds. Normally, the precise reaction pathway for such reactions is unknown, since a molecule may break up into a variety of smaller fragments [155]. We have tried to identify which molecules are released from the nanoparticles during annealing, to get an idea how this thermal decomposition and also evaporation would proceed. Fig. 3.2 shows the TGA curves for the inks in inert atmosphere, and the species detected with MS are placed on its primary corresponding mass loss step, for a simplified view. As expected, ethanol and water are detected in the first mass loss step

for the ligand-coated nanoparticle ink, while the amine group is seen at 350°C (corresponding to the boiling point of oleylamine). At 450°C organic fragments are released. For the ligand-free nanoparticle powder, all species are detected at around 100°C, except from sulfur dioxide which peaks around 500°C. The intensity of all these species as a function of temperature can be seen in Fig. 4 in **Paper III**.

3.3.4   IN-SITU X-RAY DIFFRACTION

The final thermal analysis technique used was *in-situ* XRD as a function of temperature. The XRD patterns for annealing in air are displayed in Fig. 3.3(a). The peaks shift to lower angles as the temperature is increased, as a result of thermal expansion in the lattice. An overview of the 2θ peaks can be seen in Fig. 3.3(b), where the main CZTS (112) peak disappears after 350°C, but starts to degrade already at 50°C. The final XRD pattern is plotted in Fig. 3.4(a), *i.e.* when the material is cooled back to 30°C. Before annealing (Fig. 3.3(a)) the peaks match pure-phase kesterite CZTS. After air-annealing, the kesterite CZTS phase is non-existing, and instead many oxide secondary phases appear (Fig. 3.4(a)). The phases indicated are just a few of the possible oxide phases that could exist. Interestingly, when the same measurement was carried out in nitrogen atmosphere, a similar result was obtained (Fig. 3.4(b)), but for this experiment the kesterite CZTS phase disappears after 400°C.

This emphasizes the importance of a very tightly closed annealing chamber, and raises the question whether the STG 409CD instrument has the required low amounts of oxygen to avoid seeing the material degrade. An easy way to test this, would be to characterize the final material by XRD or EDX, but more material has to be measured[4]. Based on eye-inspection, no colour-change was seen for the samples after TGA in inert and reducing atmosphere, while the samples in air turned white.

3.4   OUTLOOK

The aim of this thermal analysis was to determine the effect of the annealing atmosphere. Unfortunately, no variation was seen for inert and reducing atmosphere, apart from that the mass loss was somewhat more pronounced in reducing atmosphere, as was also expected. When annealed in air, CZTS starts to decompose already at 50°C, and the rate of oxidation will of course depend on the time the material experiences an elevated temperature as seen from the in-situ XRD measurement. The mass spectrometry analysis is tedious but it showed how the ligands decompose in the sample. The outcome of this study are certain temperatures, which can be used for pre-annealing the films. For

---

[4]Unfortunately, the relevant equipment was not available in the months after the analysis.

the ligand-free particles, a temperature above 100°C should be applied. For the ligand-coated particles, part of the ligands would be removed at 200°C, 350°C, and 425°C. Decomposition will occur if the sample is left at these temperatures for longer times. A temperature of 200°C was chosen as the pre-annealing temperature, due to the risk of oxidation and temperature limit of the hotplates used.

The DTA measurements could be repeated with a larger sample mass, as this could enhance a potential crystallization signal. Furthermore, in Chapter 5 we found that adding Na increases grain growth, which could also be attempted here at different temperatures.

If I were to repeat this analysis today, I would use larger sample masses which would allow easier characterization of the remaining product.
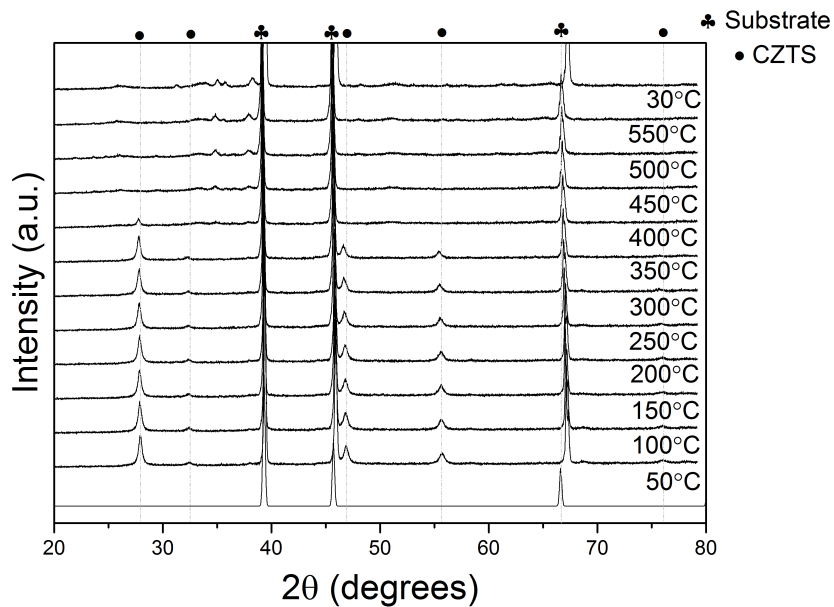
(a)
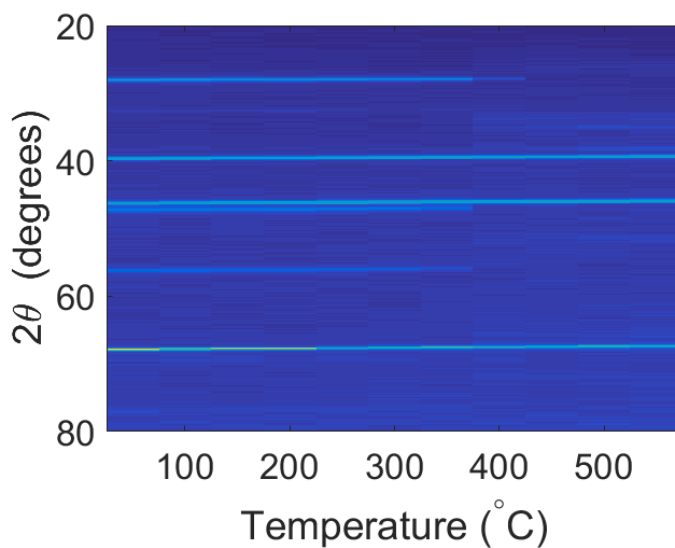
(b)

Figure 3.3: In-situ XRD patterns in air as a function of temperature (a), where the diffractogram at the bottom is the Pt substrate. An overview of the 2θ peaks (b) shows that the decomposition temperature in air is 350°C, but this plot also reveals that the peak intensities decrease already from annealing at 50°C.
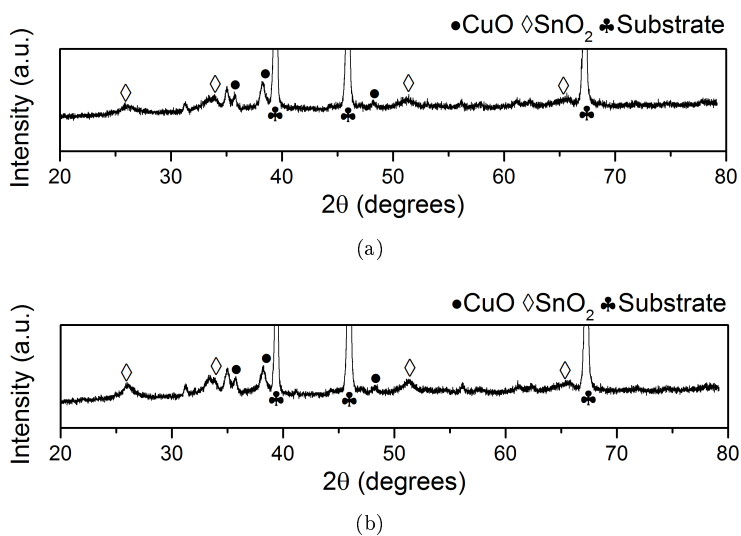
(a)

(b)

Figure 3.4: Remaining material after in-situ XRD, in (a) air, and (b) nitrogen. Potential oxides formed are marked, but several other phases could also be present. The ICSD coll. codes of CuO is 16025 and SnO_2 is 9163.

Thin-Film Deposition

This chapter briefly presents the deposition techniques used to form thin films with a thickness of about 1 μm by solution-processing. An overview of the techniques is given, followed by a description of the experimental setups, and general results and observations. Finally, ideas on how to improve the reproducibility of these coating methods will be given.

4.1 Introduction

Thin-film deposition can be categorized either as coating or printing; printing implies a method where a layer of ink is transferred from a stamp to a substrate, and coating describes the process of casting the ink onto a substrate. In other words, printing is distinguished because it can be used to make complex patterns according to the definition by Krebs [81]. For lab scale research, techniques such as spin-coating, doctor blading[1], and drop-casting are suitable, while for mass production gravure coating, knife-over-edge coating, spray-coating and printing (ink-jet printing, and screen printing) are more desirable for high-volume production [81]. For CZTS, films have been deposited by spin-coating [29, 31, 97, 146], spray-coating [26, 156], doctor blading [28], dip-coating [157], roll-to-roll (R2R) printing [30], and ink-jet printing [156].

4.2 Experimental details

Dried nanoparticle powders were dispersed in suitable solvents to formulate the inks, followed by deposition. The solvents used for deposition were purchased and used without further purification. They include: 1-octanethiol ($CH_3(CH_2)_7SH$, $\geq 98.5\%$) from Sigma Aldrich, toluene and isopropanol (99.8%) from Merck Millipore, and ethanol (96%) from VWR Chemicals.

---

[1] Doctor blading is R2R compatible as the up-scalable knife-coating.

4.2.1 SUBSTRATE PREPARATION

A clean substrate surface is essential for solar cell fabrication. Contamination could originate from fingerprints, dust particles, oils from substrate fabrication, hairs, and paper fibers from packaging or cleaning, and would result in poor film adhesion, crack/pore formation, and thus electronic defects in the film. Coating the surface or in other ways treating it chemically can also enhance film adhesion, but this could also affect the electronic properties in unknown ways [83].

In this work, substrates used for deposition were sonicated in a solution of 50% ethanol and 50% DI water for 10 min. Afterwards, the substrates were taken out of the mixture and rinsed with ethanol. The substrates were then blow-dried with a flow of nitrogen. Mo-coated soda-lime glass (SLG) was used as the substrate, which also introduced good spreading of the inks.
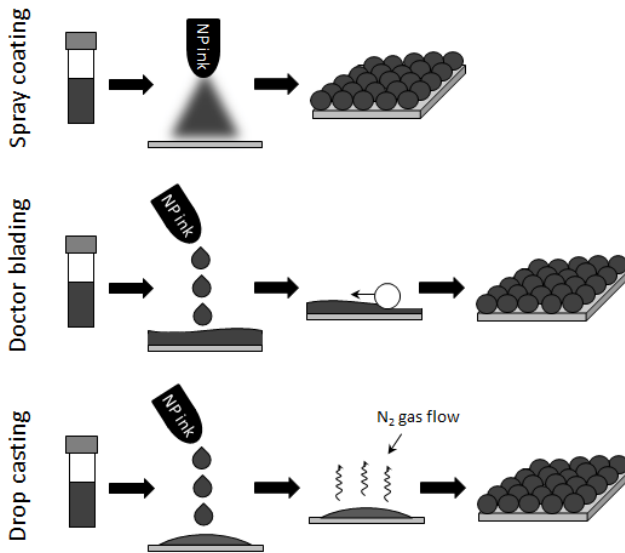

Figure 4.1: Schematical overview of deposition techniques. The thin films will consist of more than a monolayer of nanoparticles, but illustrated here as such for simplicity. For drop-casting, a flow of nitrogen expedites drying and results in a more uniform layer.

4.2.2 THIN-FILM DEPOSITION

In this work, three different methods were used for deposition: spray-coating, doctor blading, and drop-casting. The principles of all methods are illustrated in Fig. 4.1. By spray-coating an ink is forced through a nozzle to form a

fine aerosol, and a carrier gas directs the aerosol to the substrate. The aerosol will dry upon impact with the substrate [81, 158]. For spray-coating we have used ligand-free nanoparticles, as these could be dispersed in water and ethanol. Doctor blading is a type of knife-coating technique, where a solution is spread across a substrate with a rod or a knife, and in the present work it was used for the ligand-coated nanoparticles. The third method, drop-casting, relies on the solvent to evaporate such that a thin film is formed, and could be done on either type of nanoparticles, but was mostly used for the ligand-free ones.

The structural evolution of the film is believed to depend on few solvent properties. One is the ink quality, which determines how well the nanoparticles are dispersed in the solvent. When the ink quality is not optimal, the film will become non-uniform and thickness variations will occur. Another factor affecting film formation is the vapor pressure of the solvent. Short-chained alcohols with high vapor pressure are commonly used to deposit films of thickness of the order of tens of nanometers, and low volatility solvents are used to fabricate layers of tens of micrometers. The viscosity of the solution is also an important property affecting film thickness and cracking tendency. Tensile stress is generated within the film during drying as the solvent is removed, which will lead to cracking. As the film gets thicker, the tensile stress increases. This can be avoided by depositing multiple layers, and also by using lower vapor pressure solvents [83].

Heat treatments are typically applied after deposition, both to remove residual solvent molecules and to enforce crystallization and densification in the film. We saw in Chapter 3 at which temperatures residual organic species from the solvent and surfactants were removed. This chapter will cover this *pre-annealing* step, as it is used between the depositions for multiple layers, but the *sulfurization* is covered in depth in Chapter 5.
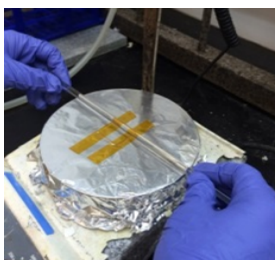

Figure 4.2: Doctor blading setup, where a glass substrate is taped to a hotplate with thermal tape. The glass rod is used to spread the ink on the substrate.

4.2.2.1 DOCTOR BLADING

Doctor blading was carried out on a hotplate with a glass rod (Fig. 4.2). High temperature tape (from Tesa, which can resist 350°C for 10 h, and of a thickness

of 60 μm) was used to keep the sample in place, and functioned as a spacer between the rod and the substrate.

Inks were formulated from mixtures of toluene and octanethiol. How many washing cycles the nanoparticles had gone through would influence how much of each solvent was required to disperse the nanoparticles. For example, when the particles are washed, it would be more likely that some oleylamine ligands are removed, and it would be harder to disperse the particles. In this case, adding slightly more octanethiol would aid the dispersion, and as would longer sonication time.

For a typical ink, 20 drops of a solution of 1:2 octanethiol:toluene were added to a powder that had been washed three times. The mass of the nanoparticles was 200 mg. The ink was sonicated for 30 min. Before deposition, all equipment was cleaned thoroughly in isopropanol. One drop of the nanoparticle ink was placed on a substrate of 1 cm×2 cm, and firmly spread with the glass rod. The sample was heated to 200°C in 40 min, and left at this temperature for 20 min, whereafter the sample was removed from the hotplate and cooled to room temperature. The coating and drying were repeated for a total of three layers.
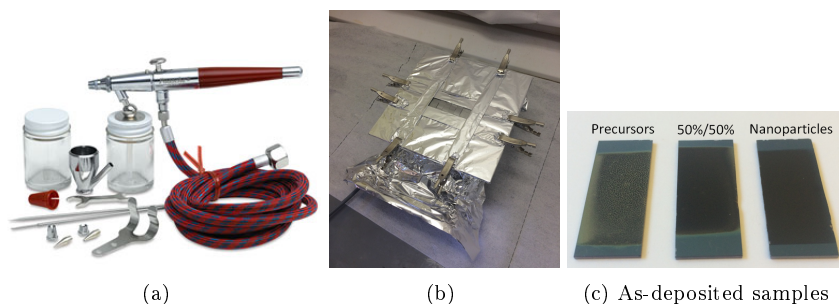

(a)   (b)   (c) As-deposited samples

Figure 4.3: Spray gun (image from [159]) (a), spray-coating stage (b) where Al-strips are used to secure the samples on the hotplate while spraying, and (c) images of as-deposited samples.

4.2.2.2 SPRAY-COATING

Spray-coating was performed with an airbrush from Paasche (Model VL Double Action) that was connected to a nitrogen flow (Fig. 4.3(a)). The nozzle with the smallest needle (VLM-1, corresponding to spray patterns of down to 0.4 mm) was used, and it was positioned such that the smallest possible volume was ejected. The hotplate used for deposition (Fig. 4.3(b)), was a hotplate (from Heidolph, type MR 2002) with an Al-plate attached for uniform heat distribution. Thin Al-strips covered in Al-foil were used to clamp the substrates

in place during coating. The temperature on the hotplate was measured with a K-type thermocouple (same as for synthesis temperature control), which was placed next to the substrates under the thin Al-plates, but the temperature was hard to control, because the temperature was lowered during spraying.

Typical inks were formulated from mixtures of 10% ethanol and 90% water. The ligand-free nanoparticle concentration was 20 mg/ml, and the mixture was sonicated for 2 h in an ice bath. For a typical deposition, a spray pressure of 3 mbar N_2 was used. The substrates were attached on a hotplate, and heated to a temperature of $130°C$ (set point temperature of $160°C$) before deposition was initialized. Spray-coating was carried out with a linear movement (right/left) over the samples for 5 s, and left to dry for 25 s. The total deposition time lasted 25 min. For the first 15 min, deposition was done with 10 cm distance to the substrate, after which the deposition rate was increased by lowering the distance to about 5 cm. Some parameters were hard to control with this hand-held spray gun, especially the spraying distance, angle and movement[2].

4.2.2.3 Drop-casting

Drop-casting was carried out by placing a drop of ink on a substrate with a pipette, and when necessary blow-drying the film with a flow of nitrogen. This technique was used for preparing samples for characterization and for optimizing the sulfurization procedure.

Inks were formulated by adding 5 ml toluene or ethanol to approx. 200 mg of ligand-coated or ligand-free nanoparticles, respectively, and sonicating for 30 min. Films were formed by dropping one drop on a 1 cm×1 cm substrate. The ligand-coated nanoparticle samples were left to dry for 30 min, while the ligand-free nanoparticle samples were blow-dried with a flow of nitrogen for 5 min to expedite the drying and create a more uniform layer. This process was repeated three times, whereafter the samples were heated at $150°C$ for 20 min.

4.2.3 Characterization

After deposition, the samples were characterized with optical microscopy. In some cases, micron-sized cracks and holes were discovered, and these films would be discarded for solar cell fabrication. After annealing, the cross-section of the films was imaged with SEM. In the below sections, a few initial examples are showed to point out what can affect film formation.

---

[2]An extra challenge originated from the fact that the coating was carried out inside a fume hood. The sash window should be kept down to minimize spreading of airborne particles into the lab, and in the meantime the spray gun should be vertically positioned above the samples at a typical distance of 5 to 15 cm.
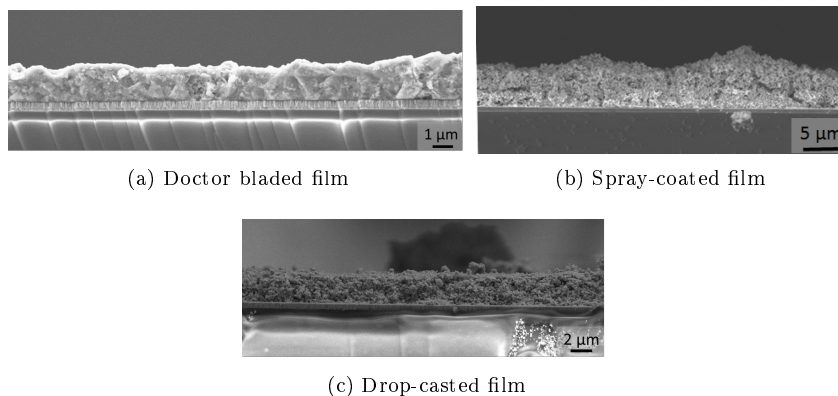
(a) Doctor bladed film

(b) Spray-coated film

(c) Drop-casted film

Figure 4.4: Thickness variations in doctor bladed, spray-coated, and drop-casted films.

4.3 Results and discussion

Thickness control and a uniform film formation without holes and large cracks are important characteristics for a good quality deposition. All films deposited were between 500 nm and 5 μm (up to 10 μm for spray-coated films), and SEM micrographs of typical annealed films are showed in Fig. 4.4. For the spray-coated film in Fig. 4.4(b), micrometer-variation in the thickness can be seen, which is a typical trait for this deposition method. While the thickness of the drop-casted films also varied but to a smaller extent (not clear in image), doctor blading was the easiest way to control the thickness.
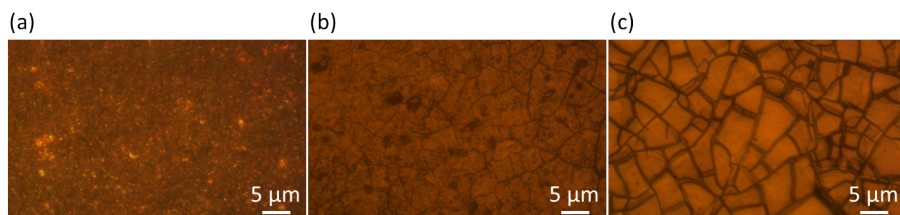

Figure 4.5: Optical micrographs of doctor bladed films at 40 times magnification, where (a) shows a crack-free surface, (b) cracks of less than 500 nm, and (c) more than 1 μm wide cracks.

4.3.1   Doctor blading

Three optical micrographs of doctor bladed samples are displayed in Fig. 4.5. They exemplify a crack-free sample (a), a sample with minor cracks[3] (b), and a sample with major cracks (c). The samples were prepared almost identically, but with few variations. Samples (a) and (b) were prepared from the same nanoparticles, but sample (a) was made first, followed by nanoparticle washing by centrifugation and re-dispersion to form the ink for sample (b). Sample (c) was made with a different batch of nanoparticles, and only 3/4 of the solvent volume was used compared to (a) and (b). Only a few studies were carried out, and not enough to conclude anything definitive about crack formation in these films; however one outcome is that the nanoparticles are sensitive to many different parameters and their history of treatment. Therefore it was necessary to monitor the formation of each individual film as a new one.
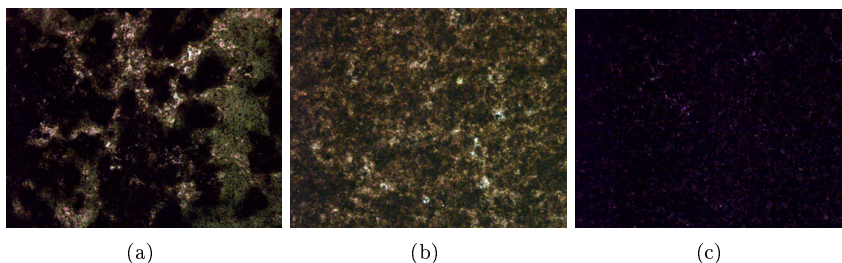

(a)   (b)   (c)

Figure 4.6: Optical micrographs of spray-coated nanoparticle films under 100 times magnification. (a) large islands and holes, (b) smaller holes, and (c) no holes detected with SEM. Unfortunately the scale bar cannot be determined.

4.3.2   Spray-coating

The formation of pin holes is one of the main issues encountered for spray-coated thin films. The particles tend to agglomerate instead of forming a smooth film. Spraying slowly and allowing the film to dry at low temperatures should give the particles less energy to move around and therefore a higher likelihood to form a uniform film. However, the spray-coated films are typically rough, because large droplets will dry on the substrate without first forming a coherent film [158].

It is also important to start with a completely homogeneous, well-dispersed ink. Fig. 4.6 shows optical micrographs of three different spray-coated films, with large holes in (a), smaller holes in (b), and no holes in (c). The difference in preparation is that (a) did not have a completely well-dispersed ink initially,

---

[3]Small cracks can under properly working annealing conditions grow together to form a uniform film, also seen by [160].

and the substrate temperature was kept at 100°C throughout the reaction. The temperature for samples (b) was increased from 130°C to 290°C, and for sample (c) from 130°C to 220°C. The total deposition times were 18 min, 45 min, and 25 min, respectively. Moving the spray gun closer to the substrate greatly increases the deposition rate. Sample thicknesses were: 0.3-1, 4-5, and 1-3 μm, respectively. The images are representative of the samples, but there were variations on each sample too.

A recent study by Martini *et al.* determined interesting fluid properties of CZTS inks for spray-coating and ink-jet printing. They identify four musts regarding ink formulation: (1) long-term nanoparticle stability in the ink to avoid clogging, (2) appropriate fluid properties for formation of a stable drop-generation, (3) good substrate wetting, and (4) suitable solvent evaporation rate to avoid the formation of cracks and pin holes [156]. The fluid properties that are required for a given liquid to be printable can be characterized by some physical constants, and a parameter, Z_{spray} is used here defined as

$$Z_{spray} = \frac{(\gamma_{ink}\rho a_{nozzle})^{1/2}}{\eta} \quad (4.1)$$

where ρ the ink density, a_{nozzle} the characteristic nozzle diameter, ηink the viscosity of the ink, and γ_{ink} the surface tension of the ink. A stable drop will be formed when $10 > Z_{spray} > 1$ [161].

Martini *et al.* determine good substrate wetting behavior when the difference between the surface tension of the substrate, γ_{sub}, and the surface tension of the liquid, γ_{liq}, was about 10 mJ/m^2. The surface tension of the Mo substrate was measured to be 48 mJ/m^2, which calls for a solvent with about 38 mJ/m^2 [156]. These properties can be used to tune the nanoparticle ink to improve the deposition.

4.3.3   Drop-casting

Drop-casting is an easy and fast method to make films with the ligand-free nanoparticles. The thickness can be controlled between 1 to 5 μm, which is enough for making samples for optimizing the sulfurization procedure. There are still many holes in the film, and the samples are not suitable for making solar cells.

4.4   Outlook

A presentation on the deposition techniques used has been given, with a description of the experimental setup, and the resulting film morphology. No

reproducibility studies have been carried out, and in true each film was studied as a novel one. Optical microscopy was a useful technique to determine whether or not there are cracks and holes, but these features can exist even though they are not observed here. For doctor bladed films, cracks could be observed in some cases, while for spray-coated films pin holes were more common. Depositing a thicker film by multi-layer deposition will limit these holes. Drop-casting is not known to be a very reproducible technique, and thus not recommended to make solar cells, but its ease of use and the rapid depositions made it useful for preparing samples to study the sulfurization conditions. In true, drop-casting can be made more reproducible by drop-casting a measured amount with a pipette into a frame clapsed on top of a substrate, as done by [162].

I believe that thin-film deposition is the main weakness of the present work done on CZTS solar cells. Especially for the ligand-free nanoparticles, spin-coating would make depositions more reproducible and faster than spray-coating, and more uniform with a better control of pin holes compared to drop-casting[4]. The addition of a small amount of binder might be helpful, but is perhaps not necessary as it will also add additional organic species to the film. More meticulous studies on the film thickness and surface roughness should also be carried out for different ink formulations, and by varying spin-coating parameters (rotational speed, time, and intermediate heating steps).

If spray-coating is a priority, an automated system will provide better control of the deposition conditions. High-efficiency solution-processed chalcogenide photovoltaic devices have been fabricated in a nitrogen glove box by spray-coating [35]. This group observed a huge increase in efficiency, when coating was performed in inert atmosphere instead of under ambient conditions. A nitrogen glove box would also allow easier control over the spraying distance. Furthermore, a better control can be achieved by connecting a thermocouple to LabView and monitoring the temperature during deposition. Characterizing the fluid properties of the ink used in terms of the Z_{spray} parameter, suitable substrate wetting and solvent evaporation rate would be useful and only a few measurements required. Finally, finding a way to determine the long-term nanoparticle stability in the ink would also be beneficial.

---

[4]DTU Fotonik has a spin-coater, but it has been and is still out of use due to renovations (written September 22, 2016).

SULFURIZATION OF SOLUTION-PROCESSED Cu_2ZnSnS_4 THIN FILMS

This chapter concerns sulfurization of CZTS nanoparticle and precursor thin films. The objective is to achieve a dense absorber with micron-sized grains. We found that the nanoparticle systems were very challenging to sinter, as a high temperature was not sufficient to start the sintering process. We solved this by eliminating the organic ligands that impeded the merging of the nanoparticles and by including a liquid phase additive during annealing to enhance grain growth.

5.1 INTRODUCTION

Micron-sized grains are desirable, because too many grain boundaries reduce the charge transport since the boundaries act as recombination centers for electrons and holes [163]. In addition, the best CZTS solar cells produced from nanoparticles have micron-sized grains [31, 146]. One exception is the work by Park *et al.* who fabricated a CZTS thin film from spin-coated precursors, and when annealed at 540°C an efficiency of 5.02% is achieved versus 0.15% when annealed at 570°C [34]. The grains are smaller for their best device, but this could be a result of other factors because the absorber is also very porous.

In this section, a presentation of grain growth theory and well-known methods that increases the rate of sintering will be given. Thereafter, the considerations for annealing the CZTS compound are summarized, with an overview of published CZTS nanoparticles solar cells. Finally, typical annealing studies on solution-processed CZTS are presented.

5.1.1 Theory of grain growth

The high melting point of CZTS of 990°C makes it impossible to deposit as a liquid phase directly on the desired substrate. Instead, a particle or precursor ink must be used for deposition, which is converted into a solid under a subsequent heat treatment. The process of merging nanoparticles without melting into a solid material is called *sintering* and/or *coarsening*, and is commonly used for ceramics or metal particles. However, the principles apply to any crystalline or amorphous material, and can also be used to explain our colloidal CZTS system [162].
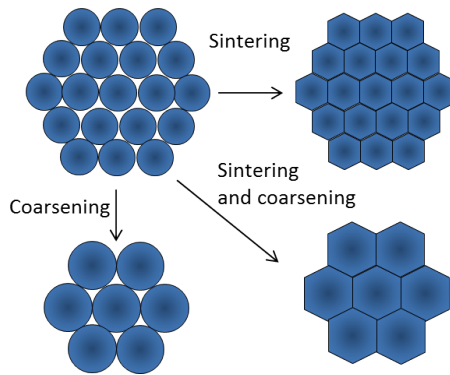
Figure 5.1: Simplified schematics of result of sintering and coarsening processes, where the sintering process displayed also results in a higher density. Sintering takes place when vacancies migrate out of the sample to decrease the surface area, *i.e.* material diffuses to fill out a void thus decreasing the center-to-center distance of particles and causing densification. Coarsening is a process similar to Ostwald ripening, where smaller particle will dissolve and larger ones grow (imagine that the displayed particles are not of exactly the same size). Coarsening results in larger average grain size and also larger average pore size.

Grain growth, just like nanoparticle growth, occurs when a system evolves to minimize its surface energy. The rate depends on temperature and the initial particle size. Grain growth can occur either by sintering or coarsening (Fig. 5.1). During sintering, individual particles are combined to a bulk with solid interfaces, and the density of the material can increase or remain the same. Whether or not the density of the material increases, depends on the diffusion mechanism. If material either is moved by grain boundary diffusion from the neck to the surface or lattice diffusion from the neck to the surface, the density will increase. Coarsening can occur either by coalescence, where two particles merge, or Ostwald ripening, where smaller particles dissolve and larger ones grow.

As described in [164, 165], the purpose of grain growth studies is often to determine the required temperature, applied pressure, particle size and packing,

composition and type of atmosphere in order to produce the desired microstructure. Understanding which physical properties that make sintering happen is crucial since it allows control of the final density and thus avoid porosity.
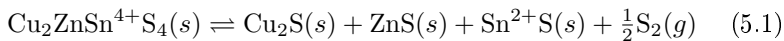
5.1.1.1 INCREASING THE RATE OF DENSIFICATION

Enhanced densification rates can be obtained in three different ways: dopant-assisted sintering, hot-pressing, or liquid phase additive sintering. *Dopant-addition* can reduce the grain boundary mobility, which makes it more likely that pores will remain attached to the grain boundary. When pores are attached to the grain boundary, it is more likely that they are completely eliminated, and result in a higher density. *Hot-pressing* is carried out by applying an external pressure, which increases the driving force for densification. *Liquid phase sintering* includes a small amount of a liquid that partly fills the voids in the material and assists in the densification. The (simplified) mechanism is typically divided into several (overlapping) steps: As temperature is increased (1) the liquid phase is formed, and (2) distributed around the solid phase, (3) the solid phase will be dissolved in the liquid and reprecipitate which causes densification [164, 165]. When considering which liquid phase additive to use, there are certain guidelines, including a good solubility for the principle constituents, and a reasonably low viscosity for rapid diffusion [164].

5.1.2 GRAIN GROWTH IN THE CZTS COMPOUND

The typically used sulfurization temperature of CZTS is in the range between $500°$C and $600°$C [59]. Similar to liquid phase synthesis, where Cu-S formation is followed by Cu-Sn-S and finally Zn-inclusion to form CZTS [108], the solid phase formation goes through similar steps for films made from precursors. At room temperature, only metal binaries exist, and when the temperature is raised to above $200°$C, metal-chalcogenide binaries start to form. Above $450°$C, Sn will be included into a Cu-Sn-S phase, and above $500°$C ZnS reacts with Cu_2SnS_3 to form CZTS [166]. In addition to these solid state chemical reactions, the elevated temperature is needed to remove defects and grow grains [59].

Increasing the time and temperature will produce larger grains. However, this has to be balanced with elemental losses that are commonly seen during annealing of the CZTS compound. The decomposition reaction of CZTS which is dominating at high temperature states that

$$Cu_2ZnSn^{4+}S_4(s) \rightleftharpoons Cu_2S(s) + ZnS(s) + Sn^{2+}S(s) + \tfrac{1}{2}S_2(g) \quad (5.1)$$
$$SnS(s) \rightleftharpoons SnS(g) \quad (5.2)$$

Scragg *et al.* found that it is the multivalent instability of Sn which is the driving force of the elemental losses in CZTS [136]. They calculated the minimum partial pressure of sulfur, $p_{\mathrm{S_2}}$, to ensure CZTS stability at 550°C to be greater than 2.3×10^{-4} mbar, and the partial pressure product, $p_{\mathrm{SnS}}(p_{\mathrm{S_2}})^{1/2}$, to be greater than 3.8×10^{-5} mbar. One way to keep the decomposition at bay is to supply sufficient vapor pressure of the elements on the right side of the chemical equilibrium in Eq. (5.1). This is done by introducing gaseous S or SnS, and by annealing in a closed volume. For instance, Redinger *et al.* found that adding S and Sn during annealing was crucial for their absorber, and increased the efficiency from 0.02% to 5.4% for their co-evaporated CZTSSe precursors [167]. As an example of our own work, the first CZTS absorber which was annealed without any additional sulfur or tin was found to decompose into a wide range of secondary and ternary phases (Fig. 5.2).
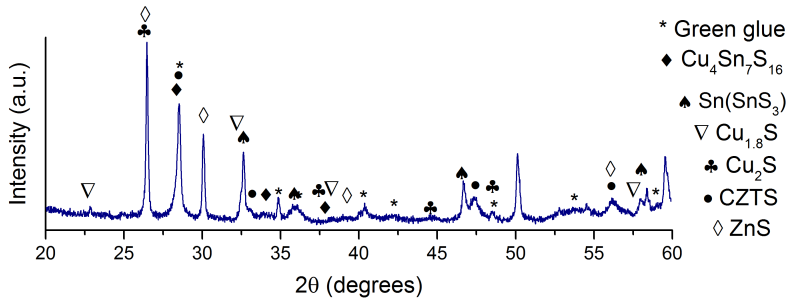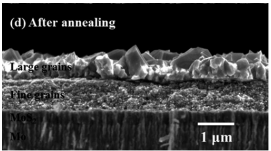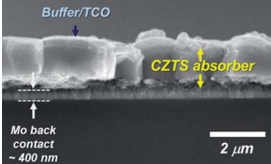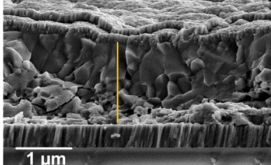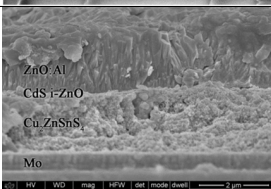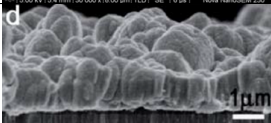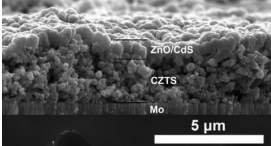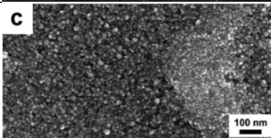

Figure 5.2: XRD pattern with matching phases for ligand-coated CZTS thin film on quartz annealed at 550°C for 30 min with no additional sulfur in the graphite box. This was one of the first annealings carried out. Several secondary phases are detected, and it is clear why S-powder is required in the box to avoid decomposing the CZTS phase. Once sulfur had been introduced in the graphite box, the CZTS phase did not decompose, and no difference was seen when varying the S-amount (which must mean that the S is adsorbed in the graphite structure). The green glue was used to keep the sample in place.

5.1.3   STATE OF THE ART

The number of published pure-sulfide CZTS nanoparticle solar cells is from the author's knowledge limited to seven cases. Annealing in Se will increase the efficiency [42], but as discussed earlier there are reasons for avoiding Se and improving the pure-sulfide devices. An overview of the fabricated solar cells are displayed in Table 5.1, including synthesis, deposition and annealing approaches. The SEM micrographs of the two record devices (perhaps also the 2.5% device) are the only samples that exhibit micron-sized grains, while the micrographs of other devices were not of high enough resolution to see any grain boundaries. The images are displayed in a larger size in Appendix D. One common factor for the two record devices is that Na is added to the nanoparticle thin film, but

Table 5.1: Overview of all pure-sulfide CZTS nanoparticle solar cells. The crystallite size is determined by XRD. New abbreviations: Dodecanethiol (DDT), dimethylformamide (DMF), dichlorobenzene (DCB), and polyvinylpyrrolidone (PVP). "C.S." denotes crystallite size, and "P.S." particles size.

SEM image	Synthesis	Deposition	Annealing	η
	One-pot, TOPO/DDT, 1h/250°C, for wurtzite CZTS.	Spin-coating in DMF, air-anneal 5min/250°C, repeated several times. 25 nm NaF (sputtering).	S, 5 min/580°C	4.8% [31]
	Hot-injection, TPP, 300°C P.S.: 14.5±4.6 nm	Spin-coating in DCB, air-anneal 10 min/350°C, soaked in Na-solution, dried 10 min/80°C, 1.4μm thick	N_2+4%H_2S, 30 min/500°C	3.6% [146]
	One-pot, OLA, 2h/260°C P.S.: 60 nm C.S.: 20 nm	Spin-coating, air-anneal 5 min/150°C, many layers, 1 μm thick	Air, 1h/350°C C.S.: 60 nm	2.5% [29]
	Hot-injection, OLA P.S.: 12 nm	Doctor blading, hexanethiol, 200 mg/ml, air-anneal 2 min/300°C, two layers, 1.5 μm thick	S/Ar flow, 30min/550°C C.S.: 24 nm	2.0% [28]
	Solvothermal, EG+PVP, 180°C/12h P.S.: 10 nm	R2R printing, EtOH/H_2O, 1-2 μm thick	S, 20 min/500°C	1.94% [30]
	One-pot microwave, EG P.S.: 7.6 nm C.S.: 7.3 nm	Spin-coating, 50 mg/ml, air-anneal at 80°C, 19 layers, 3 μm thick	SnS+S powder/N_2 flow, 20 min/400°C Thickness after: 2.4 μm C.S.: 26.8 nm	0.25% [97]
	One-pot, OLA P.S.: 10.6 nm	Spray-coating, toluene, 20 mg/ml	No annealing	0.23% [26]

they also differ in other ways: One utilizes wurtzite nanoparticles that transform into the kesterite phase during annealing, and the other one utilizes a type of easily decomposable capping ligands (triphenylphosphate, TPP). The deposition technique that results in the highest efficiencies is spin-coating, but doctor blading, R2R printing and spray-coating have also been attempted. Annealing takes place above 500°C in atmospheres branching from pure S, to diluted H_2S, to air.

5.1.4 Annealing condition for solution-processed CZTS films

Numerous optimization studies have been carried out to determine the influence of the annealing conditions on solution-processed CZTS absorber layers, however not on annealing of nanoparticle thin films. Furthermore, most annealing setups and starting materials are different. Previous findings can be used as a guideline, especially when there is an agreement in the literature.

Annealing can be performed either in inert or reactive atmosphere, where the reactive chalcogen-containing atmosphere can compensate for deficit in the absorber by increasing the S-amount. It is important to avoid having less than the stoichiometric amount of sulfur, since sulfur vacancies have a low formation energy and will create deep level donor defects in the absorber [47]. If the as-deposited film lacks sulfur, annealing in sulfur will lead to a volume expansion of the crystal lattice, and a more dense film with larger grains [168]. Finally, as mentioned before, a high vapor pressure of sulfur will prevent the decomposition reaction of CZTS. Sulfurization can be done with elemental sulfur in inert atmosphere [31, 162, 160], in forming gas (for evaporated CZTS) [167], or hydrogen sulfide [146, 169, 170, 171, 172], in increasing order of reactivity and toxicity. In one comparative study, more uniform and densely packed grains are seen for annealing in hydrogen sulfide [172].

To further enhance grain growth in nanoparticle thin films, several innovative means have been pursued. Limiting the amount of organic material by utilizing shorter ligands [160], more easily decomposable ligands [146], or using ligand-free nanoparticles dispersed in ethanol/water (synthesized by the solvothermal method) [30]. Precursors can be added to the ink to serve as nucleation centers as demonstrated for CIS [173], or solution-filling where precursors are added after CIS nanoparticle films were deposited and dried [174]. Finally, employing the phase transformation from wurtzite to kesterite resulted in the record CZTS nanoparticles device [31]. Interestingly, one study by Zhang *et al.* shows that annealing ligand-free wurtzite CZTS nanoparticles does not result in significant grain growth [175]. The annealing conditions used for their study were 5% H_2S in N_2 atmosphere[1] for 30 min at 550°C. Perhaps it is not the phase transformation

---

[1] No note on pressure.

from wurtzite to kesterite which is sole reason for the success by Liu *et al.*, but rather the NaF-top layer employed [31]. Na-addition is in fact one way to enhance grain growth in the chalcogenide films, as will be discussed in the next section.

5.1.4.1 INCREASING THE RATE OF DENSIFICATION IN CZTS

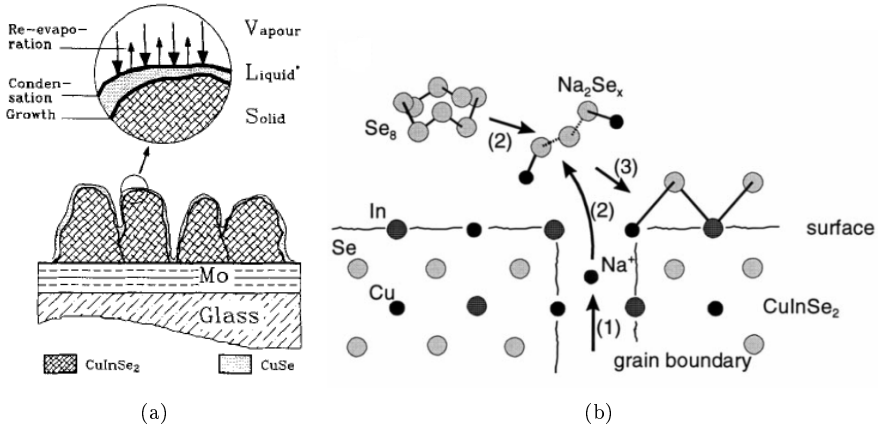(a)   (b)

Figure 5.3: Grain growth models for CIS, where (a) is the liquid phase CuSe sintering model by Klenk *et al.* from [176], and (b) liquid phase Na_2Se_x sintering model by Braunger *et al.*, from [177].

The Cu-content has an influence on the structural evolution of the film, where Cu-rich conditions display larger CZTSSe grains than the desired Cu-poor composition [178]. Indubitably, this excess of Cu would result in a $Cu_{2-x}S(e)$ secondary phase, which was also detected. Nevertheless, KCN etching can be employed to remove unwanted Cu-phases [19]. For the selenide systems, Cu-rich conditions are believed to improve grain growth by forming a liquid phase CuSe-additive [176, 179, 180]. For the sulfides, CuS is not a liquid phase at temperatures below 600°C, which would limit the usefulness of the Cu-rich conditions for grain growth in CZTS. However, due to the high cation mobility in the Cu-S compound this could still result in a quasi-liquid phase on the surface of the grains [181].

The liquid phase CuSe assisted model for $CuInSe_2$ materials by Klenk *et al.* explains that grains grow by a vapor-liquid-solid (VLS) mechanism (Fig. 5.3(a)). They explain that the Cu-atoms will diffuse to the surface, and furthermore that: "*The vapor species condense at the surface of the binary phase covering the grains. They are then transported to the binary/ternary interface where the crystallite is growing,*" [176]. Other liquid binary phases could form, but CuSe was experimentally found to be the important one.

The incorporation of alkali metals in solution-processed CZTS thin films has been done through a selection of different processes. The most studied additive is sodium, which has shown massive improvements on CZTS both in terms of grain growth and electronic properties. DFT calculations have also showed that Na is expected to increase the conductivity and raise the efficiency of CZTS devices [182].

Sodium can be included by soaking the film in sodium salt [146], or by depositing a NaF-layer on top of the absorber layer before annealing, for example for wurtzite CZTS nanoparticles [31], and at different thicknesses for precursor solutions (CZTSSe) [183, 184]. Vacuum deposition of a NaF-layer is relatively complicated and expensive. In addition, for both Na-soaking and NaF-deposition, the beneficial effects of Na is typically restricted to the proximity of the NaF-layer, and limited by the Na-diffusion within the film [185]. To obtain a more uniform distribution of Na, surface functionalization of the nanoparticle ligands with Sb [145], or Na (in the form of CF$_3$COONa) of different concentrations (0.5% to 10% Na/(Cu+Zn+Sn)) [185], has been done. All the above examples add an extra process step to the fabrication. Therefore, Na can also be included directly in the ink, either during synthesis of nanoparticles through the hydrothermal approach with Na$_2$S as the S-precursor [30, 95], or through the precursor approach with Na$_2$S [35], or 0.2% NaCl [32]. Moreover, Li-addition in a precursor ink with LiCl and LiF has produced the highest hydrazine-free CZTSSe efficiency [186]. Sol-gel synthesized films with 0.5%, 1% and 5% (Na/(Cu+Zn+Sn)) (NaOH) have also been studied [187].

The commonly accepted explanation for why Na is aiding grain growth is the so-called *liquid Na$_2$Se$_x$ mediated route*, which was first developed by Braunger *et al.* and showed in Fig. 5.3(b). Here, cracking of Se$_8$ molecules into Se$_y$, $1 < y < 8$, is followed by reaction with a Na$^+$ ion at a grain boundary to create reactive liquid Na$_2$Se$_x$. This material has a higher sticking coefficient to the chalcogenide crystal surface than gasous Se$_y$, so after sticking they will crystallize with metallic precursors at the grain boundary to form the chalcogenide. Due to the resemblance between the Na-S and Na-Se phase diagrams, we assume a similar mechanism can explain the increased grain growth in the pure-phase CZTS system [188, 189]. The reactive sulfide phase would now consist of Na$_2$S$_x$.

5.2   Experimental details

Sulfurization is performed in a home-made vacuum oven with the possibility to choose the background gas and pressure. The parameters that can be controlled in our setup include:

- Temperature and heating ramps
- Time

- Initial background pressure
- Atmosphere (N_2 or 5% H_2 in N_2)

Parameters that cannot be directly controlled or measured are:

- Sulfur and tin sulfide vapor pressure
- Cooling rate

After annealing, there will be residual sulfur and tin sulfide inside the graphite box. The oven has one hot zone and one cold zone, and sulfur solidifies on the cold zone and therefore it must be lost from the graphite box. How long time the provided sulfur stays in the graphite box is not known.
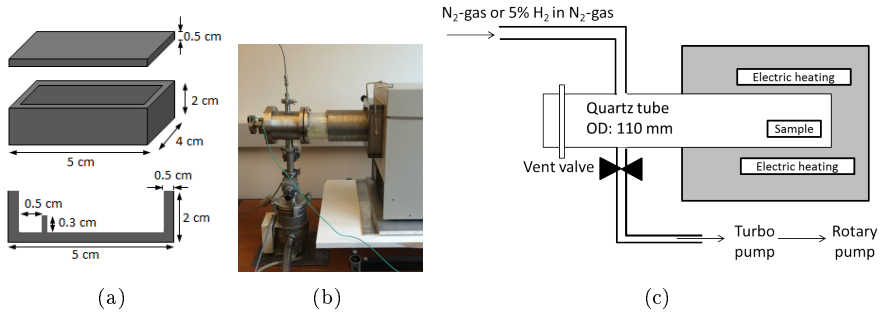
5.2.1   Oven design

Figure 5.4: Sulfurization oven, including (a) graphite box schematics, (b) image of oven, and (c) schematics of oven. The dimensions of the quartz tube are: Length 50 cm, outer diameter 110 mm, and glass thickness 3 mm.

The sulfurization oven setup is depicted in Fig. 5.4. The temperature and pressure were monitored during each annealing with a thermocouple positioned either inside a hole in the graphite box, next to the graphite box, or outside the quartz tube. The limitations on the temperature is that above 600°C SLG deteriorates[2] [170]. Furthermore, the oven has some mechanical limitation, where the temperature of O-rings cannot exceed 200°C. The O-rings are located towards the cold zone in the quartz tube, where the quartz tube is connected to the metal flange. The graphite box is showed in Fig. 5.4(a), and sometimes a lid with a 1 mm hole in was used. S powder (99.98%) and SnS powder (99.99%) were purchased from Sigma Aldrich, and always put in the small compartment in the graphite box when used.
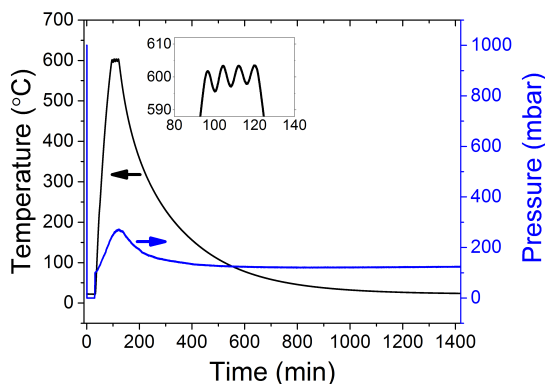
Figure 5.5: Annealing profile of temperature and pressure during a typical annealing at 600°C for 30 min. The temperature oscillates between 596°C and 603°C as showed in the inset.

5.2.2   Experimental procedure

In a typical annealing, 100 mg of S powder was added to the graphite box, which also contained unquantifiable amounts of residual S from previous annealings[3]. The oven was pumped down to a base pressure below 10^{-2} mbar, filled with 100 mbar N$_2$, and heated to 600°C in 45 min. The temperature was kept at this step for 30 min, followed by a natural cooling where it took 10 h to reach 50°C. This is displayed in the annealing profile in Fig. 5.5. The temperature at 600°C will in fact oscillate between 596°C and 603°C, as can be seen in the inset. The pressure in the quartz tube increases from gas expansion according to the ideal gas law, and to a less extent from evaporation of S. The pressure specified in the discussion below is the initial pressure prior to heating[4].

5.2.2.1   Oven cleaning

The oven was cleaned by scraping off sulfur with paper towels from inside the quartz tube every eight to tenth annealing, followed by a bake out, where the oven filled with N$_2$ was heated to 600°C and pumped. The graphite box was also left inside the oven. There was no way to test the effect of this cleaning, but less sulfur remained on the inside of the quartz tube.

---

[2]It is possible to anneal at 800°C, as done by Chernomordik *et al.*, however the SLG might be damaged after this [162].

[3]The graphite box would also contain Cu, Zn, Sn, and S from previous annealings, and especially SnS powder after SnS was introduced.

[4]The actual pressure during annealing will depend on the temperature.

5.2.3 CHARACTERIZATION

One new characterization technique used here was glow-discharge optical emission spectroscopy (GDOES). GDOES measures compositional depth profiles in solid samples. This is done by sputtering material off the sample, and detecting emission from atoms accommodated in plasma. A Horiba Scientific Profiler2 was used, which was operated in RF-mode at powers of 25 W with a patented ultra fast sputtering (UFS) technology using a gas mixture of Ar and 5% O_2 at a pressure of 300 Pa.

5.3 RESULTS AND DISCUSSION

The results from the annealing studies are split up into three parts: the ligand-coated nanoparticle films in Section 5.3.1, films made from a precursor ink and deposited with spray-coating in Section 5.3.2, and the ligand-free nanoparticle films in Section 5.3.3. This is also in chronological order according to when the work was conducted.

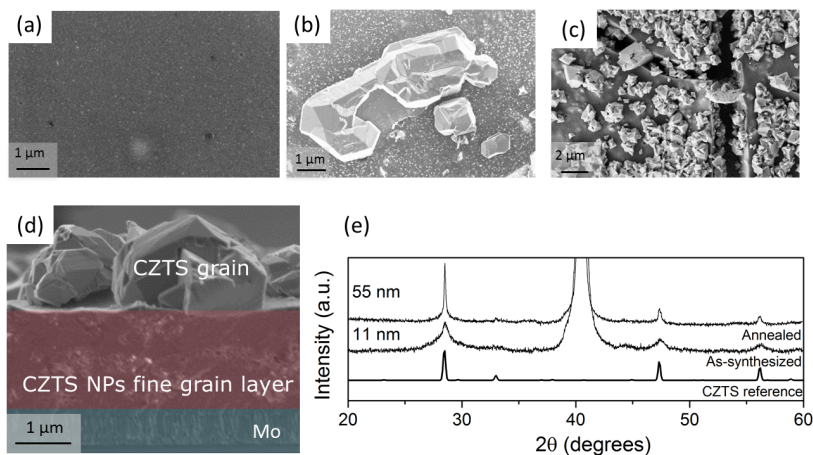### 5.3.1 LIGAND-COATED CZTS NANOPARTICLE THIN FILMS

Figure 5.6: Display of typical ligand-coated CZTS nanoparticle films deposited via doctor blading. (a)-(c) show top view SEM micrographs of an as-deposited (a) and two annealed films (b)-(c). (d) shows a cross-section, where it is clear that the large grains grow on top of the film. (e) shows the XRD patterns of an as-deposited and annealed film, where the peaks sharpen after annealing. SEM micrographs taken by Andrea Crovetto.

In this section a summary of the results on annealing ligand-coated CZTS nanoparticle thin films is presented. The nanoparticles used for this analysis

were the ones synthesized by the one-pot method described in Section 2.3.2, with severe reproducibility or EDX measurement issues.

Three parameters were preliminary investigated: (1) the amount of sulfur required for annealing (0 mg, 20 mg, 50 mg, 100 mg, and 200 mg), (2) the sulfurization time (30 min, 1 h, and 2 h), (3) the background pressure used for annealing (see Appendix E for all SEM micrographs and selected XRD patterns and compositions). No significant difference was detected under the selected annealing conditions, except for the XRD pattern of the first annealing with 0 mg S in the graphite box (Fig. 5.2), which showed decomposition of the CZTS phase. An overview of a typical appearance of these films is displayed in Fig. 5.6. As a general observation, grains grow on the surface of the films. The composition of the large grains (Cu/(Zn+Sn)=0.82, Zn/Sn=1.32) versus the composition of the average film (Cu/(Zn+Sn)=0.65, Zn/Sn=2.0) suggests that the large grains on top of the surface are CZTS. There was no trace of grain growth within the films (Fig. 5.6(d)), but a high amount of organic material was detected here. The grain growth on the surface of the film and the presence of the fine grain layer are consistent with what other groups find when annealing ligand-coated nanoparticles (sometimes to a lesser extent than us) [31, 146, 162, 160].

The XRD patterns in Fig. 5.6(e) do not show any secondary phases, and the peak sharpens during annealing. The crystallite size as calculated by the Scherrer equation goes from 11 nm to 55 nm after annealing at 550°C for 30 min, which agrees with with grain growth occurring.

The curious appearance of CZTSe grains on top of the film has been explained in terms of out-diffusion of cations to the top surface [190]. Mainz *et al.* saw that the layer under the large grains contained a higher concentration of carbon than the bottom of the film [190]. They proposed that the carbon covering the particles restricts them from merging, either by reducing the surface energy of the particles (which in turn reduces the driving force for sintering) or in another way create an energy barrier for growth, and thus making cation out-diffusion to the surface the only possibility to form large grains [160].

The underlying formation mechanism is thus connected to (lack of) decomposition of organic material at the surface. Tiong *et al.* study the grain growth of CZTS nanoparticles in different solvents with 3 to 10 carbon atoms per molecule [160]. They find that when solvents with three carbon atoms were used, a bi-layer with a dense but thin top layer of grains up to 3 µm in diameter were formed. When the carbon content in the solvent molecule is 5 or 7 atoms, the micron-sized grains penetrate deeper in the absorber but at the expense of a higher porosity. When the number of carbon atoms in the solvent was increased to 10, grain growth was further restricted and did not cover the full top surface (similar to our absorbers in Fig. 5.6(b) and (c), which were made with a 8 carbon atoms solvent).

The organic ligands and solvent residues can (I) evaporate, (II) thermally decompose, or (III) react with sulfur. Chernomordik *et al.* suggest the formation of CS_2, COS, and H_2S, when annealing ligand-coated CZTS nanoparticle thin films in a quartz ampule for a better control of the sulfur pressure [162]. This assessment was based upon eye inspection of the color of the evolved gases, the faint sulfurous odor when the sample is removed from the quartz ampule, and from elemental analysis of the leftover powder, which was mostly carbon with trace amounts of sulfur.

These species (m/z 76 (we see some 44), 60, and 34, for CS_2, COS, and H_2S, respectively) were not detected with mass spectrometry, but admittedly there was no added sulfur powder during these studies. Based on the results in **Paper III**, the oleylamine ligands will thermally decompose into smaller fragments such as CH_2NH_2, $C_3H_6^+$, and $C_2H_3^+$ starting at $350°C$ and peaking at $470°C$[5]. Increasing the annealing time and temperature to 2 h at $800°C$ as done by [162] did not result in a complete removal of the organic material, suggesting even more energy is required.
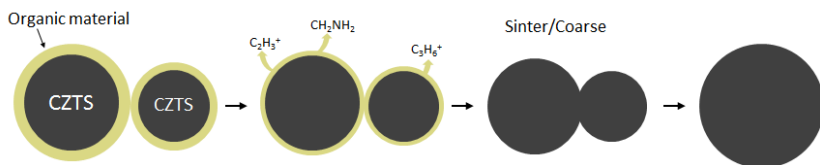

Figure 5.7: Grain growth model by removal of organic material based on our results, and inspired by Tiong *et al.* [160]. The presence of too much organic material will prevent the merging of the nanoparticle, but as the oleylamine ligands thermally decompose into smaller species, grain growth will finally occur.

The explanation by Tiong *et al.* for why the grains are growing on the surface is also based upon that sulfur is participating in a reaction with carbon to remove the organic material. For removal of carbon within the film, sulfur vapor would first have to diffuse into the bulk. Once a compact CZTS top-layer is formed, this will further hinder the diffusion of sulfur to the fine grain layer underneath [160].

Based on the results in **Paper III**, we cannot say that removal of organic material is connected to the sulfur vapor[6], since we did not add any sulfur and we still saw grains growing on top of the film. Therefore, our hypothesis is that thermal decomposition of the organic materials is part of the formation mechanism, and that the organic species that will have to diffuse to the surface to be removed. Particles will merge to minimize the surface energy, however

---

[5]I cannot explain why thermal decomposition appears to stop above this temperature. Is it too hard for the organic material within the film to diffuse to the surface? Should we include an isothermal annealing step at $470°C$?

[6]There is of course a possibility that sulfur evaporates from the CZTS.

this requires that the particles are in contact, which is not the case when an organic coating exists[7]. Based on our results, we present an adjustment of grain growth model originally made by Tiong *et al.* (Fig. 5.7).

(a)   (b)
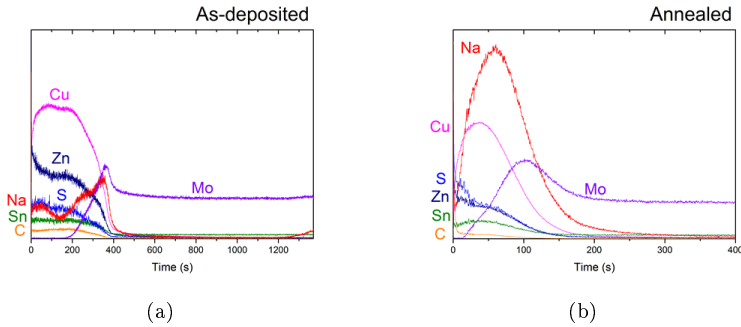
Figure 5.8: GDOES measurements of an (a) as-deposited and (b) annealed film. The cation amounts do not change in relation to one another, however the Na-amount is clearly increasing after annealing. This points to out-diffusion of Na from the substrate. GDOES measurements taken by Patrick Chapon.

The preliminary GDOES measurements in Fig. 5.8 suggest out-diffusion of Na during annealing. The measurements were not calibrated and cannot be used for quantification. What can be deduced is the relative concentrations of each element. While the Cu-, Zn-, and Sn-amounts do not seem to change during annealing, the Na-amount increases to a great extent. The very low presence of Na in the Mo-layer is also observed in similar measurements [184]. Na-diffusion from the SLG is commonly seen and known to improve grain growth [191, 192], however the out-diffusion of Na from the SLG was not enough to enhance grain growth in these nanoparticle films.

5.3.1.1   SUMMARY

The ligand-coated nanoparticle thin films presented here, did not work well as solar cell absorber (see Chapter 6). Presently, grains nucleate and grow at the film-vapor interface, and micron-sized grains are required connecting the back Mo-contact with the top surface. Focus should be put upon minimizing the amount of organic material, and optimizing the annealing conditions further. The presented changes with respect to the sulfurization time, the added sulfur amount, and the pressure, have not been sufficient to merge the nanoparticles into larger grains. Uniform grain growth have been observed by other group, and therefore it should be achievable.

---

[7]The length of the oleylamine molecule is approximately 2 nm.

Limiting the amount of organic material in the films can be done by increased washing of the nanoparticles or by using less binder used during deposition. However, as we expected this difficulty at an early stage, the ligand-free nanoparticles were developed. In a few sections you will see that adding a rather high concentration of Na, can lead to successful sintering of the nanoparticles.

5.3.2 Precursor Cu-Zn-Sn-S thin films

The precursor inks should, according to recent record efficiencies of solution-processed CZTS, be an easier starting point than CZTS nanoparticles. Therefore, it seemed like the best method to understand and optimize the spray-coating approach and also a promising method to make absorber layers. Accordingly, the first time grain growth was detected within the depth of a film, was for a thin film deposited from a precursor ink with spray-coating (Fig. 5.9).
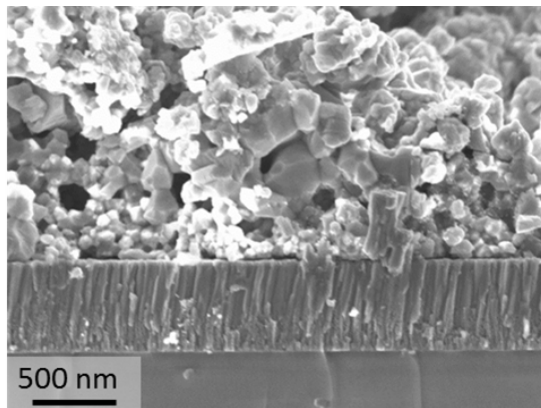

Figure 5.9: SEM micrograph of spray-coated film made from precursors. This was the first time grain growth was detected within the film. This is samples M1, annealed at 550°C for 20 min. Images taken by Andrea Crovetto.

A typical ink was formulated by preparing three mixtures: 0.8 mmol $CuCl_2 \cdot 2H_2O$ was dissolved in 10 ml DI water, 0.67 mmol $ZnCl_2$ and 0.42 $SnCl_2 \cdot 2H_2O$ in 10 ml DI water, and 380 mg thioures in 20 ml DI water in a third flask. The three mixtures were stirred for 10 min, whereafter 2 drops of HCl was added to the Zn and Sn solution. The mixtures were combined, and the ink was used for spray-coating as described in Chapter 4. Annealing was carried out at 550°C.

As an overview of the work, three inks with different salt concentrations are listed in Table 5.2. None of them have the desired composition as measured by EDX, but the XRD patterns of all annealed samples were satisfactory (Fig. 5.10(a)). The Raman spectrum of sample M3 displays sharp CZTS peaks (compare the $286\,\mathrm{cm}^{-1}$ peak) (Fig. 5.10(a)), and sample M3 could be Zn-poor CZTS. Samples

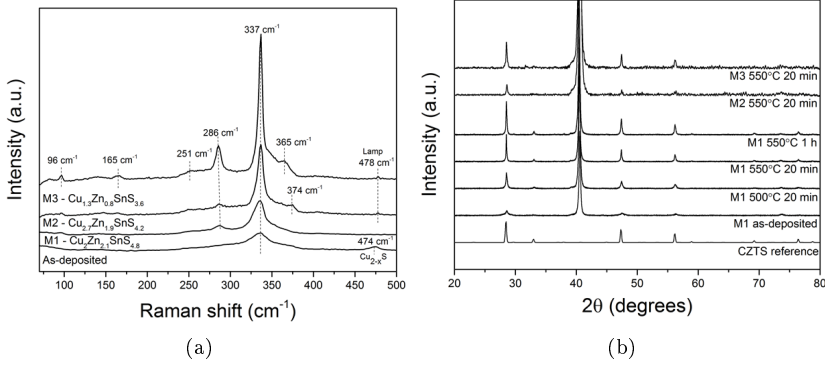(a)   (b)

Figure 5.10: Characterization of samples M1, M2, and M3 prepared by spray-coating a precursor ink. Raman spectra (a) of annealed samples with increasing CZTS signal, and XRD patterns (b) for different annealing procedures. Perhaps there is a XRD peak at $31.8°$ for sample M3, but due to the noise level it is difficult to say.

Table 5.2: Effect of varying metal salt on elemental composition after annealing. The composition is presented as if the synthesized phase is CZTS, but in fact it could be a combination of binary and ternary phases as well.

Sample	CuCl₂· 2H₂O (mmol)	ZnCl₂ (mmol)	SnCl₂· 2H₂O (mmol)	Composition
M1	0.8	0.67	0.42	$Cu_2Zn_{2.1}SnS_{4.8}$
M2	0.8	0.54	0.57	$Cu_{2.7}Zn_2SnS_{4.3}$
M3	0.8	0.54	0.74	$Cu_{1.3}Zn_{0.8}SnS_{3.6}$

M1 and M2, on the other hand, are Zn-rich and could very well contain a ZnS secondary phase, which cannot be detected with XRD or Raman spectroscopy with the laser wavelength of the setup used.

5.3.2.1 SUMMARY

The results in this section are preliminary, and they should here serve as an introduction to what can be done without nanoparticles. By tuning the concentration of the metal salts in the ink, a better composition can be obtained. However, it was the deposition technique used here, spray-coating, which made it challenging to achieve reproducible films. Since promising results were obtained from the ligand-free nanoparticles (see below), the precursors route was not pursued further.

5.3.3 LIGAND-FREE CZTS NANOPARTICLE THIN FILMS

The sulfurization oven and the conditions applied are crucial for making a good absorber layer[8]. Therefore, reproducible films with the same composition were needed in order to optimize the annealing conditions. This was obtained by drop-casting the ligand-free nanoparticles with very similar composition (most films were made from only two different batches). This allowed examination of the effect of added sulfur-amount and SnS-amount in the graphite box, background pressure, sulfurization time and temperature, atmosphere, and finally a liquid phase additive. The results are collected in **Paper IV**. In the following, an overview of the paper and some additional results are presented.

5.3.3.1 SUMMARY OF FINDINGS IN PAPER

The effect of Na in Cu_2ZnSnS_4 nanoparticle thin films has been investigated. The as-synthesized CZTS nanoparticles were inherently ligand-free (**Paper II**), which allowed the use of polar solvents, such as water and ethanol. Another advantage of these particles is that the user- and environmentally-friendly NaCl salt can be directly dissolved in controllable amounts. This further circumvents the need for later incorporation of additives, or a ligand-exchange step to functionalize the surface of the nanoparticles. In addition, the homogeneous distribution of Na in the ink allows uniform grain growth within the deposited absorber layer.

By including Na in the nanoparticle ink, micron-sized grains throughout the whole absorber are achieved after annealing in a sulfur atmosphere at 600°C. The absorber layer appeared to be of a density corresponding to full density, and no closed porosity could be detected. In addition, the photoluminescence signal increased by a factor of 200 after Na-inclusion. Without Na, the grains were very difficult to sinter, the film was porous, and the photoluminescence was low. The Na-concentration was defined as the Na/(Cu+Zn+Sn)-ratio of the measured Cu, Zn, and Sn atomic percentages and the added Na, and we see that concentrations between 10% and 40% produced a dense absorber with micron-sized grains. These concentrations are significantly higher than those used in other CZTS systems with sodium.

We also found that a sulfidation temperature above 550°C was required. At 550°C, NaCl-crystals appeared on the surface of the thin films, suggesting an incomplete transformation of Na into the liquid phase Na_2S_x-additive during

---

[8]We realized this after my colleagues sent a PLD absorber to another lab for annealing and device fabrication. The efficiency increased from 2.7% to 5.2%! We suspect that the sulfurization was the main difference, as the other layers appeared similar or even better when fabricated in our lab.

sintering. At this temperature, grain growth was only detected in close proximity to the NaCl regions. It was also observed that the NaCl crystals could be easily removed by a quick water rinse, but that this treatment reduced the photoluminescence signal (Chapter 6). This is relevant as it is customary to leave the absorber layer in a water-based solution after annealing before buffer layer deposition.
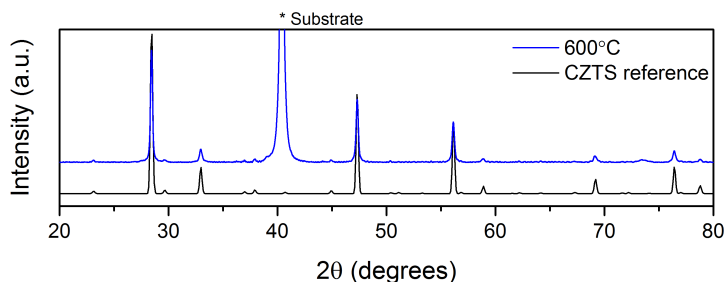

Figure 5.11: A 4 h XRD scan will reveal the small peaks that do not exist in ZnS or Cu₂SnS₃. Adopted from **Paper IV**.

5.3.3.2 Annealing without Na

In the supporting information of **Paper IV**, you will find a meticulous study on CZTS films without Na of all annealing conditions that could be changed in our setup: The amount of sulfur between 0 mg and 200 mg, background pressure from 25 mbar to 225 mbar, the temperature between 400°C and 600°C, SnS addition, annealing atmosphere, and annealing time between 0 min and 2.5 h. The composition, SEM morphology, XRD patterns, Raman spectra, and PL spectra were quite similar for the different conditions. However, a few of these results are good examples of typical or atypical phenomena that occur in CZTS and our nanoparticle system, and will be discussed here accordingly.

First of all, the sample annealed at 600°C was the only one where a change in morphology was seen, however the sample was still very porous. An extraordinarily accurate XRD scan of this sample did reveal all the small reflections that do not exist in ZnS and Cu₂SnS₃ (Fig. 5.11). These phases might still exist, but considering the relative peak intensities, most of the material must be CZTS.

Secondly, one may expect S- and Sn-loss especially for the material annealed at 600°C, but this was not detected even though no additional SnS-powder

Table 5.3:   Composition of selected samples from annealing optimization study. Atomic ratios are averages of five different measurements, and errors are standard deviations calculated from five measurements. Reprinted from **Paper IV**.

Sample	Cu (at.%)	Zn (at.%)	Sn (at.%)	S (at.%)
As-synthesized	25 ± 0.3	14 ± 0.4	14 ± 0.5	47 ± 0.2
600°C 0 min	25 ± 0.7	14 ± 0.7	13 ± 0.7	48 ± 1.0
600°C 30 min	25 ± 1.0	14 ± 0.4	14 ± 0.4	47 ± 1.3
600°C 2.5 h	23 ± 0.5	13 ± 0.3	13 ± 0.3	51 ± 0.9
400°C	22 ± 0.8	12 ± 0.4	15 ± 0.8	51 ± 1.1
500°C	23 ± 1.1	13 ± 0.9	13 ± 0.6	51 ± 1.9
Hole in lid	21 ± 0.6	14 ± 0.7	12 ± 1.1	53 ± 1.4

was used (Table 5.3). We therefore assume the partial pressure in the graphite box of $S(g)$ and $SnS(g)$ is sufficiently high in order to avoid elemental losses. SnS powder has been foreseen as an indispensable addition [136], but it did not directly help in our annealing, and no groups that made a solar cell from nanoparticles claimed or disclosed using it[9] [31, 146]. Thus, the decomposition reaction in Eq. (5.1) could be less pronounced for annealing nanoparticle thin films.

The samples that had the largest deviations from the original composition were the samples annealed at 400°C, 500°C, and the sample annealed with a hole in the graphite box. A decrease in the Cu-amount was seen for all samples, and possibly a loss of Sn for the sample annealed with a hole in the lid, but it is difficult to draw any conclusion when the S-amount also increases and the errors of the measurements are quite substantial. The Raman spectra that differed most from the rest were those at 400°C and 500°C, and Fig. 5.12 shows that Cu-Sn-S phases are present below 550°C. The existence of these phases corresponds well to what is expected to form in these temperature regimes [166]. The XRD pattern of the sample annealed at 400°C (see Supporting Information of **Paper IV**) may have a $Cu_{1.8}S$ phase, but the Cu-Sn-S phases detected with Raman spectroscopy will overlap with the CZTS peaks.

5.3.3.3   Mixing nanoparticles and precursors

As an additional attempt to enhance grain growth in the ligand-free nanoparticle films, precursors were added as nucleation centres. Films were made from a mixture of spray-coated nanoparticles and precursors. Fig. 5.13 displays SEM micrographs of three types of spray-coated samples: Precursors, nanoparticles, and a mixture of 50% precursors and 50% nanoparticles. These films were

---

[9]Flynn *et al.* used it to fabricate a solar cell with an efficiency of 0.25%, which is similar to an non-annealed device [97, 26].
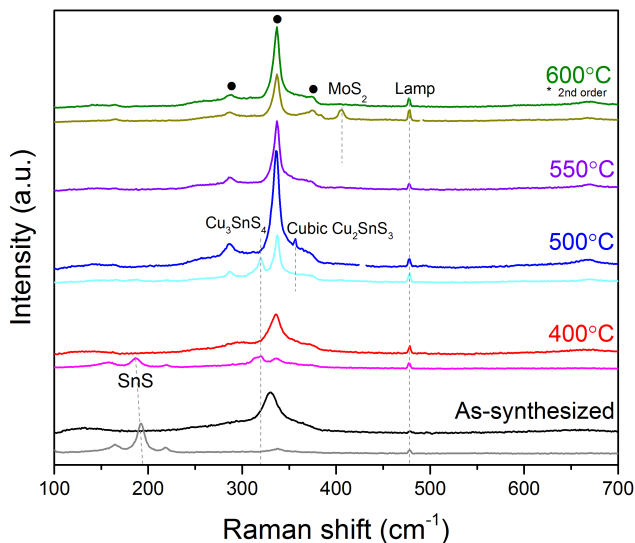
Figure 5.12: Phase evolution for CZTS nanoparticle thin film annealed at different temperatures. The main CZTS peak around 337 cm^{-1} was present in all samples, and other CZTS peaks are marked with a ● . The as-synthesized particles contain a SnS-phase, which still exists at 400°C. At 400°C and 500°C Cu-Sn-S phases were also seen. At 600°C, a MoS_2 phase is present, however this has to do with the thickness of the sample. Raman spectra taken by Stela Canulescu. Figure is adapted from **Paper IV**.

annealed at 550°C for 30 min in forming gas. The thickness can be sufficiently controlled to around 2 μm, but many holes exist, in particular for the films made from precursors. No micron-sized grains are seen, and the films are very porous. The largest agglomerates appear for the precursor films, and the smallest for the nanoparticle films. Whether the agglomerate consists of grains cannot be concluded, but under all circumstances they are smaller than a few hundreds of nanometer. Furthermore, the precursor and 50%/50% as-deposited films appear smooth, but after annealing the porosity increases because of solvent evaporation. Films of a very similar morphology from spray-deposited CIGS have been fabricated by Ahn *et al.* [180].

The sample composition was determined to be $Cu_{1.5}Zn_{1.1}SnS_?$, $Cu_{1.4}ZnSnS_?$, and $Cu_{1.7}Zn_{0.9}SnS_?$, for precursors, 50%/50%, and nanoparticles, respectively[10]. No secondary phases could be detected from the XRD patterns with this resolution (Fig. 5.14(a)). The Raman spectra only show the CZTS peaks, except
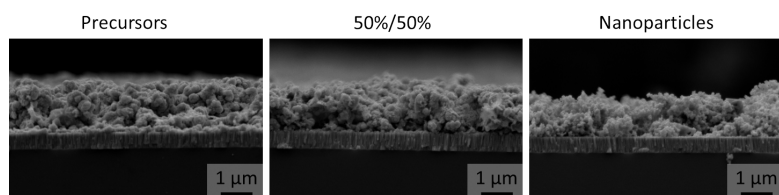
---

[10]The sulfur amount could not be quantified because it overlapped with the Mo-signal.

Precursors 50%/50% Nanoparticles

(a) As-deposited top views

Precursors 50%/50% Nanoparticles
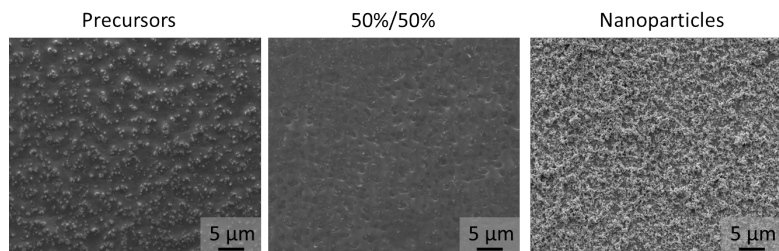
(b) Annealed top views
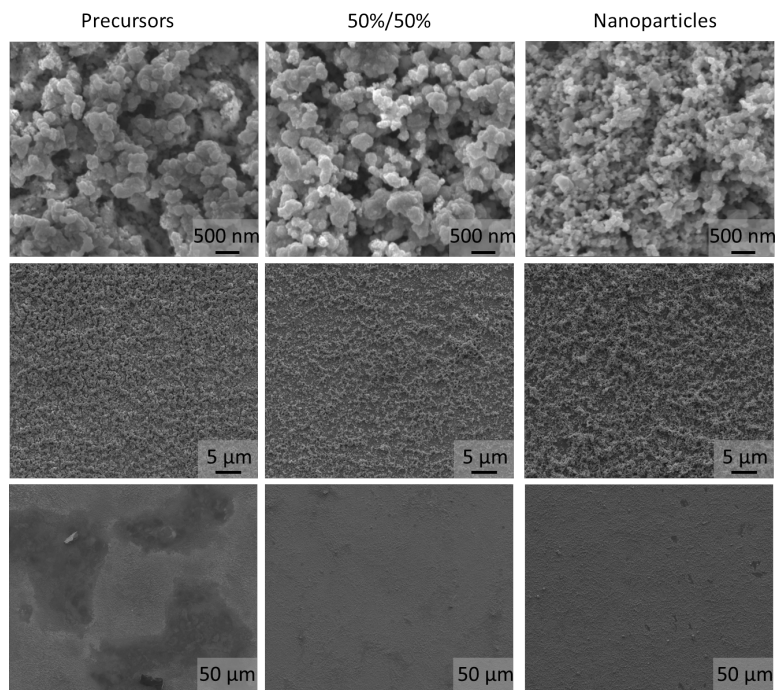
Precursors 50%/50% Nanoparticles

(c) Annealed cross-sections

Figure 5.13: Spray-coated samples, where (a) are the top views of as-deposited samples, (b) the top views of the annealed films under different magnifications, and (c) the cross-sections of annealed samples with a thickness around 2 µm. Films were annealed at 550°C for 30 min in forming gas.
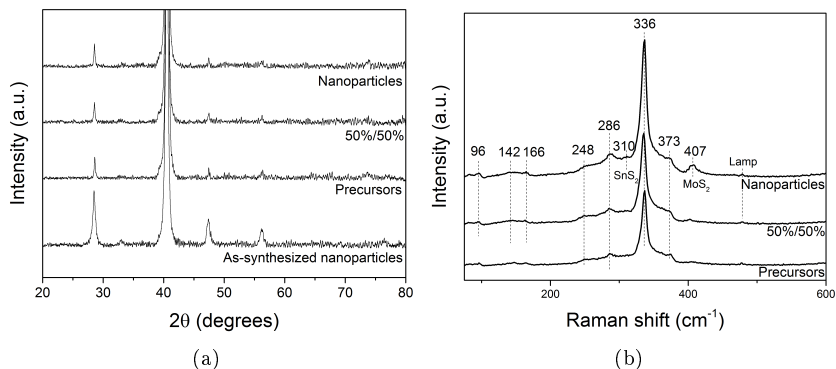
Figure 5.14: XRD patterns (a) and Raman spectra (b) of three types of spray-coated films. The XRD patterns appear similar, and as do the Raman spectra. Raman spectra taken by Stela Canulescu.

for the nanoparticle sample where a substrate peak (MoS$_2$) was also detected, and possibly a SnS$_2$ peak (Fig. 5.14(b)). This study exemplifies the difficulty in seeing grain growth in these solution-processed CZTS thin films.

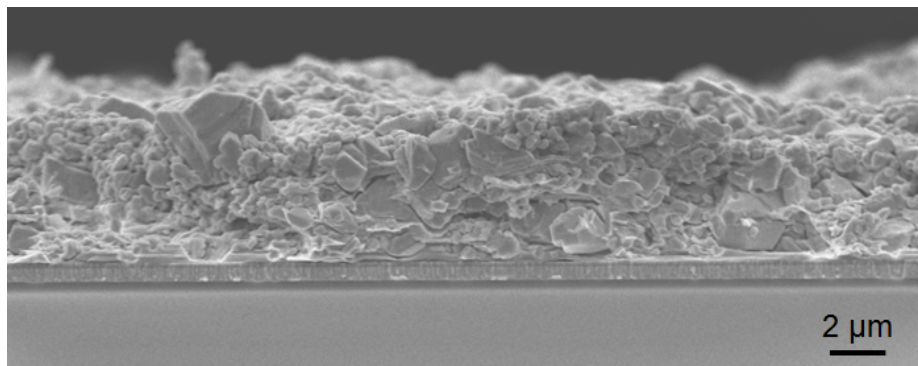#### 5.3.3.4   The effect of Na-addition

Figure 5.15: Dense CZTS layer with micron-sized grains. The thickness should be decreased to make a device. A 200 nm thick MoS$_2$-layer is detected at the substrate.

For the thin films in this work, a concentration of 10% Na or higher was used to induce a change in film morphology. A cross-section of a sample with 40% Na annealed at 600°C is displayed in Fig. 5.15, where dense, large grains can be seen. In addition, a 200 nm thick MoS$_2$ layer could be identified as part of the Mo-layer. The high Na-concentrations in themselves were not sufficient to sinter
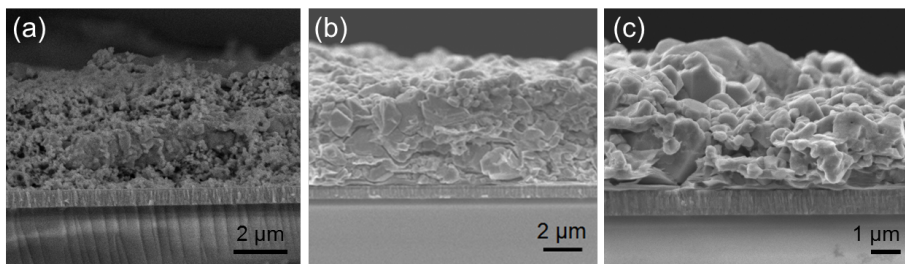
Figure 5.16: Comparison of (a) 30% Na annealed at 550°C, (b) 40% Na annealed at 600°C, and (c) 40% Na annealed at 600°C with a subsequent water rinse. Some grain growth in the sample annealed at 550°C is detected, however it is very porous and it could possibly be NaCl. Once Na is added and the temperature is raised to 600°C, micron-sized grains appear throughout the whole absorber layer, and the film looks similar after water rinse.
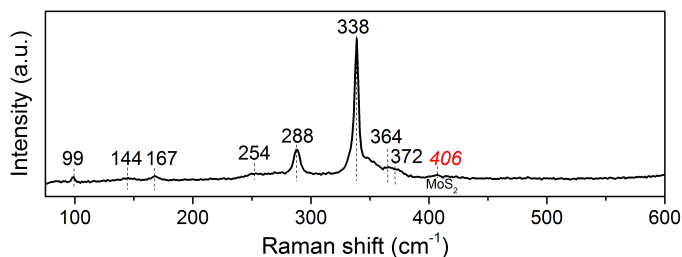

Figure 5.17: Raman spectra of annealed CZTS at 600°C with 40% Na, with no sign of any secondary phases except from MoS_2. Raman measurement by Stela Canulescu.

the particles, but additionally a temperature of above 550°C was required, as the cross-section micrograph in Fig. 5.16(a) shows. This has been seen before, for example by Tian *et al.* who used Na_2S as sulfur precursor when synthesizing CZTS nanoparticles by the hydrothermal route, but as they only anneal at 500°C, no significant grain growth was achieved in their system [30]. For some of the films annealed at 550°C, NaCl-crystals were detected by XRD and elemental mapping on the surface of the CZTS films. These would be detrimental to a solar cell, however they can easily be removed with a quick water rinse. The cross-section after such a treatment is showed in Fig. 5.16(c).

The Raman spectrum of a 40% Na sample in Fig. 5.17 shows many of the characteristic peaks for CZTS, with no signs of any secondary phases. However, with Raman spectroscopy it can be difficult to distinguish CZTS from ZnS with the laser wavelength used here. Furthermore, Sn-S has been detected at the CZTS film/Mo-substrate interface by doing Raman spectroscopy on exfoliated

films (**Paper IV**). The presence of a SnS_2 phase at the back contact would probably be detrimental to the solar cell, as it is an n-type semiconductor with a band gap of 2.2 eV.

Sulfurization of the back contact to a layer of MoS_2 has only been detected from cross-sections of samples annealed with Na. The formation of MoS_2 indicates a high reactivity of S during annealing, as S can diffuse deeply into the absorber [193]. Accordingly, Tiong *et al.* also notice the formation of a thin (50 nm) MoS_2 for C-rich solvents, and thick (350 nm) MoS_2 layers for solvents with less carbon [160]. The existence of reactive sulfur is good, because it means that grains will grow, however the formation of MoS_2 may not be beneficial. MoS_2 is an indirect semiconductor with a band gap of 1.3 eV that may affect the V_{OC} and alter the band-alignment at the CZTS/Mo-interface to restrict hole transport [49].

Table 5.4: Composition of samples with 10% Na. The atomic ratio is the averages of five different measurements, and errors are standard deviations calculated from these five measurements.

Sample	Cu (at.%)	Zn (at.%)	Sn (at.%)	S (at.%)
N1 (as-synthesized)	24±0.9	16±0.6	13±0.6	48±0.9
N1 30 min	24±1.6	13±0.8	12±2.7	51±4.8
N1 1 h	23±1.0	13±2.4	12±0.8	52±2.6
N1 2 h	-	-	-	-
N2 (as-synthesized)	23±0.6	18±0.5	12±0.5	47±0.9
N2 30 min	19±1.6	15±2.8	10±1.5	56±5.4
N2 1 h	22±0.6	18±1.7	11±0.3	50±1.4
N2 2 h	22±0.7	17±0.4	10±1.0	51±1.2

5.3.3.5 The effect of sulfurization time with Na-addition

As an additional example of how Na-addition enhances grain growth, two nanoparticle batches with different composition were annealed with 10% Na for different annealing times. The compositions are listed in Table 5.4 and SEM micrographs of top surfaces are shown in Fig. 5.18. Apparently, the sulfurization time is not very important for the degree of grain growth, but rather the Na-concentration. For these films, a concentration of 10% is not sufficient to create a completely dense layer.

5.4 Outlook

Annealing CZTS nanoparticle thin films in sulfur atmosphere can be discouraging. Basic improvements such as increased sulfurization time and temperature,
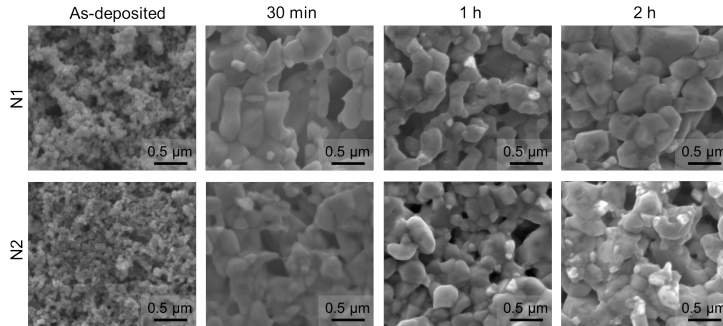
Figure 5.18: SEM micrographs as a function of time for two different compositions (N1: $Cu_{1.8}Zn_{1.2}SnS_{3.7}$, N2: $Cu_{1.9}Zn_{1.5}SnS_{3.9}$. Annealing is carried out at 600°C with 10% Na, and no added SnS powder.

minimized C-content, or changing the atmosphere to forming gas only led to relatively small changes in film morphology. High porosity, small grains within the film, or grains only growing on the surface of the films were some typical features of these nanoparticle films. The addition of Na in the form of NaCl salt aided grain growth throughout the thin film and produced a dense absorber layer. For even higher concentrations of NaCl in the inks, methanol or water could be used to form the ink, as NaCl is more soluble in these solvents. To better understand the mechanism of Na-assisted grain growth, annealing studies on films with Na at different temperature should be carried out. Furthermore, it might be possible to carry out Monte Carlo simulation studies to learn more about the grain growth mechanism in these films.

One critical point about Na-addition is that it requires such a high annealing temperature (600°C), as liquid phase Na_2S_x has to be created. I think that the next step should be to investigate other liquid phase additives. I would say there are five criteria that need to be fulfilled: (1) the molecule should contain sulfur, (2) it should become liquid at a lower temperature than Na_2S_x, (3) it has to work as a liquid phase additive and enhance sintering, (4) it should also improve the electronic properties of CZTS, and (5) it should of course be relatively cheap and non-toxic. My first-hand suggestions would be K_2S_x, Rb_2S_x, and Cs_2S_x which for high atomic percentages of sulfur would be a liquid at a lower temperature than Na_2S_x as seen from their individual phase diagrams (Fig. 5.19 and 5.20) [188, 194, 195, 196]. Among these, potassium has proven advantageous for solution-processed CZTS [197]. I would also encourage computational material scientists to calculate which of these dopants that would be useful for the electronic and photovoltaic properties of CZTS.

To further enhance grain growth in the film, a few approaches could be attempted: Adding precursors to the Na-included films annealed at 600°C, or hot

pressing the films during annealing (perhaps simply under a weight). Further-more, for the spray-coated films, hot pressing or vacuum pressing after deposi-tion could help create a more flat film.

The oven itself can also be improved, which would result in more reproducible and perhaps better results. Firstly, finding a way to control or measure the S (and perhaps SnS) vapor pressure during annealing would be helpful. The oven is built in such a way that it has one hot zone and one cold zone. We see that S sublimes on the cold zone, which means it is lost from the graphite box at some point. Therefore, building an oven that has no cold zone would allow a static environment with more S vapor. Some groups achieve this by annealing their samples in sealed quartz tubes, however this is not a fast and easy approach. Some groups also use hydrogen sulfide, which could be an option (especially now we already installed a H_2S sensor), but maybe not for up-scaling at a later stage. Secondly, control of the cooling would be useful. It could allow more than one annealing per day[11], and some secondary phases are more favourably formed at lower temperature regimes. It could also allow control of the order/disordering of the cations in the lattice. Many groups have a rapid thermal processing (RTP) oven, which can heat and cool very quickly. Finally, adjustments of the graphite box could be made by increasing the wall thickness or with a tighter construction (*e.g.* by screwing the lid on) to ensure a more stable atmosphere of S vapor and SnS vapor. Furthermore, coating the graphite box with SiO_2 could also do the same.

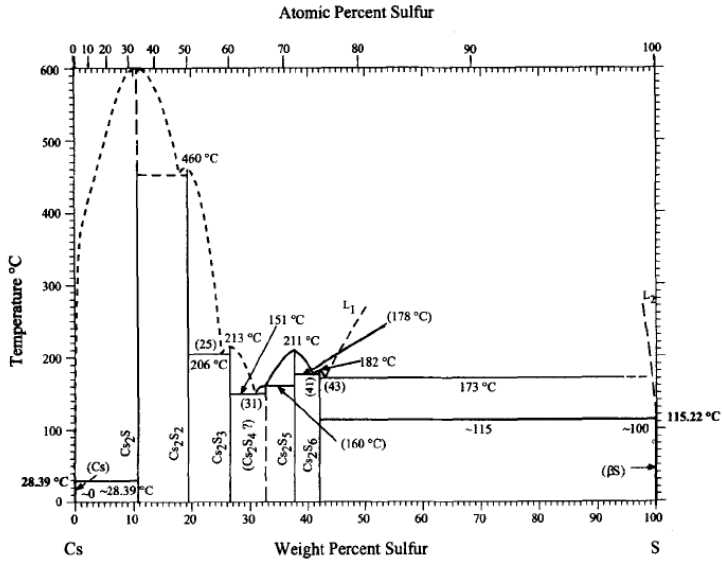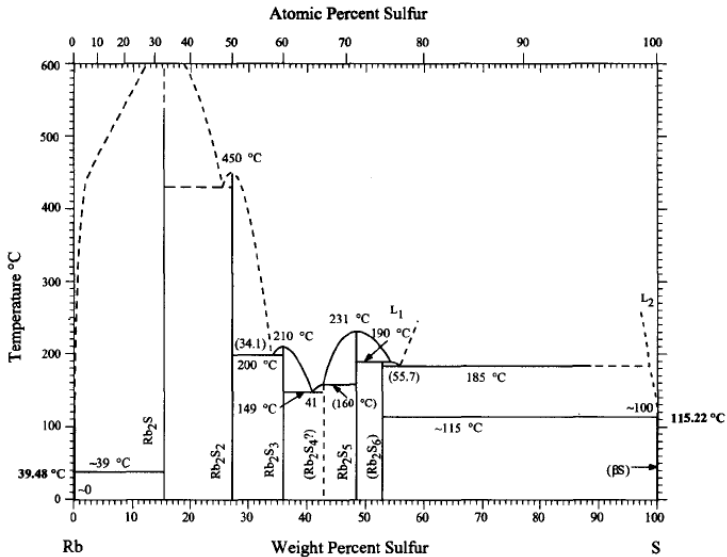[11]We were four people using the oven for sulfurization.
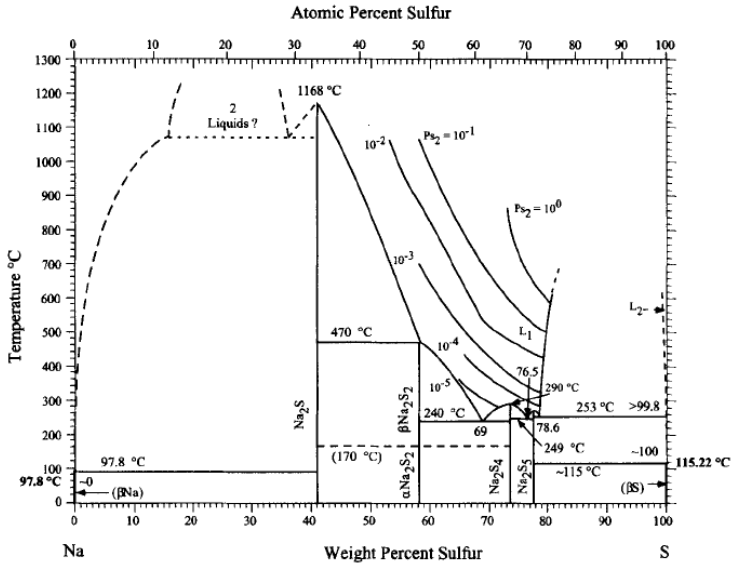
(a)
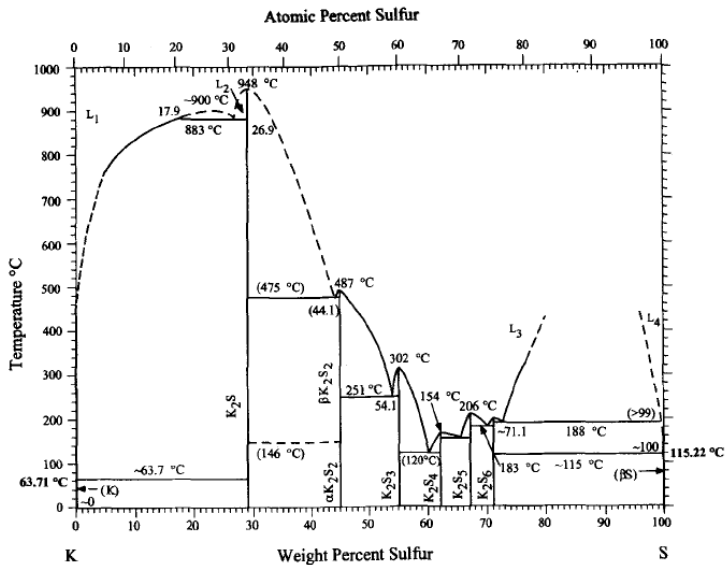
(b)

Figure 5.19: Phase diagrams of the (a) Na-S system, and (b) K-S system, from [188, 194].

(a)

(b)

Figure 5.20: Phase diagrams of the (a) Cs-S system, and (b) Rb-S system, from [196, 195].

PHOTOVOLTAIC BEHAVIOUR OF SOLUTION-PROCESSED CU$_2$ZNSNS$_4$ THIN-FILM DEVICES

In this chapter, a few CZTS thin-film solar cells will be briefly presented. I want to emphasize that focus has not been on manufacturing devices, as thin-film deposition still needs to be optimized. However, here are some baseline measurements that can be improved in the future. A useful measure to determine the quality of the bare absorber layers is photoluminescence (PL). We found that the annealed ligand-free CZTS nanoparticle thin films exhibited a high PL signal when sodium was included, which indicates that radiative recombination is dominating, and thus fewer defect states exist.

6.1 INTRODUCTION

In the following, the most important equations governing the behavior of a solar cell will be presented. The total current density, J, that in an ideal case can be extracted from a solar cell can be described by the light-generated current density, J_L, minus the diode current, such that

$$J = J_L - J_0 \left(e^{qV_A/kT} - 1 \right) \tag{6.1}$$

where J_0 is the saturation current density, q the charge on an electron, V_A the diode applied voltage, k the Boltzmann's constant, and T the temperature

[198]. A solar cell is typically characterized by parameters such as the open-circuit voltage, V_{OC}, the short-circuit current density, J_{SC}, the fill factor, F_F, the series resistance, R_s, and the shunt resistance, R_{sh}, which are all parameters that can be determined from the JV-curve.

The power conversion efficiency, η, can be found as the fraction between the maximum power output, P_m, and the incident power, P_{in} [199], as

$$\eta = \frac{P_m}{P_{in}} = \frac{V_m J_m}{P_{in}} = \frac{V_{OC} J_{SC} F_F}{P_{in}} \tag{6.2}$$

where V_m and J_m are the maximum voltage and current density, respectively, created in the solar cell.

6.2   EXPERIMENTAL DETAILS

All samples were annealed with 100 mg S, at 10 mbar N_2 pressure, 550°C for 1 h. The conventional device structure for CZTS solar cells consists of: Mo as the back contact, CZTS as the p-type absorber, CdS as the n-type buffer layer with a band gap of 2.4-2.6 eV, ZnO window layer, Al-doped ZnO (AZO) as the transparent conductor, and Ag or Al dot contacts on the top surface. For the detailed fabrication process, see [200].

6.2.1   CHARACTERIZATION

The current density-voltage (JV) characteristics were determined under simulated sunlight (AM 1.5G, 100 mW/cm^2) and measured with a Keithley 2400 Source Meter. The setup was calibrated with a standard crystalline silicon solar cell by Newport.

The external quantum efficiency (EQE) is a measure of how many incoming photons that are converted into electrons in the external circuit. The EQE was measured using a home-made setup at DTU Nanotech. Light from a halogen lamp was monochromated and focused onto a 0.5 mm diameter spot on the solar cell. The output current was measured in 10 nm wavelength steps at zero voltage bias and calibrated with a standard Si photodiode to yield the quantum efficiency of the device.

In photoluminescence spectroscopy a semiconductor is excited by illumination from a laser/lamp, and carriers emitted by radiative recombination are collected with a detector. Steady-state photoluminescence spectra were measured with an Accent RPM2000 system at an excitation wavelength of 532 nm and power density 100 W/cm^2.

6.3 Results and discussion

In the first part of the results, the best devices fabricated to date will be presented, and the second part will display the PL spectra of ligand-free CZTS nanoparticle films. As a final remark, a device annealed in selenium atmosphere is showed for comparison.

6.3.1 Performance of CZTS solar cells without Na

The current-density versus voltage characteristics of the best solution-processed CZTS solar cells fabricated are showed in Fig. 6.1(a). The best device was made from ligand-coated nanoparticles, and it had an efficiency of 0.2%. Important device characteristics are compared to the precedent literature in Table 6.1, where all our parameters are lagging behind the record device by Liu *et al.* [31].
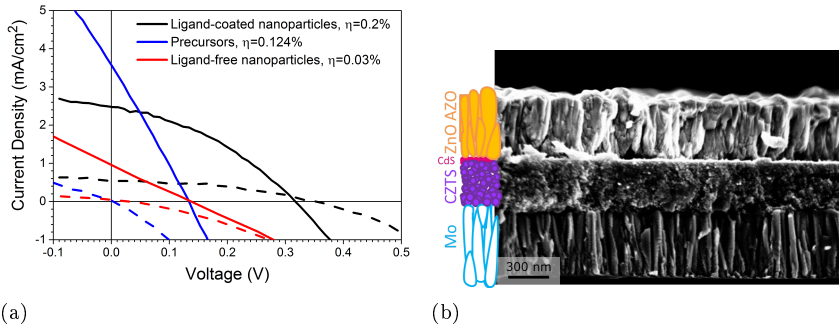

(a)   (b)

Figure 6.1: Photovoltaic performance (a) of solar cells made with different approaches but all with the typical bi-layer structure. The dashed lines are the measurements done in the dark. SEM micrograph (b) of a ligand-coated CZTS nanoparticle solar cell with an efficiency of 0.1%. Measurements and image acquired by Andrea Crovetto.

Table 6.1: Characteristic performance parameters for CZTS solar cells from three different inks. All samples were annealed at 550°C for 30 min and without any Na.

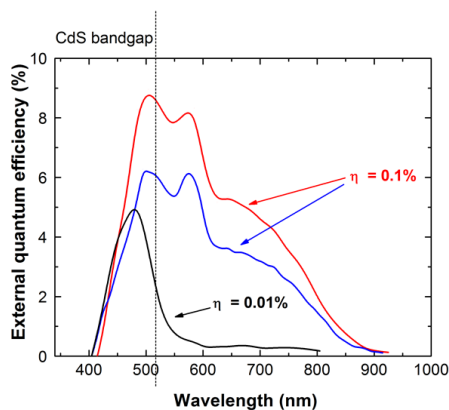|	Ligand-coated	Precursors	Ligand-free	Liu *et al.* [31]
η (%)	0.2	0.12	0.03	4.8
V_{OC} (mV)	315	135	139	525
J_{sc} (mA/cm^2)	2.5	3.6	0.95	17
F_F (%)	37	20		53
Area (cm^2)	0.2	0.14	0.17	
R_s (under illumination) (Ωcm^2)	34	19	65	
R_{sh} (under illumination) (Ωcm^2)	303	44	135	

Figure 6.2: External quantum efficiency spectral response of ligand-coated CZTS nanoparticle solar cells. Measurement done by Andrea Crovetto.

The maximum theoretical power conversion efficiency for a material with a band gap of around 1.5 eV is 32% for a single-junction solar cell [201]. The low efficiency of the fabricated devices is a consequence of overall low V_{OC}, J_{SC}, and F_F. Among these, the V_{OC} is a measure of the difference between the conduction band in CdS and the valence band in CZTS under flat-band/open circuit conditions (or the difference between the quasi-Fermi levels under short-circuit conditions). It will be limited from tail states in the band gap, and thus by bulk recombination or interface recombination.

The J_{SC} will depend on optical properties of the material, *e.g.* absorption and reflection, and on the collection probability. The absorption and reflection should be similar, such that low collection must be the cause for the low J_{SC}. The carrier collection is proportional to the generation of carriers (which is similar when the thickness does not change), and correlated to the diffusion length of electrons and holes. The ligand-coated nanoparticle device displays "crossover" between the light and dark JV-curves, which means that the device is dominated by recombination currents.

The F_F will also depend on a few different features. A high series resistance in all devices, but especially in the one made from ligand-free nanoparticles, implies poor charge transport through the material. The high series resistance could come from the CZTS absorber, but it could also originate at the top contacts. The low shunt resistance implies that shunt paths exist in the solar cell. Especially the JV-curve of the precursor cell is very steep near J_{SC}, *i.e.* it has a low shunt resistance, but it is also seen for the ligand-free nanopaticle device [60].

A SEM micrograph of a solar cell fabricated with ligand-coated nanoparticles

is showed in Fig. 6.1(b). It had an efficiency of 0.1%. The CZTS film is 400 nm thick, and no distinct grains were seen either on the surface or within the film, which could explain the high series resistance in similar devices and a low electron lifetime within the CZTS.

The external quantum efficiency will also provide information of the J_{SC}. Fig. 6.2 displays a low quantum efficiency of less than 10% for the solar cell with an efficiency of 0.1%. Furthermore, the EQE maxima at around 500 nm and 600 nm indicates that photons absorbed with these energies (2-2.5 eV) are the greatest contributor to the photo-current. However, the peak in the EQE could also stem from defect in CdS that are occupied at lower wavelengths. Therefore, some groups do the measurement under white light or under bias [202, 200].
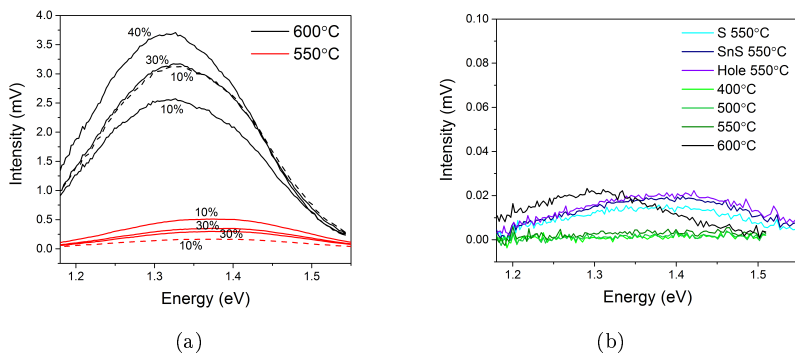

(a)

(b)

Figure 6.3: PL spectra of samples annealed with Na (a) and without Na (b). The samples without Na were annealed at 550°C and all had an intensity of below 0.02 mV. The dashed line in (a) is for films made with water as the solvent, while the solid lines are with ethanol. Water would in principle allow a higher solubility of NaCl, and accordingly the film at 600°C has a higher PL signal intensity, but the film annealed at 550°C does not. Measurement done by Andrea Crovetto. Figure adapted from **Paper IV**.

6.3.2 Photoluminescence of annealed ligand-free CZTS nanoparticle thin films with Na

The photoluminescence spectra of annealed samples with Na are displayed in Fig. 6.3(a). The highest intensity is achieved for the sample with 40% Na that was annealed at 600°C, and thus the longest electron lifetime in CZTS. Annealing at 600°C is significantly better than annealing at 550°C, which is consistent with the film morphologies observed in Chapter 5. Still, the samples with Na annealed at 550°C are significantly better than all samples without Na (Fig. 6.3(b)).
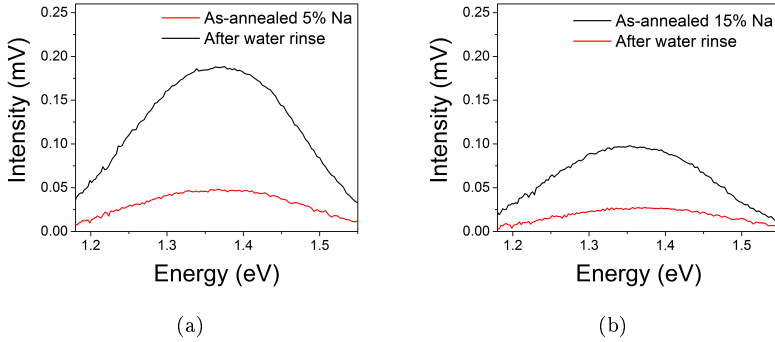
Figure 6.4: PL spectra of samples before and after water rinse, where (a) is for 5% Na, and (b) for 15% Na annealed. Both samples are annealed at 550°C for 30 min. Measurement done by Andrea Crovetto.

The energy of the emitted photons should for a defect-free material correspond to the band gap but be broadened by thermal distribution of energy states. Yet, the samples with Na that are annealed at 600°C peak between 1.3 eV and 1.33 eV, and at 1.37 eV for 550°C. This off-set from the CZTS band gap of 1.45-1.51 eV is commonly seen, and related to the existence of unwanted tail states in the CZTS system [203]. Na-inclusion has been seen to shift the PL peaks closer to the band gap, but it is not observed here [204]. The broadening of the peaks is also related to either band-to-tail or tail-to-band recombination, and reveals the existence of states within the band gap. As discussed in Chapter 1, several defect states, secondary phases, and disordering phenomena can exist in the Cu-Zn-Sn-S system, and will significantly lower the PL quantum yield by introducing non-radiative recombination pathways.

The PL intensity was also measured on samples after a quick water rinse, with the purpose to remove excess NaCl. As it is also customary to deposit the buffer layer in a water-based solution, all samples would experience this treatment anyway. The PL spectra before and after water rinse are showed in Fig. 6.4 for two different samples. Interestingly, the PL intensity decreases after water rinse, indicating a lower electron lifetime in CZTS. However, these are preliminary results, and a water rinse may not impact the absorber in a destructive manner as the buffer layer is deposited thereafter.

6.3.3   Solar cell annealed in selenium-atmosphere

To conclude this thesis, a device that was completed at NTU in Singapore will be presented. At NTU, they anneal in selenium atmosphere, and they have a well-established process for fabricating solar cells. The device characteristics of
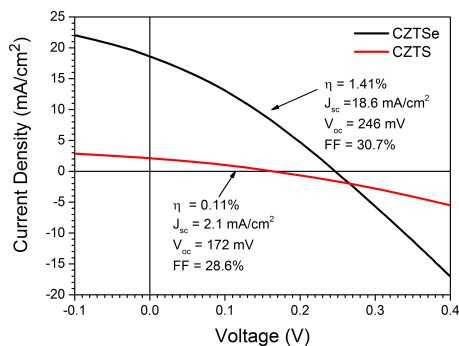
Figure 6.5: Photovoltaic performance of CZTSe solar cell fabricated with ligand-coated CZTS nanoparticles at DTU, but annealed in selenium atmosphere at NTU in Singapore. The device was also completed in Singapore. Measurement done by Zhanggang Li.

a solar cell made from ligand-coated CZTS nanoparticles synthesized at DTU and annealed at NTU can be seen in Fig. 6.5, with a comparison to a solar cell fabricated in-house at DTU. In total four samples were prepared at NTU, and the best efficiency was 1.41%, while the others were below 0.2%[1].

6.4 OUTLOOK

The best solar cell fabricated in-house had a power conversion efficiency of 0.2%, while the best solar cell fabricated at NTU had an efficiency of 1.4%. The increase in efficiency is mostly because of the higher short-circuit current-density. The improvement could both be a result of annealing in selenium atmosphere, as larger grains were observed, or a better quality of the remaining layers.

A high photoluminescence intensity is achieved for films with sodium, and a correlation between grain size and PL signal was seen. The next step should be to deposit a uniform film of appropriate thickness and with good contact to the other layers. Once this is carried out, a good solar cell efficiency may be achieved.

---

[1] This was the first time I tried doctor-blading, and there were cracks in the not-working samples.

CHAPTER 7

CONCLUSION

The aim of this thesis was to synthesize CZTS absorber materials that could be used to fabricate solar cells with a power conversion efficiency of 4%. This goal was not achieved. In fact, the highest efficiency obtained was 0.2%. However, other milestones have been reached in the process.

The first step of the solution-processing route is ink formation. At an early stage, we decided to pursue the nanoparticle ink approach, and nanoparticle synthesis was covered in Chapter 2. In a rather established field, two new synthesis recipes were developed with the aim of easier handling conditions and a better material for the subsequent processing steps. The first track concerned synthesis of large CZTSe nanoparticles with a wide size distribution. This was achieved by utilizing a two-step hot-injection method. The second track concerned developing nanoparticles without any hydrocarbon surface coatings, as these organic ligands have been challenging to remove in the succeeding annealing steps. By choosing suitable solvents and precursors, organic ligand-free nanoparticles were successfully synthesized in a facile one-step process. These particles further had the advantage that they could be dispersed in solvents such as water and ethanol, which makes them more practical for spray-coating. The composition could be tuned by changing the precursor concentration, but not always in a predictable manner. For particles synthesized with the optimal Cu-poor and Zn-rich composition, a SnS secondary phase as part of the nanoparticles was hard to avoid. As these particles should only function as the starting material for grain growth, and SnS was anticipated to evaporate during annealing, we did not try to control it further.

To better understand how the solvents and ligands are removed from the films and particles, the as-synthesized material was characterized by thermogravimetric analysis coupled with a mass spectrometry, as shown in Chapter 3. No clear difference was detected between using an atmosphere of nitrogen or forming gas. We saw that water and ethanol evaporate as whole molecules, while oleylamine

either thermally decomposes in smaller fragments or evaporates. The temperature required to remove part of the oleylamine ligands was almost 100°C above its boiling point.

In Chapter 5 and Chapter 6, the aim was to fabricate thin film absorber layers from CZTS nanoparticle and precursor inks. Films were deposited by a range of techniques, including spray-coating, doctor blading, and drop-casting. Converting the as-deposited amorphous or nanocrystalline thin films into an almost "monocrystalline" material is not very effective under the current sulfurization conditions. The literature on annealing of CZTS or CIGS nanoparticle thin films typically describes the presence of porous materials or of an organic layer at the back interface - which were also typical features in our absorbers. In the present work, we have shown that it is possible to achieve a dense material with micron-sized grains when removing the hydrocarbon ligands and employing a liquid phase additive during sintering. Sodium in the form of NaCl salt was for the first time dissolved directly in the nanoparticle ink. The addition of sodium had a significant impact, and it greatly enhanced both structural and optoelectronic properties of the films, but it also required an annealing temperature of 600°C.

7.1   IDEAS FOR FUTURE WORK

Whether or not it is environmentally-friendly to fabricate a solar cell at 600°C is open to discussion, and could be assessed with a life cycle analysis. The objective now should be to identify mild processing conditions that can enable higher performances in CZTS nanoparticle films deposited under ambient conditions. For liquid phase synthesis, the CZTS phase is formed at 220°C, while when sulfurizing precursors the CZTS phase is formed above 500°C. From a mild processing condition point of view, synthesizing CZTS nanoparticles at 220°C could therefore be favorable. The risk of annealing below 500°C is the formation of unwanted secondary and ternary phases, but this may be controlled by suitable vapor pressures of relevant species as well as fast sintering times. Utilizing the findings in Chapter 2 on how to synthesize larger particles, can also be useful. As proposed in the outlook of Chapter 5, finding a liquid phase additive that does not require a high temperature processing step to enhance the rate of densification, could be a good place to start.

On the contrary, instead of trying to counteract the porosity of the absorber, perhaps it would be better to exploit this inherent morphology. If the diffusion length is low because of traps in the material, maybe adapting a solar cell structure similar to many organic solar cells would be advantageous for solution-processed CZTS. Bulk hetero-junction (BHJ) solar cells are based on randomly mixed n- and p-type materials which will increase the junction interface. Surrounding this BHJ are a hole-blocking layer on one side, and an

electron-blocking layer on the other, which ensures that only the desired carriers can enter into the external circuit. For CZTS this would require a porous absorber layer, and an n-type material that can be deposited to fill out the voids and thus create a dense p-n junction. This layer could be deposited with chemical bath deposition, as CdS currently is, or with for example spin-coating. Obviously, the energy bands have to match CZTS, which could perhaps result in a better buffer layer than CdS in the end.

Bibliography

[1] J. Rockström, W. Steffen, K. Noone, Å. Persson, F. S. I. I. I. Chapin, E. Lambin, T. M. Lenton, M. Scheffer, C. Folke, H. J. Schellnhuber, B. Nykvist, C. A. de Wit, T. Hughes, S. V. D. Leeuw, H. Rodhe, S. Sörlin, P. K. Snyder, R. Costanza, U. Svedin, M. Falkenmark, L. Karlberg, R. W. Corell, V. J. Fabry, J. Hansen, B. Walker, D. Liverman, K. Richardson, P. Crutzen, and J. Foley, "Planetary Boundaries : Exploring the Safe Operating Space for Humanity," *Ecology and Society*, vol. 14, no. 2, p. 32, 2009.

[2] W. Steffen, K. Richardson, J. Rockström, S. E. Cornell, I. Fetzer, E. M. Bennett, R. Biggs, S. R. Carpenter, W. D. Vries, C. A. D. Wit, C. Folke, D. Gerten, J. Heinke, G. M. Mace, L. M. Persson, V. Ramanathan, B. Reyers, and S. Sörlin, "Planetary boundaries : Guiding changing planet," *Science*, vol. 347, no. 6223, pp. 1259855–1–10, 2015.

[3] W. Commission, "Report of the World Commission on Environment and Development : Our Common Future," tech. rep., 1987.

[4] N. S. Lewis, "Powering the Planet," *MRS Bulletin*, vol. 32, no. October, pp. 808–820, 2007.

[5] O. Morton, "A New Day Dawning?," *Nature*, vol. 443, no. September, pp. 19–22, 2006.

[6] S. Philipps and W. Warmuth, "Photovoltaics report," tech. rep., Fraunhofer Institute for Solar Energy Systems, ISE, 2016.

[7] Fraunhofer ISE, "Current and Future Cost of Solar Photovoltaics - Longterm Scenarios for Market Development, System Prices and LCOE of

Utility-Scale PV Systems," tech. rep., Agora Energiwende, Freiburg, Germany, 2015.

[8] S. Henbest and E. Giannakopoulou, "New Energy Outlook 2015: Long-term Projections of the Global Energy Sector," tech. rep., Bloomberg New Energy Finance, 2015.

[9] M. A. Green, "Commercial progress and challenges for photovoltaics," *Nature Energy*, vol. 1, no. January, pp. 1–4, 2016.

[10] K. P. Bhandari, J. M. Collier, R. J. Ellingson, and D. S. Apul, "Energy payback time (EPBT) and energy return on energy invested (EROI) of solar photovoltaic systems: A systematic review and meta-analysis," *Renewable and Sustainable Energy Reviews*, vol. 47, pp. 133–141, 2015.

[11] K. Ito, "An Overview of CZTS-Based Thin-Film Solar Cells," in *Copper Zinc Tin Sulfide-Based Thin-Film Solar Cells* (K. Ito, ed.), ch. 1, pp. 3–41, Nagano, Japan: Wiley, 1st ed., 2015.

[12] P. Jackson, R. Wuerz, D. Hariskos, E. Lotter, W. Witte, and M. Powalla, "Effects of heavy alkali elements in Cu(In,Ga)Se2 solar cells with efficiencies up to 22.6%," *Physica Status Solidi - Rapid Research Letters*, vol. 10, no. 8, pp. 583–586, 2016.

[13] E. Wesoff, "First Solar Hits Record 22.1% Conversion Efficiency for CdTe Solar Cell," 2016.

[14] Y. S. Lee, T. Gershon, O. Gunawan, T. K. Todorov, T. Gokmen, Y. Virgus, and S. Guha, "Cu2ZnSnSe4 thin-film solar cells by thermal co-evaporation with 11.6% efficiency and improved minority carrier diffusion length," *Advanced Energy Materials*, vol. 1401372, pp. 1–4, 2014.

[15] "Web of Science," 2016.

[16] K. Ito and T. Nakazawa, "Electrical and Optical Properties of Stannite-Type Quaternary Semiconductor Thin Films," *Jpn. J. Appl. Phys*, vol. 27, no. 11, pp. 2094–2097, 1988.

[17] H. Katagiri, N. Sasaguchi, S. Hando, S. Hoshino, J. Ohashi, and T. Yokota, "Preparation and evaluation of Cu2ZnSnS4 thin films by sulfurization of E-B evaporated precursors," *Solar Energy Materials and Solar Cells*, vol. 49, no. 1-4, pp. 407–414, 1997.

[18] H. Katagiri, K. Saitoh, T. Washio, H. Shinohara, T. Kurumadani, and S. Miyajima, "Development of thin film solar cell based on Cu2ZnSnS4 thin films," *Solar Energy Materials and Solar Cells*, vol. 65, no. 1, pp. 141–148, 2001.

[19] B.-A. Schubert, B. Marsen, S. Cinque, T. Unold, R. Klenk, S. Schorr, and H.-W. Schock, "Cu2ZnSnS4 thin film solar cells by fast coevaporation," *Prog. Photovolt: Res. Appl.*, vol. 19, pp. 93–96, 2011.

[20] H. Katagiri, K. Jimbo, S. Yamada, T. Kamimura, W. S. Maw, T. Fukano, T. Ito, and T. Motohiro, "Enhanced conversion efficiencies of Cu2ZnSnS4-based thin film solar cells by using preferential etching technique," *Applied Physics Express*, vol. 1, no. 4, pp. 0412011–0412012, 2008.

[21] S. Tajima, T. Itoh, H. Hazama, K. Ohishi, and R. Asahi, "Improvement of the open-circuit voltage of Cu2ZnSnS4 solar cells using a two-layer structure," *Applied Physics Express*, vol. 8, no. 8, p. 82302, 2015.

[22] K. Sun, C. Yan, F. Liu, J. Huang, F. Zhou, J. A. Stride, M. Green, and X. Hao, "Over 9% Efficient Kesterite Cu2ZnSnS4 Solar Cell Fabricated by Using Zn1-xCdxS Buffer Layer," *Advanced Energy Materials*, vol. 6, no. 1600046, pp. 1–5, 2016.

[23] S. Tajima, "Cu2ZnSnS4 photovoltaic cell with improved efficiency using high-temperature annealing after CdS buffer layer deposition," *Progress in Photovoltaics: Research and Applications*, 2016.

[24] X. Jin, J. Li, G. Chen, C. Xue, W. Liu, and C. Zhu, "Preparation of Cu2ZnSnS4-based thin film solar cells by a combustion method," *Solar Energy Materials and Solar Cells*, vol. 146, pp. 16–24, 2016.

[25] N. Nakayama and K. Ito, "Sprayed films of stannite Cu2ZnSnS4," *Applied Surface Science*, vol. 92, pp. 171–175, 1996.

[26] C. Steinhagen, M. G. Panthani, V. Akhavan, B. Goodfellow, B. Koo, and B. A. Korgel, "Synthesis of Cu2ZnSnS4 Nanocrystals for Use in Low-Cost Photovoltaics," *J. Am. Chem. Soc.*, vol. 131, pp. 12554–12555, 2009.

[27] U. V. Ghorpade, M. P. Suryawanshi, and W. Shin, "Wurtzite CZTS nanocrystals and phase evolution to kesterite thin film for solar energy harvesting," *Physical Chemistry Chemical Physics*, vol. 17, pp. 19777–19788, 2015.

[28] E. Gu, C. Yan, F. Liu, Y. Liu, Z. Su, K. Zhang, Z. Chen, J. Li, and Y. Liu, "Cu2ZnSnS4 Thin Film Solar Cells From Coated Nanocrystals Ink," *Journal of Materials Science: Materials in Electronics*, vol. 26, no. 3, pp. 1932–1939, 2015.

[29] E. M. Mkawi, K. Ibrahim, M. K. M. Ali, M. a. Farrukh, and N. K. Allam, "Solvent solution-dependent properties of nonstoichiometric cubic Cu2ZnSnS4 nanoparticles," *Chemical Physics Letters*, vol. 608, pp. 393–397, 2014.

[30] Q. Tian, X. Xu, L. Han, M. Tang, R. Zou, Z. Chen, M. Yu, J. Yang, and J. Hu, "Hydrophilic Cu2ZnSnS4 nanocrystals for printing flexible, low-cost and environmentally friendly solar cells," *CrystEngComm*, vol. 14, no. 11, p. 3847, 2012.

[31] X. Liu, F. Zhou, N. Song, J. Huang, C. Yan, F. Liu, K. Sun, J. A. Stride, X. Hao, and M. Green, "Exploring the Application of Quaternary Metastable Wurtzite Nanocrystals in Pure-sulfide Cu2ZnSnS4 Solar Cells by Forming Nearly Micron-sized Large Grains," *J. Mater. Chem. A*, vol. 3, pp. 23185–23193, 2015.

[32] D. Tiwari, T. Koehler, X. Lin, R. Harniman, I. Griffiths, L. Wang, D. Cherns, R. Klenk, and D. J. Fermin, "Cu2ZnSnS4 thin-films generated from a single solution based precursor: the effect of Na and Sb doping," *Chemistry of Materials*, vol. 28, pp. 4991–4997, 2016.

[33] K. Woo, Y. Kim, and J. Moon, "A non-toxic, solution-processed, earth abundant absorbing layer for thin-film solar cells," *Energy & Environmental Science*, vol. 5, no. 1, p. 5340, 2012.

[34] S.-N. Park, S.-J. Sung, J.-H. Sim, K.-J. Yang, D.-K. Hwang, J. Kim, G. Y. Kim, W. Jo, D.-H. Kim, and J.-K. Kang, "Nanostructured p-type CZTS thin films prepared by a facile solution process for 3D p-n junction solar cells.," *Nanoscale*, vol. 7, no. 25, pp. 11182–9, 2015.

[35] G. Larramona, S. Bourdais, A. Jacob, C. Choné, T. Muto, Y. Cuccaro, B. Delatouche, C. Moisan, D. Péré, and G. Dennler, "Efficient Cu2ZnSnS4 solar cells spray coated from a hydro-alcoholic colloid synthesized by instantaneous reaction," *RSC Advances*, vol. 4, no. 28, p. 14655, 2014.

[36] F. Zhou, F. Zeng, X. Liu, F. Liu, N. Song, C. Yan, A. Pu, J. Park, K. Sun, and X. Hao, "Improvement of Jsc in a Cu2ZnSnS4 Solar Cell by Using a Thin Carbon Intermediate Layer at the Cu2ZnSnS4/Mo Interface," *ACS Applied Materials and Interfaces*, vol. 7, no. 41, pp. 22868–22873, 2015.

[37] K. Tanaka, "CZTS Thin Films Prepared by a Non-Vacuum Process," in *CZTS Thin Films Prepared by a Non-Vacuum Process* (K. Ito, ed.), no. 1, ch. 12, pp. 271–288, John Wiley & Sons Ltd, 1 ed., 2015.

[38] F. Jiang, S. Ikeda, T. Harada, and M. Matsumura, "Pure Sulfide Cu2ZnSnS4 thin film solar cells fabricated by preheating an electrodeposited metallic stack," *Advanced Energy Materials*, vol. 4, no. 7, pp. 2–5, 2014.

[39] A. Ennaoui, M. C. Lux-Steiner, A. Weber, D. Abou-Ras, I. Kötschau, H. W. Schock, R. Schurr, A. Hölzing, S. Jost, R. Hock, T. Vos, J. Schulze,

and A. Kirbs, "Cu2ZnSnS4 thin film solar cells from electroplated precursors: Novel low-cost perspective," *Thin Solid Films*, vol. 517, no. 7, pp. 2511–2514, 2009.

[40] X. Lin, J. Kavalakkatt, K. Kornhuber, S. Levcenko, M. C. Lux-Steiner, and A. Ennaoui, "Structural and optical properties of Cu2ZnSnS4 thin film absorbers from ZnS and Cu3SnS4 nanoparticle precursors," *Thin Solid Films*, vol. 535, no. 1, pp. 10–13, 2013.

[41] W. Wang, M. T. Winkler, O. Gunawan, T. Gokmen, T. K. Todorov, Y. Zhu, and D. B. Mitzi, "Device characteristics of CZTSSe thin-film solar cells with 12.6% efficiency," *Advanced Energy Materials*, vol. 4, no. 7, pp. 1–5, 2014.

[42] C. K. Miskin, W.-C. Yang, C. J. Hages, N. J. Carter, C. S. Jogekar, E. A. Stach, and R. Agrawal, "Solar Cells Utilizing Small Molecular Weight Organic Semiconductors," *Prog. Photovolt: Res. Appl.*, vol. 15, no. February 2013, pp. 659–676, 2014.

[43] G. Larramona, A. Jacob, C. Chone, T. Muto, Y. Cuccaro, B. Delatouche, C. Moisan, D. Pe, G. Dennler, I. E. S. A. S, A. Caquot, and S. A. Cedex, "8.6% Efficient CZTSSe Solar Cells Sprayed from Water-Ethanol CZTS Colloidal Solutions," *J. Phys. Chem. Lett.*, vol. 5, pp. 3763–3767, 2014.

[44] C. Persson, R. Chen, H. Zhao, and M. Kumar, "Electronic Structure and Optical Properties from First-Principles Modeling," in *Copper Zinc Tin Sulfide-Based Thin-Film Solar Cells* (K. Ito, ed.), vol. 1, ch. 4, pp. 75–106, Nagano, Japan: Wiley, 1 ed., 2015.

[45] S. Schorr, "Crystallographic Aspects of Cu2ZnSnS4 (CZTS)," in *Copper Zinc Tin Sulfide-Based Thin Film Solar Cells* (K. Ito, ed.), ch. 3, pp. 55–73, John Wiley & Sons Ltd, 1 ed., 2015.

[46] Q. Guo, H. W. Hillhouse, and R. Agrawal, "Synthesis of Cu2ZnSnS4 Nanocrystal Ink and Its Use for Solar Cells," *J. Am. Chem. Soc.*, vol. 131, pp. 11672–11673, 2009.

[47] S. Chen, A. Walsh, X. G. Gong, and S. H. Wei, "Classification of lattice defects in the kesterite Cu2ZnSnS 4 and Cu2ZnSnSe4 earth-abundant solar cell absorbers," *Advanced Materials*, vol. 25, no. 11, pp. 1522–1539, 2013.

[48] J. J. Scragg, J. T. Watjen, M. Edoff, T. Ericson, T. Kubart, and C. Platzer-Bjorkman, "A Detrimental Reaction at the Molybdenum Back Contact in Cu2ZnSn(S,Se)(4) Thin-Film Solar Cells," *Journal of the American Chemical Society*, vol. 134, no. 47, pp. 19330–19333, 2012.

[49] K.-J. Yang, J.-H. Sim, B. Jeon, D.-H. Son, D.-H. Kim, S.-J. Sung, D.-K. Hwang, D. B. K. Soomin Song, J. Kim, and J.-K. Kang, "Effects of Na and MoS2 on Cu2ZnSnS4 thin-film solar cell," *Prog. Photovolt: Res. Appl.*, vol. 23, pp. 862–873, 2015.

[50] J. J. Scragg, T. Kubart, J. T. Wätjen, T. Ericson, M. K. Linnarsson, and C. Platzer-Björkman, "Effects of Back Contact Instability on Cu2ZnSnS4 Devices and Processes," *Chemistry of Materials*, vol. 25, pp. 3162–3171, 2013.

[51] "International Crystal Structure Database," 2017.

[52] C. Frisk, T. Ericson, S. Y. Li, P. Szaniawski, J. Olsson, and C. Platzer-Björkman, "Combining strong interface recombination with bandgap narrowing and short diffusion length in Cu2ZnSnS4 device modeling," *Solar Energy Materials and Solar Cells*, vol. 144, pp. 364–370, 2016.

[53] A. Walsh, S. Chen, S. H. Wei, and X. G. Gong, "Kesterite thin-film solar cells: Advances in materials modelling of Cu 2 ZnSnS 4," *Advanced Energy Materials*, vol. 2, no. 4, pp. 400–409, 2012.

[54] J. J. Scragg, L. Choubrac, A. Lafond, T. Ericson, and C. Platzer-Björkman, "A low-temperature order-disorder transition in Cu2ZnSnS4 thin films," *Applied Physics Letters*, vol. 104, no. 041911, pp. 1–4, 2014.

[55] S. Schorr, "The crystal structure of kesterite type compounds: A neutron and X-ray diffraction study," *Solar Energy Materials and Solar Cells*, vol. 95, no. 6, pp. 1482–1488, 2011.

[56] M.-C. Huang, S.-Y. Wei, C.-H. Hsu, W.-H. Ho, Y.-S. Su, and C.-H. Lai, "Effect of injection rate on the growth of Cu2ZnSnS4 nanoparticles synthesized by hot injection method," in *2013 IEEE 39th Photovoltaic Specialists Conference (PVSC)*, pp. 0380–0382, 2013.

[57] H. Du, F. Yan, M. Young, B. To, C. S. Jiang, P. Dippo, D. Kuciauskas, Z. Chi, E. A. Lund, C. Hancock, W. M. Hlaing Oo, M. A. Scarpulla, and G. Teeter, "Investigation of combinatorial coevaporated thin film Cu2ZnSnS4. I. Temperature effect, crystalline phases, morphology, and photoluminescence," *Journal of Applied Physics*, vol. 115, no. 173502, pp. 1–14, 2014.

[58] M. Kumar, A. Dubey, N. Adhikari, S. Venkatesan, and Q. Qiao, "Strategic review of secondary phases, defects and defect-complexes in kesterite CZTS–Se solar cells," *Energy Environ. Sci.*, vol. 8, no. 11, pp. 3134–3159, 2015.

[59] D. M. Berg and P. J. Dale, "Kesterite: Equilibria and Secondary Phase Identification," in *Copper Zinc Tin Sulfide-Based Thin Film Solar Cells* (K. Ito, ed.), vol. 1, ch. 5, pp. 107–132, Newark, Delaware: Wiley, 1st ed., 2015.

[60] "PVEducation," 2017.

[61] A. Redinger and S. Siebentritt, "Loss Mechanisms in Kesterite Solar Cells," in *Copper Zinc Tin Sulfide-Based Thin-Film Solar Cells* (K. Ito, ed.), vol. 1, ch. 16, pp. 363–386, Belvaux, Luxembourg: John Wiley & Sons, Ltd, 1st ed., 2015.

[62] W. Shockley and H. J. Queisser, "Detailed balance limit of efficiency of p-n junction solar cells," *Journal of Applied Physics*, vol. 32, no. 3, pp. 510–519, 1961.

[63] X. Liu, Y. Feng, H. Cui, F. Liu, X. Hao, G. Conibeer, D. B. Mitzi, and M. Green, "The current status and future prospects of kesterite solar cells: a brief review," *Prog. Photovolt: Res. Appl.*, vol. 24, pp. 879–898, 2016.

[64] European Commission, "On the review of the list of critical raw materials for the EU and the implementation of the Raw Materials Initiative," tech. rep., 2014.

[65] S. Chu, "U.S. Department of Energy - Critical Materials Strategy," tech. rep., U.S. Department of Energy, 2011.

[66] C. S. Tao, J. Jiang, and M. Tao, "Natural resource limitations to terawatt-scale solar cells," *Solar Energy Materials and Solar Cells*, vol. 95, no. 12, pp. 3176–3180, 2011.

[67] A. Feltrin and A. Freundlich, "Material challenges for terawatt level deployment of photovoltaics," *Conference Record of the 2006 IEEE 4th World Conference on Photovoltaic Energy Conversion, WCPEC-4*, vol. 2, pp. 2469–2472, 2008.

[68] V. Fthenakis, "Sustainability of photovoltaics: The case for thin-film solar cells," *Renewable and Sustainable Energy Reviews*, vol. 13, no. 9, pp. 2746–2750, 2009.

[69] C. Candelise, J. F. Spiers, and R. J. K. Gross, "Materials availability for thin film (TF) PV technologies development: A real concern?," *Renewable and Sustainable Energy Reviews*, vol. 15, no. 9, pp. 4972–4981, 2012.

[70] H. Wang, "Progress in thin film solar cells based on Cu2ZnSnS4," *International Journal of Photoenergy*, vol. 2011, 2011.

[71] J. Collier, S. Wu, and D. Apul, "Life cycle environmental impacts from CZTS (copper zinc tin sulfide) and Zn3P2 (zinc phosphide) thin film PV (photovoltaic) cells," *Energy*, vol. 74, no. C, pp. 314–321, 2014.

[72] G. Finnveden, M. Z. Hauschild, T. Ekvall, J. Guinée, R. Heijungs, S. Hellweg, A. Koehler, D. Pennington, and S. Suh, "Recent developments in Life Cycle Assessment," *Journal of Environmental Management*, vol. 91, no. 1, pp. 1–21, 2009.

[73] World Health Organization, "Ten chemicals of major public health concern," 2016.

[74] V. M. Fthenakis, M. Fuhrmann, J. Heiser, A. Lanzirotti, J. Fitts, and W. Wang, "Emissions and encapsulation of cadmium in CdTe PV modules during fires," *Progress in Photovoltaics: Research and Applications*, vol. 13, no. 8, pp. 713–723, 2005.

[75] D. Hironiwa, N. Matsuo, N. Sakai, T. Katou, H. Sugimoto, J. Chantana, Z. Tang, and T. Minemoto, "Sputtered (Zn,Mg)O buffer layer for band offset control in Cu2ZnSn(S,Se)4 solar cells," *Japanese Journal of Applied Physics*, vol. 53, no. 10, p. 106502, 2014.

[76] N. Sakai, H. Hiroi, and H. Sugimoto, "Development of Cd-free buffer layer for Cu2ZnSnS4 thin-film solar cells," *IEEE*, pp. 3654–3657, 2011.

[77] T. Ericson, J. J. Scragg, A. Hulqvist, J. T. Wätjen, P. Szaniawaki, T. Törndahl, and C. Platzer-Björkman, "Zn(O,S) Buffer Layers and Thickness Variations of CdS Buffer for Cu2ZnSnS4 Solar Cells," *IEEE Journal of Photovoltaics*, vol. 4, no. 1, pp. 465–469, 2014.

[78] M. Nguyen, K. Ernits, K. F. Tai, C. F. Ng, S. S. Pramana, W. A. Sasangka, S. K. Batabyal, T. Holopainen, D. Meissner, A. Neisser, and L. H.Wong, "ZnS buffer layer for Cu2ZnSn(SSe)4 monograin layer solar cell," *Solar Energy*, vol. 111, pp. 344–349, 2015.

[79] S. K. Saha, A. Guchhait, and A. J. Pal, "Cu2ZnSnS4 (CZTS) nanoparticle based nontoxic and earth-abundant hybrid pn-junction solar cells.," *Physical Chemistry Chemical Physics*, vol. 14, no. 22, pp. 8090–6, 2012.

[80] R. H. Reuss and B. R. Chalamala, "Introduction to Solution-Deposited Inorganic Electronics," in *Solution Processing of Inorganic Materials* (D. B. Mitzi, ed.), ch. 1, pp. 1–32, Hoboken, New Jersey: John Wiley & Sons, Inc, 1 ed., 2009.

[81] F. C. Krebs, "Fabrication and processing of polymer solar cells: A review of printing and coating techniques," *Solar Energy Materials and Solar Cells*, vol. 93, no. 4, pp. 394–412, 2009.

[82] S. E. Habas, H. A. S. Platt, M. F. A. M. V. Hest, and D. S. Ginley, "Low-Cost Inorganic Solar Cells: From Ink To Printed Device," *Chem. Rev.*, vol. 110, pp. 6571–6594, 2010.

[83] R. W. Schwartz and M. Narayanan, "Chemical solution deposition — basic principles," in *Solution Processing of Inorganic Materials* (D. B. Mitzi, ed.), ch. 2, pp. 33–76, John Wiley & Sons, Inc, 2009.

[84] C. B. Murray, C. R. Kagan, and M. G. Bawendi, "synthesis and characterization of monodisperse nanocrystals and close-packed nanocrystal assemblies," *Annual Reviews in Material Science*, vol. 30, pp. 545–610, 2000.

[85] A. Khare, A. W. Wills, L. M. Ammerman, D. J. Norris, and E. S. Aydil, "Size control and quantum confinement in Cu2ZnSnS4 nanocrystals.," *Chemical communications*, vol. 47, no. 42, pp. 11721–11723, 2011.

[86] K. Lu, "Nanoparticle synthesis," in *Nanoparticulate Materials: Synthesis, Characterization, and Processing*, ch. 2, pp. 24–126, John Wiley & Sons, Inc, 1st ed., 2013.

[87] J.-k. Park, J. Jeong, Y. Kim, B. Kim, and S.-h. Cho, "Solvent-free synthesis of Cu2ZnSnS4 nanocrystals: a facile, green, up-scalable route for low cost photovoltaic cells," *Nanoscale*, vol. 6, pp. 11703–11711, 2014.

[88] A. Ritscher, J. Just, O. Dolotko, S. Schorr, and M. Lerch, "A mechanochemical route to single phase Cu2ZnSnS4 powder," *Journal of Alloys and Compounds*, vol. 670, no. 82, pp. 289–296, 2016.

[89] S. Schorr, H.-J. Hoebler, and M. Tovar, "A neutron diffraction study of the stannite-kesterite solid solution series," *European Journal of Mineralogy*, vol. 19, pp. 65–73, 2007.

[90] Y. Zhao, W.-H. Zhou, J. Jiao, Z.-J. Zhou, and S.-X. Wu, "Aqueous synthesis and characterization of hydrophilic Cu2ZnSnS4 nanocrystals," *Materials Letters*, vol. 96, pp. 174–176, 2013.

[91] O. Zaberca, F. Oftinger, J. Y. Chane-Ching, L. Datas, a. Lafond, P. Puech, a. Balocchi, D. Lagarde, and X. Marie, "Surfactant-free CZTS nanoparticles as building blocks for low-cost solar cell absorbers," *Nanotechnology*, vol. 23, p. 185402, 2012.

[92] C. C. Kang, H. F. Chen, T. C. Yu, and T. C. Lin, "Aqueous synthesis of wurtzite Cu2ZnSnS4 nanocrystals," *Materials Letters*, vol. 96, pp. 24–26, 2013.

[93] M. Cao and Y. Shen, "A mild solvothermal route to kesterite quaternary Cu2ZnSnS4 nanoparticles," *Journal of Crystal Growth*, vol. 318, no. 1, pp. 1117–1120, 2011.

[94] W. Xie, X. Jiang, C. Zou, D. Li, J. Zhang, J. Quan, and L. Shao, "Synthesis of highly dispersed Cu2ZnSnS4 nanoparticles by solvothermal method for photovoltaic application," *Physica E: Low-dimensional Systems and Nanostructures*, vol. 45, pp. 16–20, 2012.

[95] V. T. Tiong, Y. Zhang, J. Bell, and H. Wang, "Phase-selective hydrothermal synthesis of Cu2ZnSnS4 nanocrystals: the effect of the sulphur precursor," *CrystEngComm*, vol. 16, no. 20, pp. 4306–4313, 2014.

[96] Y. L. Zhou, W. H. Zhou, Y. F. Du, M. Li, and S. X. Wu, "Sphere-like kesterite Cu2ZnSnS4 nanoparticles synthesized by a facile solvothermal method," *Materials Letters*, vol. 65, no. 11, pp. 1535–1537, 2011.

[97] B. Flynn, W. Wang, C. H. Chang, and G. S. Herman, "Microwave assisted synthesis of Cu2ZnSnS4 colloidal nanoparticle inks," *Physica Status Solidi (A) Applications and Materials Science*, vol. 209, no. 11, pp. 2186–2194, 2012.

[98] P. K. Sarswat and M. L. Free, "An investigation of rapidly synthesized Cu2ZnSnS4 nanocrystals," *Journal of Crystal Growth*, vol. 372, pp. 87–94, 2013.

[99] C. B. Murray, D. J. Norris, and M. G. Bawendi, "Synthesis and Characterization of Nearly Monodisperse CdE (E = S, Se, Te) Semiconductor Nanocrystallites," *J. Am. Chem. Soc.*, vol. 115, no. 19, pp. 8706–8715, 1993.

[100] R. W. Balluffi, S. M. Allen, and W. C. Carter, *Kinetics of Materials*. Hoboken, New Jersey: John Wiley & Sons, 1st ed., 2005.

[101] V. I. Kalikmanov, *Nucelation Theory - Lecture Notes in Physics 860*. Heidelberh: Springer, 2013.

[102] J. Polte, "Fundamental Growth Principles of Colloidal Metal Nanoparticles - a new Perspective," *CrystEngComm*, vol. 17, no. 5, pp. 6809–6830, 2015.

[103] V. K. LaMer and R. H. Dinegar, "Theory, Production and Mechanism of Formation of Monodisperse Hydrosols," *J. Am. Chem. Soc.*, vol. 72, no. 11, pp. 4847–4854, 1950.

[104] V. K. LaMer, "Nucleation in Phase Transitions," *Ind. Eng. Chem.*, vol. 44, no. 6, pp. 1270–1277, 1952.

[105] T. Sugimoto, "Preparation of Monodisperse Colloidal Particles," *Adv. Colloid Interface Sci.*, vol. 28, pp. 65–108, 1987.

[106] J. A. Lewis, "Colloidal Processing of Ceramics," *J. Am. Ceram. Soc.*, vol. 83, no. 10, pp. 2341–59, 2000.

[107] B. S. Tosun, B. D. Chernomordik, A. a. Gunawan, B. Williams, K. A. Mkhoyan, L. F. Francis, and E. S. Aydil, "Cu2ZnSnS4 nanocrystal dispersions in polar liquids.," *Chemical communications*, vol. 49, no. 34, pp. 3549–51, 2013.

[108] C. Coughlan and K. M. Ryan, "Complete study of the composition and shape evolution in the synthesis of Cu2ZnSnS4 (CZTS) semiconductor nanocrystals," *CrystEngComm*, vol. 17, no. 36, pp. 6914–6922, 2015.

[109] T. Kameyama, T. Osaki, K.-i. Okazaki, T. Shibayama, A. Kudo, S. Kuwabata, and T. Torimoto, "Preparation and photoelectrochemical properties of densely immobilized Cu2ZnSnS4 nanoparticle films," *Journal of Materials Chemistry*, vol. 20, no. 25, p. 5319, 2010.

[110] M. V. Kovalenko, L. Manna, A. Cabot, Z. Hens, D. V. Talapin, C. R. Kagan, X. V. I. Klimov, A. L. Rogach, P. Reiss, D. J. Milliron, P. Guyot-sionnnest, G. Konstantatos, W. J. Parak, T. Hyeon, B. A. Korgel, C. B. Murray, and W. Heiss, "Prospects of Nanoscience with Nanocrystals," *ACS Nano*, vol. 9, no. 2, pp. 1012–1057, 2015.

[111] Z. Li, A. L. K. Lui, K. H. Lam, L. Xi, and Y. M. Lam, "Phase-Selective Synthesis of Cu2ZnSnS4 Nanocrystals using Different Sulfur Precursors," *Inorganic Chemistry*, vol. 53, no. 20, pp. 10874–10880, 2014.

[112] S. W. Shin, J. H. Han, C. Y. Park, S. R. Kim, Y. C. Park, G. L. Agawane, A. V. Moholkar, J. H. Yun, C. H. Jeong, J. Y. Lee, and J. H. Kim, "A facile and low cost synthesis of earth abundant element Cu2ZnSnS4 (CZTS) nanocrystals: Effect of Cu concentrations," *Journal of Alloys and Compounds*, vol. 541, pp. 192–197, 2012.

[113] J. Chang and E. R. Waclawik, "Controlled synthesis of CuInS2, Cu2SnS3 and Cu2ZnSnS4 nano-structures: insight into the universal phase-selectivity mechanism," *CrystEngComm*, vol. 15, no. 28, pp. 5612–5619, 2013.

[114] M. Li, W. H. Zhou, J. Guo, Y. L. Zhou, Z. L. Hou, J. Jiao, Z. J. Zhou, Z. L. Du, and S. X. Wu, "Synthesis of pure metastable wurtzite CZTS nanocrystals by facile one-pot method," *Journal of Physical Chemistry C*, vol. 116, no. 50, pp. 26507–26516, 2012.

[115] Y. Yin and A. P. Alivisatos, "Colloidal nanocrystal synthesis and the organic-inorganic interface.," *Nature*, vol. 437, no. 7059, pp. 664–670, 2005.

[116] D. F. Shriver and M. A. Drezdzon, *The Manipulation of Air-Sensitive Compounds.* John Wiley & Sons, 2nd ed., 1986.

[117] P. Reiss, M. Carrière, C. Lincheneau, L. Vaure, and S. Tamang, "Synthesis of Semiconductor Nanocrystals, Focusing on Nontoxic and Earth-Abundant Materials," *Chemical Reviews*, p. acs.chemrev.6b00116, 2016.

[118] R. Mainz, E. Simsek Sanli, H. Stange, D. Azulay, S. Brunken, D. Greiner, S. Hajaj, M. D. Heinemann, C. A. Kaufmann, M. Klaus, Q. M. Ramasse, H. Rodriguez-Alvarez, A. Weber, I. Balberg, O. Millo, P. A. van Aken, and D. Abou-Ras, "Annihilation of structural defects in chalcogenide absorber films for high-efficiency solar cells," *Energy Environ. Sci.*, vol. 9, no. 5, pp. 1818–1827, 2016.

[119] D. M. Berg, *Kesterite equilibrium reaction and the discrimination of secondary phases from Cu2ZnSnS4*. PhD thesis, University of Luxembourg, 2012.

[120] M. Dimitrievska, A. Fairbrother, X. Fontané, T. Jawhari, V. Izquierdo-Roca, E. Saucedo, and A. Pérez-Rodríguez, "Multiwavelength excitation Raman scattering study of polycrystalline kesterite Cu2ZnSnS4 thin films," *Applied Physics Letters*, vol. 104, no. 2, 2014.

[121] X. Fontané, L. Calvo-Barrio, V. Izquierdo-Roca, E. Saucedo, A. Pérez-Rodríguez, J. R. Morante, D. M. Berg, P. J. Dale, and S. Siebentritt, "In-depth resolved Raman scattering analysis for the identification of secondary phases: Characterization of Cu2ZnSnS4 layers for solar cell applications," *Applied Physics Letters*, vol. 98, no. 18, p. 181905, 2011.

[122] M. Grossberg, J. Krustok, J. Raudoja, K. Timmo, M. Altosaar, and T. Raadik, "Photoluminescence and Raman study of Cu2ZnSn(SexS1-x)4 monograins for photovoltaic applications," *Thin Solid Films*, vol. 519, no. 21, pp. 7403–7406, 2011.

[123] P. A. Fernandes, P. M. P. Salomé, and A. F. da Cunha, "A study of ternary Cu2SnS3 and Cu3SnS4 thin films prepared by sulfurizing stacked metal precursors," *J. Phys. D. Appl. Phys.*, vol. 43, no. 21, p. 215403, 2010.

[124] P. A. Fernandes, P. M. P. Salomé, and A. F. Da Cunha, "Study of polycrystalline Cu2ZnSnS4 films by Raman scattering," *Journal of Alloys and Compounds*, vol. 509, no. 28, pp. 7600–7606, 2011.

[125] D. M. Berg, R. Djemour, L. Gütay, S. Siebentritt, P. J. Dale, X. Fontane, V. Izquierdo-Roca, and A. Pérez-Rodriguez, "Raman analysis of monoclinic Cu2SnS3 thin films," *Applied Physics Letters*, vol. 100, no. 19, p. 192103, 2012.

[126] A. Crovetto, R. Chen, R. B. Ettlinger, A. C. Cazzaniga, J. Schou, C. Persson, and O. Hansen, "Dielectric function and double absorption onset of

monoclinic Cu2SnS3: Origin of experimental features explained by first-principles calculations," *Solar Energy Materials and Solar Cells*, vol. 154, pp. 121–129, 2016.

[127] L. S. Price, I. P. Parkin, A. M. E. Hardy, R. J. H. Clark, T. G. Hibbert, and K. C. Molloy, "Atmospheric Pressure Chemical Vapor Deposition of Tin Sulfides (SnS, Sn2S3 , and SnS2) on Glass," *Chemistry of Materials*, vol. 11, no. 7, pp. 1792–1799, 1999.

[128] I. P. Parkin, L. S. Price, T. G. Hibbert, and K. C. Molloy, "The first single source deposition of tin sulfide coatings on glass: aerosol-assisted chemical vapour deposition using [Sn(SCH2CH2S)2]," *Journal of Materials Chemistry*, vol. 11, no. 5, pp. 1486–1490, 2001.

[129] H. Harima, "Raman scattering characterization on SiC," *Microelectronic Engineering*, vol. 83, no. 1 SPEC. ISS., pp. 126–129, 2006.

[130] P. A. Fernandes, P. M. P. Salomé, and A. F. da Cunha, "Growth and Raman scattering characterization of Cu2ZnSnS4 thin films," *Thin Solid Films*, vol. 517, no. 7, pp. 2519–2523, 2009.

[131] S. Mourdikoudis and L. M. Liz-Marzán, "Oleyamine in Nanoparticle Synthesis," *Chem. Mater.*, vol. 25, p. 1465, 2013.

[132] H.-I. Hsiang, C.-T. Yang, and J.-H. Tu, "Characterization of CuSbSe2 crystallites synthesized using a hot injection method," *RSC Adv.*, 2016.

[133] B. Hou, D. Benito-Alifonso, N. Kattan, D. Cherns, M. C. Galan, and D. J. Fermín, "Initial stages in the formation of Cu2ZnSn(S,Se)4 nanoparticles," *Chemistry - A European Journal*, vol. 19, no. 47, pp. 15847–15851, 2013.

[134] J. Van Embden, A. S. R. Chesman, and J. J. Jasieniak, "The heat-up synthesis of colloidal nanocrystals," *Chemistry of Materials*, vol. 27, no. 7, pp. 2246–2285, 2015.

[135] A. Shavel, M. Ibáñez, Z. Luo, J. De Roo, A. Carrete, M. Dimitrievska, A. Gencì, M. Meyns, A. Pérez-Rodríguez, M. V. Kovalenko, J. Arbiol, and A. Cabot, "Scalable Heating-Up Synthesis of Monodisperse Cu2ZnSnS4 Nanocrystals," *Chemistry of Materials*, vol. 28, no. 3, pp. 720–726, 2016.

[136] J. J. Scragg, T. Ericson, T. Kubart, M. Edoff, and C. Platzer-Björkman, "Chemical insights into the instability of Cu2ZnSnS4 films during annealing," *Chemistry of Materials*, vol. 23, no. 20, pp. 4625–4633, 2011.

[137] A. L. Patterson, "The Scherrer Formula for X-Ray Particle Size Determination," *Physical Review*, vol. 56, pp. 978–982, 1939.

[138] H. Zhou, W.-C. Hsu, H.-S. Duan, B. Bob, W. Yang, T.-B. Song, C.-J. Hsu, and Y. Yang, "CZTS nanocrystals: a promising approach for next generation thin film photovoltaics," *Energy & Environmental Science*, vol. 6, no. 10, pp. 2822–2838, 2013.

[139] P. Jalali and M. Li, "An estimate of random close packing density in monodisperse hard spheres," *Journal of Chemical Physics*, vol. 120, no. 2, pp. 1138–1139, 2004.

[140] G. D. Scott and D. M. Kilgour, "The density of random close packing of spheres," *Brit. J. Appl. Phys.*, vol. 2, no. 2, pp. 863–866, 1969.

[141] K. Lochmann, L. Oger, and D. Stoyan, "Statistical analysis of random sphere packings with variable radius distribution," *Solid State Sciences*, vol. 8, no. 12, pp. 1397–1413, 2006.

[142] A. R. Kansal, S. Torquato, and F. H. Stillinger, "Computer generation of dense polydisperse sphere packings," *Journal of Chemical Physics*, vol. 117, no. 18, pp. 8212–8218, 2002.

[143] M. Kauk, K. Muska, M. Altosaar, J. Raudoja, M. Pilvet, T. Varema, K. Timmo, and O. Volobujeva, "Effects of sulphur and tin disulphide vapour treatments of Cu2ZnSnS(Se)4 absorber materials for monograin solar cells," *Energy Procedia*, vol. 10, pp. 197–202, 2011.

[144] J. V. Embden, A. S. R. Chesman, E. D. Gaspera, N. W. Du, S. E. Watkins, and J. J. Jasieniak, "Cu2ZnSnS4xSe4(1-x) solar cells from polar nanocrystal inks," *J. Am. Chem. Soc.*, vol. 136, pp. 5237–5240, 2014.

[145] A. Carrete, A. Shavel, X. Fontané, J. Montserrat, J. Fan, M. Ibáñez, E. Saucedo, A. Pérez-Rodríguez, and A. Cabot, "Antimony-Based Ligand Exchange To Promote Crystallization in Spray-Deposited Cu2ZnSnSe4 Solar Cells," *Journal of the American Chemical Society*, vol. 135, no. 43, pp. 15982–15985, 2013.

[146] Y. Kim, K. Woo, I. Kim, Y. S. Cho, S. Jeong, and J. Moon, "Highly concentrated synthesis of copper-zinc-tin-sulfide nanocrystals with easily decomposable capping molecules for printed photovoltaic applications," *Nanoscale*, vol. 5, pp. 10183–10188, 2013.

[147] J. Zhou, L. You, S. Li, and Y. Yang, "Preparation and characterization of Cu2ZnSnS4 microparticles via a facile solution route," *Materials Letters*, vol. 81, pp. 248–250, 2012.

[148] D. Wang, Z. Jin, J. Wang, T. Liu, J. Li, and J. Lai, "Wet-chemical synthesis of quaternary chalcopyrite Cu(In1-xAlx)Se2 nanocrystals by triethylenetetramine- assisted triethylene glycol solution process," *Journal of Alloys and Compounds*, vol. 587, pp. 698–704, 2014.

[149] W. M. Haynes, ed., *CRC Handbook of Chemisty and Physics*. CRC Press, 97th ed.

[150] "Sigma Aldrich," 2017.

[151] X. Fontané, V. Izquierdo-Roca, E. Saucedo, S. Schorr, V. O. Yukhym-chuk, M. Y. Valakh, A. Pérez-Rodríguez, and J. R. Morante, "Vibrational properties of stannite and kesterite type compounds: Raman scattering analysis of Cu2(Fe,Zn)SnS4," *Journal of Alloys and Compounds*, vol. 539, pp. 190–194, 2012.

[152] D. Freedman and P. Diaconis, "On the histogram as a density estimator - L2 theory," *Zeitschrift für Wahrscheinlichkeitstheorie und Verwandte Gebiete*, vol. 57, no. 4, pp. 453–476, 1981.

[153] "Spectral Database for Organic Compounds."

[154] R. Dierick, B. Capon, H. Damm, S. Flamee, P. Arickx, E. Bruneel, D. Van Genechten, M. Van Bael, A. Hardy, C. Detavernier, and Z. Hens, "Annealing of sulfide stabilized colloidal semiconductor nanocrystals," *Journal of Materials Chemistry C*, vol. 2, no. 1, pp. 178–183, 2014.

[155] J. McMurry, *Organic Chemistry*. Thomson Learning, 6th ed., 2004.

[156] T. Martini, C. Chubilleau, O. Poncelet, A. Ricaud, A. Blayo, C. Martin, and K. Tarasov, "Spray and inkjet fabrication of Cu2ZnSnS4 thin films using nanoparticles derived from a continuous-flow microwave-assisted synthesis," *Solar Energy Materials and Solar Cells*, vol. 144, pp. 657–663, 2016.

[157] Y. Sun, K. Zong, H. Zheng, H. Wang, J. Liu, H. Yan, and M. Zhu, "Ethylene glycol-based dip coating route for the synthesis of Cu2ZnSnS4 thin film," *Materials Letters*, vol. 92, pp. 195–197, 2013.

[158] C. J. Brabec and J. R. Durrant, "Solution-Processed Organic Solar Cells," *MRS Bulletin*, vol. 33, no. July 2008, pp. 670–675, 2008.

[159] "Paasche Model VL Double Action Airbrush," 2017.

[160] V. T. Tiong, Y. Zhang, J. Bell, and H. Wang, "Carbon concentration dependent grain growth of Cu2ZnSnS4 thin films," *Rsc Advances*, vol. 5, no. 26, pp. 20178–20185, 2015.

[161] B. Derby, "Inkjet Printing of Functional and Structural Materials: Fluid Property Requirements, Feature Stability, and Resolution," *Annual Review of Materials Research*, vol. 40, no. 1, pp. 395–414, 2010.

[162] B. D. Chernomordik, A. E. Béland, D. D. Deng, L. F. Francis, and E. S. Aydil, "Microstructure Evolution and Crystal Growth in Cu2ZnSnS4 Thin Films Formed By Annealing Colloidal Nanocrystal Coatings," *Chemistry of Materials*, vol. 26, pp. 3191–3201, 2014.

[163] D. B. Mitzi, M. Yuan, W. Liu, A. J. Kellock, S. Jay Chey, V. Deline, and A. G. Schrott, "A high-efficiency solution-deposited thin-film photovoltaic device," *Advanced Materials*, vol. 20, no. 19, pp. 3657–3662, 2008.

[164] L. C. de Jonghe and M. N. Rahaman, "Sintering of Ceramics," in *Handbook of Advanced Ceramics* (S. Somiya, ed.), ch. 4, p. 187, Berkeley: Elsevir Inc., 2003.

[165] C. B. Carter and M. G. Norton, "Sintering and Grain Growth," in *Ceramic Materials: Science and Engineering* (C. B. Carter and M. G. Norton, eds.), ch. 24, pp. 427–443, New York: Springer, 1st ed., 2007.

[166] S. Delbos, "Kësterite thin films for photovoltaics : a review," *EPJ Photovoltaics*, vol. 3, p. 35004, 2012.

[167] A. Redinger, D. M. Berg, P. J. Dale, and S. Siebentritt, "The consequences of kesterite equilibria for efficient solar cells," *Journal of the American Chemical Society*, vol. 133, no. 10, pp. 3320–3323, 2011.

[168] Y. E. Romanyuk, C. M. Fella, A. R. Uhl, M. Werner, A. N. Tiwari, T. Schnabel, and E. Ahlswede, "Recent trends in direct solution coating of kesterite absorber layers in solar cells," *Solar Energy Materials and Solar Cells*, vol. 119, pp. 181–189, 2013.

[169] K. Tanaka, M. Oonuki, N. Moritake, and H. Uchiki, "Cu2ZnSnS4 thin film solar cells prepared by non-vacuum processing," *Solar Energy Materials and Solar Cells*, vol. 93, pp. 583–587, 2009.

[170] K. Maeda, K. Tanaka, Y. Fukui, and H. Uchiki, "Dependence on annealing temperature of properties of Cu2ZnSnS4 Thin films prepared by sol-gel sulfurization method," *Japanese Journal of Applied Physics*, vol. 50, no. 05FB08, pp. 1–4, 2011.

[171] K. Maeda, K. Tanaka, Y. Fukui, and H. Uchiki, "Influence of H2S concentration on the properties of Cu2ZnSnS4 thin films and solar cells prepared by sol-gel sulfurization," *Solar Energy Materials and Solar Cells*, vol. 95, no. 10, pp. 2855–2860, 2011.

[172] B. S. Pawar, S. M. Pawar, K. V. Gurav, S. W. Shin, J. Y. Lee, S. S. Kolekar, and J. H. Kim, "Effect of Annealing Atmosphere on the Properties of Electrochemically Deposited Cu2ZnSnS4 (CZTS) Thin Films," *ISRN Renewable Energy*, vol. 2011, no. 934575, pp. 1–5, 2011.

[173] Y. Cai, J. C. W. Ho, S. K. Batabyal, W. Liu, Y. Sun, S. G. Mhaisalkar, and L. H. Wong, "Nanoparticle-Induced Grain Growth of Carbon-Free Solution- Processed CuIn(S,Se)2 Solar Cell with 6% Efficiency," *ACS Applied Materials and Interfaces*, vol. 5, pp. 1533–1537, 2013.

[174] S. Ahn, K. Kim, A. Cho, J. Gwak, J. Ho, K. Shin, S. K. Ahn, and K. Yoon, "CuInSe2 (CIS) thin films prepared from amorphous Cu-In-Se nanoparticle precursors for solar cell application," *ACS Applied Materials and Interfaces*, vol. 4, pp. 1530–1536, 2012.

[175] Q. Zhang, M. Cao, J. S. Shen, J. Huang, Y. Zhao, Y. Sun, L. J. Wang, and Y. Shen, "Effect of the annealing conditions on the structural stability and photoelectrical properties of wurtzite structured Cu2ZnSnS4 nanoparticles," *Vacuum*, vol. 122, pp. 66–74, 2015.

[176] R. Klenk, T. Walter, H.-W. Schock, and D. Cahen, "A Model of the Successful Growth of Polycrystalline Films of CuInSe2 by Multisource Physical Vacuum Evaporation," *Advanced Materials*, vol. 5, no. 2, pp. 114–119, 1993.

[177] D. Braunger, D. Hariskos, G. Bilger, U. Rau, and H. W. Schock, "Influence of sodium on the growth of polycrystalline Cu(In,Ga)Se2 thin films," *Thin Solid Films*, vol. 362, pp. 161–166, 2000.

[178] M. Mousel, T. Schwarz, R. Djemour, T. P. Weiss, J. Sendler, J. C. Malaquias, A. Redinger, O. Cojocaru-Mirédin, P. P. Choi, and S. Siebentritt, "Cu-rich precursors improve kesterite solar cells," *Advanced Energy Materials*, vol. 4, no. 2, pp. 1–6, 2014.

[179] G. P. Bernardini and A. Catani, "The Cu-Se System," *Mineral. Deposita*, vol. 3, pp. 375–380, 1968.

[180] S. Ahn, K. H. Kim, J. H. Yun, and K. H. Yoon, "Effects of selenization conditions on densification of Cu(In,Ga)Se2 (CIGS) thin films prepared by spray deposition of CIGS nanoparticles," *Journal of Applied Physics*, vol. 105, no. 11, 2009.

[181] R. Scheer and H.-J. Lewerenz, "Formation of secondary phases in evaporated CuInS2 thin films: A surface analytical study," *Journal of Vacuum Science & Technology A: Vacuum, Surfaces, and Films*, vol. 13, no. 4, pp. 1924–1929, 1995.

[182] W. Xiao, J. Wang, X. Zhao, J. Wang, G. Huang, L. Cheng, L. Jiang, and L. Wang, "Intrinsic defects and Na doping in Cu2ZnSnS4: A density-functional theory study," *Solar Energy*, vol. 116, no. May, pp. 125–132, 2015.

[183] C. M. Sutter-Fella, J. a. Stückelberger, H. Hagendorfer, F. La Mattina, L. Kranz, S. Nishiwaki, A. R. Uhl, Y. E. Romanyuk, and A. N. Tiwari, "Sodium Assisted Sintering of Chalcogenides and Its Application to Solution Processed Cu2ZnSn(S,Se)4 Thin Film Solar Cells," *Chemistry of Materials*, vol. 26, no. 3, pp. 1420–1425, 2014.

[184] T. Abzieher, T. Schnabel, M. Hetterich, M. Powalla, and E. Ahlswede, "Source and effects of sodium in solution-processed kesterite solar cells," *Physica Status Solidi (A) Applications and Materials Science*, vol. 213, no. 4, pp. 1039–1049, 2016.

[185] H. Zhou, T.-B. Song, W.-C. Hsu, S. Luo, S. Ye, H.-S. Duan, C.-J. Hsu, W. Yang, and Y. Yang, "Rational Defect Passivation of Cu2ZnSn(S,Se)4 Photovoltaics with Solution-Processed Cu2ZnSnS4:Na Nanocrystals," *Journal of the American Chemical Society*, vol. 135, no. 43, pp. 15998–16001, 2013.

[186] H. Xin, S. M. Vorpahl, D. Collord, I. L. Braly, A. R. Uhl, B. W. Krueger, D. S. Ginger, and H. W. Hillhouse, "Lithium-doping inverts the nanoscale electric field at the grain boundaries in Cu2ZnSn(S,Se)4 and increases photovoltaic efficiency.," *Physical chemistry chemical physics : PCCP*, vol. 17, no. 37, pp. 23859–66, 2015.

[187] Q. Wen, Y. Li, J. Yan, and C. Wang, "Crystal size-controlled growth of Cu2ZnSnS4 films by optimizing the Na doping concentration," *Materials Letters*, vol. 140, pp. 16–19, 2015.

[188] J. Sangster and A. D. Pelton, "The Na-S (Sodium-Sulfur) System," *Phase Diagram Evaluations: Section II*, vol. 18, no. 1, pp. 89–96, 1997.

[189] J. Sangster and A. D. Pelton, "The Na-Se (Sodium-Selenium) System," *Phase Diagram Evaluations: Section II*, vol. 18, no. 2, pp. 185–189, 1997.

[190] R. Mainz, B. C. Walker, S. S. Schmidt, O. Zander, A. Weber, H. Rodriguez-Alvarez, J. Just, M. Klaus, R. Agrawal, and T. Unold, "Real-time observation of Cu2ZnSn(S,Se)4 solar cell absorber layer formation from nanoparticle precursors.," *Physical chemistry chemical physics : PCCP*, vol. 15, no. 41, pp. 18281–9, 2013.

[191] T. Prabhakar and N. Jampana, "Effect of sodium diffusion on the structural and electrical properties of Cu2ZnSnS4 thin films," *Solar Energy Materials and Solar Cells*, vol. 95, no. 3, pp. 1001–1004, 2011.

[192] M. Johnson, S. V. Baryshev, E. Thimsen, M. Manno, X. Zhang, I. V. Veryovkin, C. Leighton, and E. S. Aydil, "Alkali-metal-enhanced grain growth in Cu2ZnSnS4 thin films," *Energy Environ. Sci.*, vol. 7, no. 6, pp. 1931–1938, 2014.

[193] T. Schnabel, M. Löw, and E. Ahlswede, "Vacuum-free preparation of 7.5% efficient Cu2ZnSn(S,Se)4 solar cells based on metal salt precursors," *Solar Energy Materials and Solar Cells*, vol. 117, pp. 324–328, 2013.

[194] J. Sangster and A. D. Pelton, "The K-S (Potassium-Sulfur) System," *Phase Diagram Evaluations: Section II*, vol. 18, no. 1, pp. 82–88, 1997.

[195] J. Sangster and A. D. Pelton, "The Rb-S (Rubidium-Sulfur) System," *Phase Diagram Evaluations: Section II*, vol. 18, no. 1, pp. 97–100, 1997.

[196] J. Sangster and A. D. Pelton, "The Cs-S (Cesium-Sulfur) System," *Pha*, vol. 18, no. 1, pp. 78–81, 1997.

[197] Z. Tong, C. Yan, Z. Su, F. Zeng, J. Yang, Y. Li, L. Jiang, Y. Lai, and F. Liu, "Effects of potassium doping on solution processed kesterite Cu2ZnSnS4 thin film solar cells," *Applied Physics Letters*, vol. 105, no. 22, pp. 4–8, 2014.

[198] G. W. Neudeck, *The pn Junction Diode - Modular series on solid state devices, volume II*. W. Lafayette: Addison-Wesley Publishing Company, 2nd ed., 1989.

[199] S. M. Sze and K. K. Ng, *Physics of Semiconductor Devices*. John Wiley & Sons, Inc., 3rd ed., 2007.

[200] A. Crovetto, *Cu2ZnSnS4 solar cells: Physics and technology by alternative tracks*. PhD thesis, Technical University of Denmark, 2016.

[201] S. Rühle, "Tabulated values of the Shockley-Queisser limit for single junction solar cells," *Solar Energy*, vol. 130, pp. 139–147, 2016.

[202] C. Yan, F. Liu, K. Sun, N. Song, J. A. Stride, F. Zhou, X. Hao, and M. Green, "Boosting the ef fi ciency of pure sul fi de CZTS solar cells using the In/Cd-based hybrid buffers," *Solar Energy Materials and Solar Cells*, vol. 144, pp. 700–706, 2016.

[203] M. Grossberg, J. Krustok, J. Raudoja, and T. Raadik, "The role of structural properties on deep defect states in Cu2ZnSnS4 studied by photoluminescence spectroscopy," *Applied Physics Letters*, vol. 101, no. 2012, p. 102102, 2012.

[204] T. Gershon, Y. S. Lee, R. Mankad, O. Gunawan, T. Gokmen, D. Bishop, B. McCandless, and S. Guha, "The impact of sodium on the sub-bandgap states in CZTSe and CZTS," *Applied Physics Letters*, vol. 106, no. 12, p. 123905, 2015.

[205] R. B. Prime, H. E. Bair, S. Vyazovkin, P. K. Gallagher, and A. Riga, "Thermogravimetric analysis (TGA)," in *Thermal Analysis Of Polymers: Fundamentals And Applications* (J. D. Menczel and R. B. Prime, eds.), ch. 3, pp. 241–317, John Wiley & Sons, Inc, 1st ed., 2009.

[206] "National Institute of Standards and Technology," 2017.

[207] H. Park, Y. H. Hwang, and B. S. Bae, "Sol-gel processed Cu2ZnSnS4 thin films for a photovoltaic absorber layer without sulfurization," *Journal of Sol-Gel Science and Technology*, vol. 65, no. 1, pp. 23–27, 2013.

GANTT CHART OF PROJECT

All tasks include literature review, experiments, and characterization. All processes have been carried out continuously, but are displayed when they were the main objective of the work. The milestones were specified in the project description, and are coloured red when they were reached. A list of the milestone can be seen in Table A.1. This project was initiated in month 8 (M8).

Table A.1: Milestone defined from project description.

Month	Milestone
M8	Additional equipment purchased
M18	Conversion efficiency of cells of CZTS measured
M24	First films of CZTS produced with spray-coating at DTU Fotonik
M24	Conversion efficiency of CZTS films from spray-coating measured
M36	Production of CZTS films at Dansk Solenergi with spray-coating
M48	Possible prototype CZTS-cell produced with spray-coating at Dansk Solenergi ready with an efficiency > 4%

Quarters

1　2　3　4　5　6　7　8　9　10　11　12

Establishing experimental setup

Purchasing equipment

Additional equipment purchased

Finding available lab with fume hood

Setting up Schlenk line

Oven design, purchase and building

Synthesis

Ligand-coated CZTS

Ligand-coated CZTSe

Ligand-free CZTS

Deposition

First spray-coated films

Spray-coating at Dansk Solenergi

0% complete

Annealing

Ligand-coated CZTS

Ligand-free CZTS

Solar cells

Efficiency measured

Efficiency of spray-coated films

>4% prototype at Dansk Solenergi

TODAY

Considerations to determine particle size distribution

We compiled a list of considerations on how to obtain a representative size distribution:

- If particle aggregation is severe, larger particles tend to "hide" in the center of the aggregate, dark field and bright field images can help to measure these sizes in the thicker regions of the aggregate.
- Very small particles can stick to the surface of the larger particles, without being uncovered. Therefore, the size distribution might not be very accurate for sizes below 5 nm. However, these will also be washed out in the washing steps, and their presence is not crucial for the discussion here.
- The assumption that the particles are spherical should also be assessed. Most of the large CZTS particles were hexagonal, indicating this preferential growth direction. However, there is a possibility the particles are flat or somewhat else distorted, but we did not see any sign of this.
- It is important to collect images that each includes a representative size distribution of the particles.
- To observe the full particle size range, it was necessary to record images at different magnifications. For instance, small particles are observed by HRTEM. It should therefore be noted, that although representative images were aimed for, the particle size distribution will necessarily be biased by the number of recorded images at each magnification.

APPENDIX C

THERMOGRAVIMETRIC AND DIFFERENTIAL THERMAL ANALYSIS

In this appendix, relevant considerations on choosing the correct experimental conditions for TGA and DTA analysis are described. In addition, check-up on the temperature accuracy and calibration of the heat flow is also presented. Part of this appendix was used for a report in a course (47314 Thermal Analysis - Experimental Course). Finally, the DTA results are shown.

EXPERIMENTAL CONSIDERATIONS

The STG analysis was carried out on a Netzsch STA 409CD, which can measure from room temperature to 1500°C, with a range of 5 g, resolution of 1 μg and enthalpy precision of ± 3 %. There are many factors to consider when choosing the right experimental conditions for a measurement, [205]. In the following, the most important ones are covered.

- **Crucible:** It is important that the crucible chosen is compatible with the sample material and temperature profile, to avoid reaction with the sample or volatile species from the sample, and melting of the crucible. Corundum (Al_2O_3) crucibles are suitable for organic materials and metals, whereas platinum crucibles are not recommended for metals and reducing atmospheres. Since there might be some metal phases in the CZTS nanoparticles, and since reducing gases would be used, corundum crucibles were chosen. For powder samples no lid was used, as it allows better contact to the reaction gas, and for liquid samples a lid would limit fast evaporation of solvents to a certain amount and ensure a better heat distribution inside the crucible. However, the lid was pierced to avoid

pressure build-up of the evolved gases. The thermal conductivity of the crucible would influence the signal, and Al_2O_3 has a larger time constant than metals, which produces broader peaks, but Al_2O_3 should be sufficient for this purpose.

- **Atmosphere:** Oxidizing (air), inert (N_2), and reducing (4.5% H_2 in Ar, also called *forming gas*) atmospheres were chosen for the experiments. Among these, care should be taken when working with reducing atmosphere, as it can be toxic and flammable. In our case, when annealing sulfides, the possibility exists of forming hydrogen sulfide which is a very toxic gas. These atmospheres all have similar gas densities, and only one baseline was necessary per measurement. The flow rate was chosen to be 100 ml/min as is standard, and this should be high enough to avoid condensation of gases on cooler parts of the suspension and to avoid risking to suck air in from the outside, and still low enough not to disturb the normal laminar flow around the sample stage.

- **Temperature profile:** The starting temperature should be $50°C$ before the first thermal event in an ideal caseq, and the final temperature should be $50°C$ after the last thermal event, for the temperature, gas flow *etc.* to stabilize. The STA 409CD cannot go lower than room temperature, and therefore the starting temperature was set to this. The heating rate was chosen to be similar to the heating rate used in typical annealing processes, *i.e.* 12 K/min. Isothermal steps were also carried out to exactly copy the annealing done in practice. The cooling rate was set to the same as the heating rate for comparison.

- **Sample preparation:** The sample mass should be similar when comparing two experiments, as a low mass will have a higher resolution but lower DTA signal than a high mass. For high mass samples, the heat distribution would take time, and this would smear out the kinetics, and thus give lower resolution, but the signal will increase and provide a better signal-to-noise ratio. When preparing the sample, it is also very important that there is a good contact between the sample and the crucible, for a good thermal contact to the sample and to ensure that the thermocouple is precise. Finally, the crucible position inside the chamber is important for reproducibility.

Baselines were measured in order to account for external factors affecting the measurement. One example of a such is the buoyancy effect, which accounts for decrease in the density of the atmosphere in the instrument as temperature increases, and therefore also the mass increases of the measured sample. Once the baseline scans were done, sample masses of between 10 and 25 mg were weighed and placed in the sample crucible, and the measurement was started.

The data was analysed with the Proteus61 software. First, it was checked that the flow was stable, and then the curve was evaluated according to any interesting properties.

Calibration of temperature and heat flow

It is necessary to calibrate the temperature and heat flow regularly, and to determine whether a temperature calibration was required, the temperature accuracy was checked with a few melting point standards. The chosen ones were KNO_3, $KClO_4$, and Ag_2SO_4 from the NIST-ICTA reference materials, as these materials have melting points at $128°C$, $299°C$, and $424°C$, respectively, and covers the region of interest for these experiments. Melting point standards are convenient as the signal response is significant and reproducible and they resemble the samples used here. An example of how the onset temperature and peak area are determined is showed in Fig. C.1. As can be seen from Table C.1, the measured temperatures were within the tolerance of the instrument, and no calibration will be carried out.
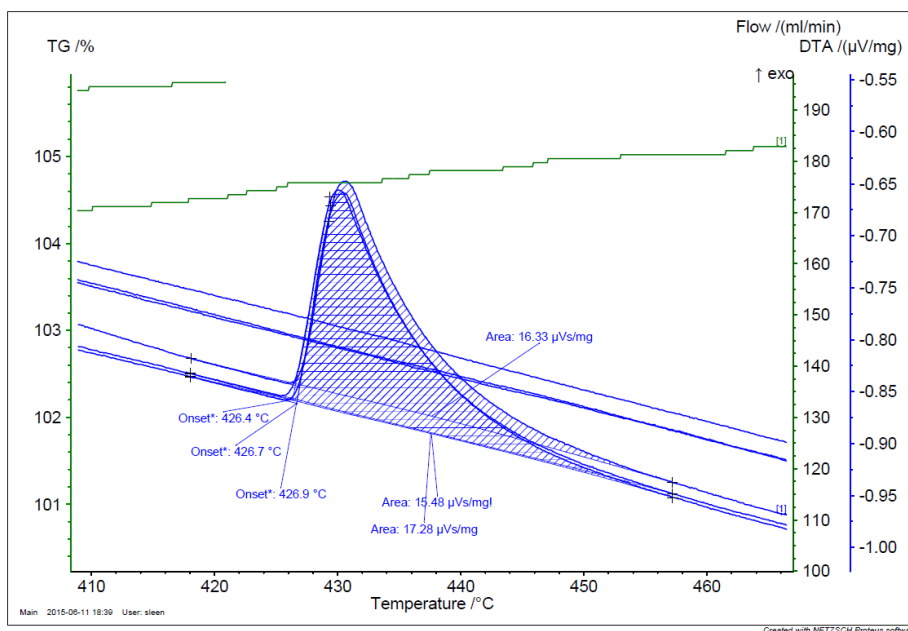
Figure C.1: Example of calibration measurements on melting point standards, here Ag_2SO_4. Three measurements were carried out, and the temperature was determined as an average of the extrapolated onset, and the peak with a Belzier baseline.

Similarly, the heat flow can be deduced from the area under the peak in the

Table C.1: Temperature check in relevant temperature region with three melting point standards. T_m is the literature value, and $T_{ex.ons.}$ the extrapolated onset from the measurement. The difference is found to be accepted for this purpose.

Melting point standard	T_m (°C)	$T_{ex.ons.}$ (°C)	T_m -$T_{ex.ons.}$ (°C)
KNO_3	128	129	-1
$KClO_4$	299	300	-1
Ag_2SO_4	424	427	-3

DTA curve. The heat of fusion, or melting enthaply, ΔH, can be found from literature, and a calibration faction, $K(T)$, can be determined from the following relation

$$\Delta H = K(T) \cdot A \qquad (C.1)$$

where the peak area, A, is calculated from the DTA curve. The peak area of the second and third curves was calculated with a Bezier baseline, and can be seen in Table C.2. The Bezier baseline is proper to use when the curve have similar curvature before and after the thermal event, *i.e.* no changes in the specific heat capacity during the melting process.

Table C.2: The calibration factor was calculated from the melting point peak area for the three standard materials for different melting enthalpies (heat of fusion) found in literature. The values marked in bold are believed to be the correct melting enthalpies and corresponding calibration factors as they seem to match the measurements done here best.

Melting point standard	Enthaply (J/g)	Peak area (µVs/mg)	Calibration factor (kA)
KNO_3	95.0[149]/**50.4[206]**/25.1[206]	18.4	5.16/**2.74**/1.36
$KClO_4$	**100.5[206]**	37.1	**2.71**
Ag_2SO_4	57.7[149]/**51.7[206]**	16.4	3.52/**3.15**

The enthalpy values from literature vary, as some account for melting and some for crystallization, but the believed melting enthalpies are marked in bold, as they resemble the measurements done here the most. A calibration factor around $K(T) = 3$ should therefore be appropriate. Any variations in the measured enthalpy can result from many factors, but the crucible position inside the chamber is a main one.
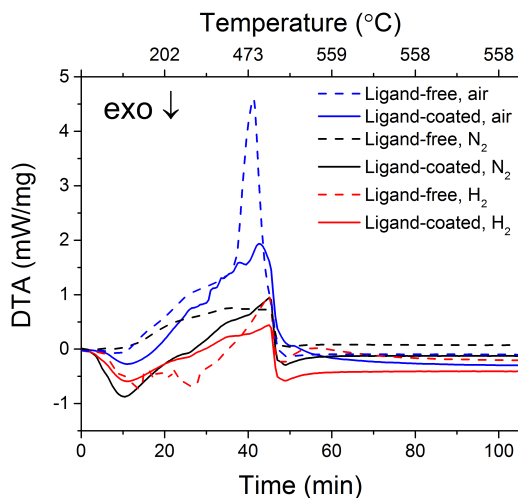
Figure C.2: DTA curves for ligand-coated and ligand-free nanoparticle powders in different atmosphere. The temperature increases with 12 K/min until 560°C, where the temperature is kept for 1 h.

RESULTS

DTA measures the temperature difference between the sample and a reference sample, and can tell us whether a reaction is endothermic or exothermic. A comparison of the different atmospheres is displayed in Fig. C.2 for the two types of nanoparticle powders. All sample masses were between 16 mg and 21 mg, so no large variation in DTA signal should stem from this. The DTA measurement indicates an endothermic reaction initially for all atmospheres, *e.g.* thermal decomposition of organic material or vaporization (water evaporation). Once the heat-up phase is complete, the DTA signals return to approx. 0 mW/mg, and no heat flow is detected throughout the isothermal step. Crystallization would be detected as an exothermic peak, and as would oxidation, of which there are no signs here. The DTA curves are rather similar for the two types of particles. The initial phase is uncertain, as the system needs to stabilize, and should not be considered. In the literature, differential scanning calorimetry (DSC) measurements have been done on sol-gel solutions, where an endothermic peak was seen initially, followed by an exothermic peak indicative of crystallization [207].
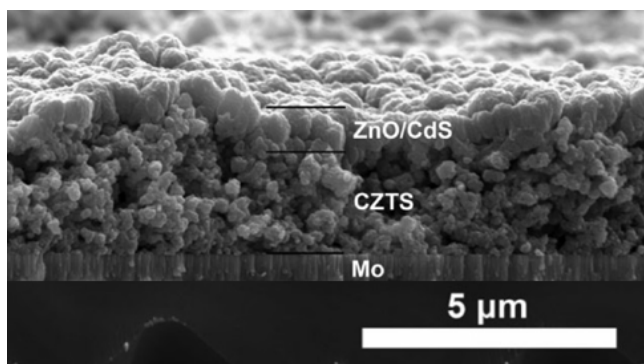
SEM MICROGRAPHS OF CZTS NANOPARTICLE SOLAR CELLS
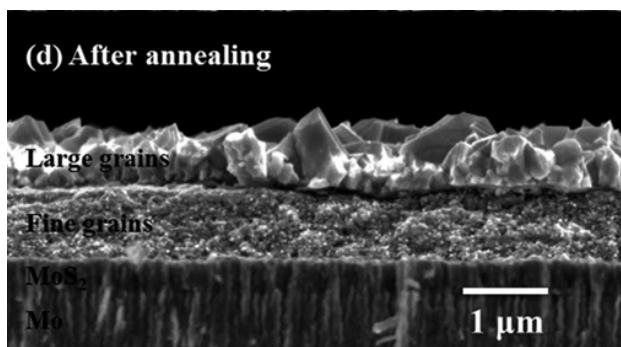
(a) Liu *et al.* [31]
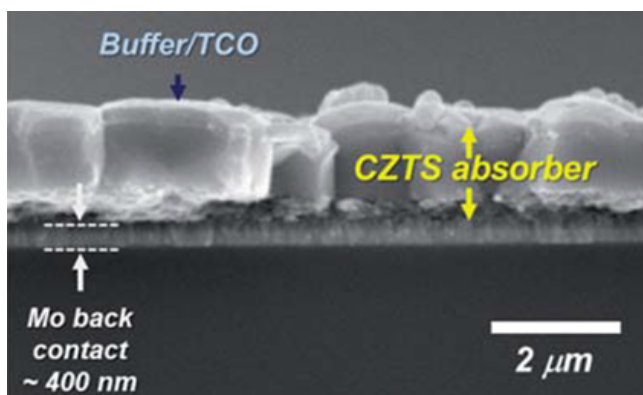
(b) Kim *et al.* [146]

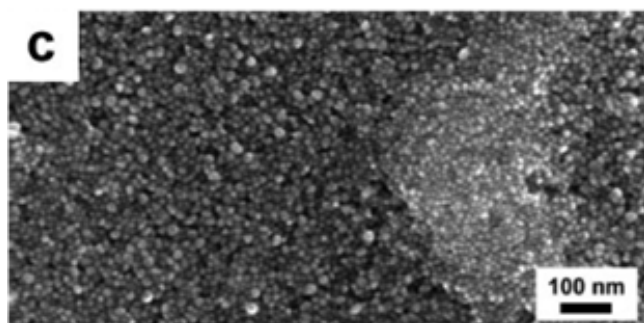**Figure D.1:** SEM micrographs of CZTS nanoparticle solar cell cross-sections.
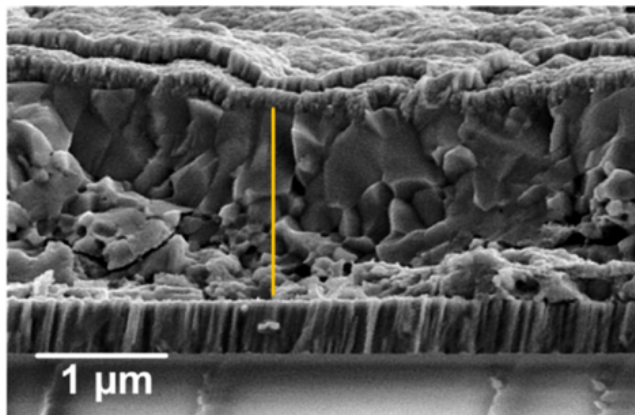
(a) Mkawi *et al.* [29]
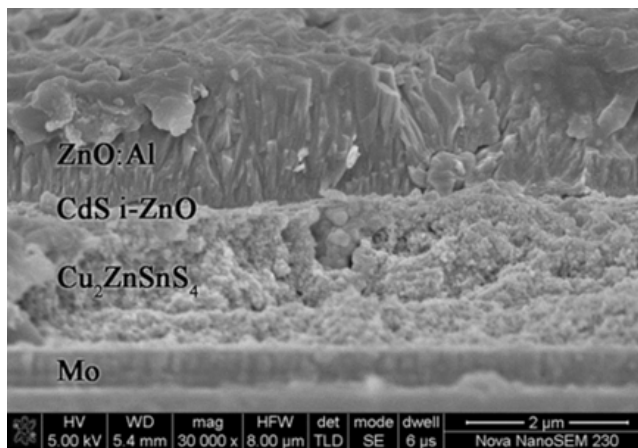
(b) Gu *et al.* [28]

Figure D.2: SEM micrographs of CZTS nanoparticle solar cell cross-sections.
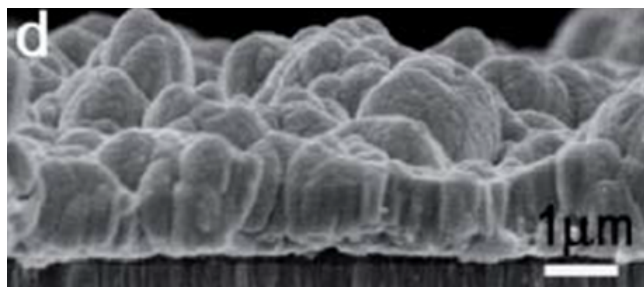
(a) Tian *et al.* [30]

(b) Flynn *et al.* [97]

(c) Steinhagen *et al.* [26]

Figure D.3: SEM micrographs of CZTS nanoparticle solar cell cross-section (and top surface for (d)).

APPENDIX E

ANNEALING OF LIGAND-COATED CZTS NANOPARTICLE THIN FILMS

In this appendix, SEM images and selected XRD pattern for ligand-coated CZTS films annealed under different conditions will be presented. The annealing conditions investigated were: amount of sulfur in graphite box, annealing time, and background pressure.

The effect of adding different *amount of sulfur* into the graphite box during annealing can be seen in the SEM images in Fig. E.1. Large grains grow on top of the film, and no grain growth is detected within the films (Fig. E.1(b)). The triangular grains on the 0 mg S film are likely a different phase. Sn-S is known to grow as plates, but according to the EDX and XRD measurements, they could also be ZnS. No clear difference can be seen between the various S-amounts, but the largest grains appeared when adding 100 mg S, so all future annealings used this amount. The sulfur content in the film was found not to vary with the amount of sulfur in the graphite box (Table E.1). The XRD patterns for some of the corresponding films shows the desired CZTS phase for all samples except the 0 mg S samples (Fig. E.2(a)).

The influence on *annealing time* can be seen in Fig. E.3. Again, grains are seen to grow on top of the surface. It is difficult to estimate from these images, whether more grain growth occurred for longer annealing times. Cracks in the film could be detrimental to a solar cell, but we see here that if the cracks are around 1 µm, CZTS grains can grow inside them and fill out the voids.

Finally, the *background pressure* was also investigated, and again grains were seen on the surface (Fig. E.4).
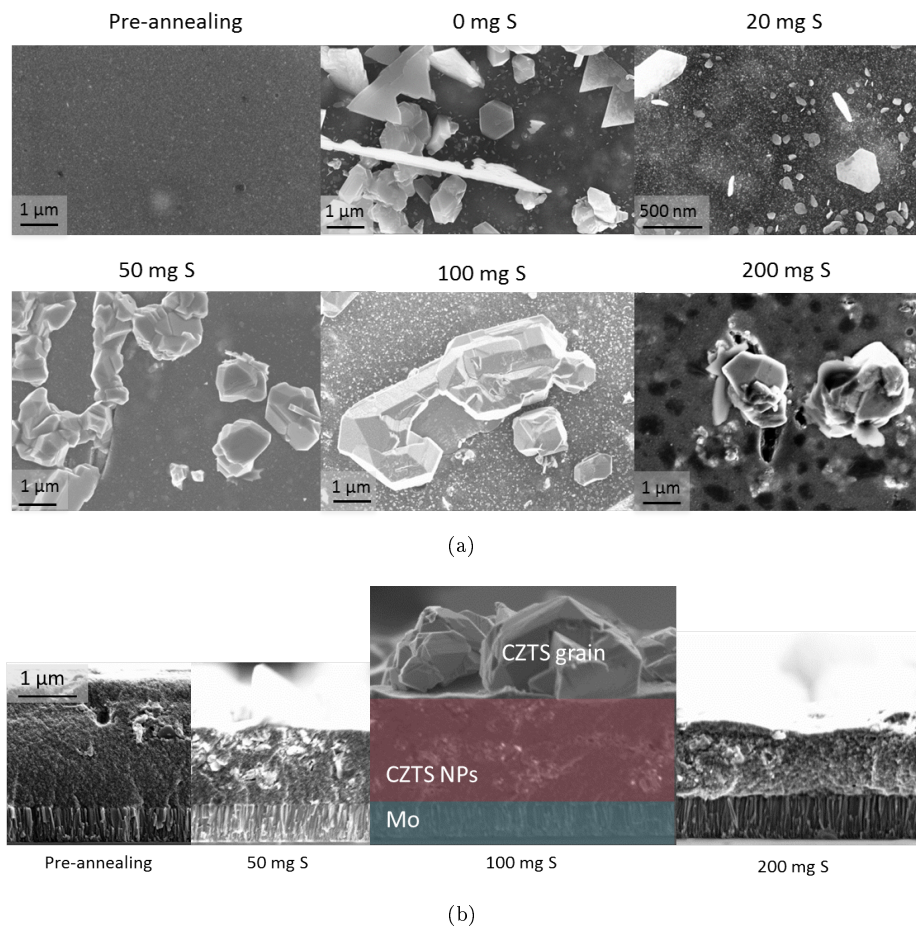
(a)

(b)

Figure E.1: Top view (a) and cross-section (b) micrographs of ligand-coated films annealed at 550°C for 30 min with different amount of S powder in the graphite box. Images acquired by Andrea Crovetto.
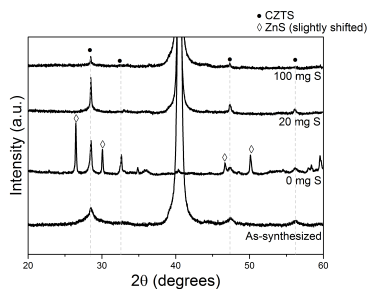
Figure E.2: XRD patterns of different amount of sulfur in the graphite box. The CZTS phase was the only identified phase on all samples, except the 0 mg S sample.
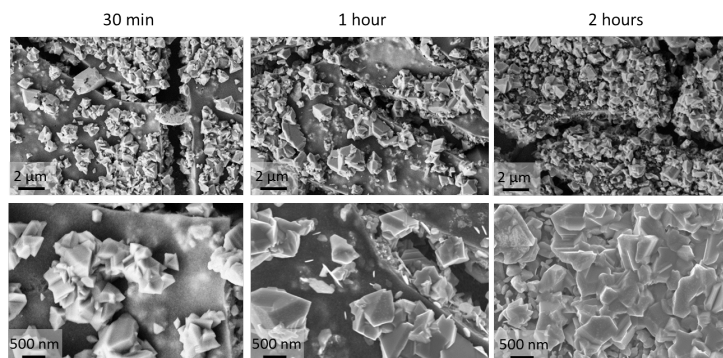

Figure E.3: Top view micrographs of ligand-coated films annealed at $550°C$ with 100 mg S for different annealing times. Images acquired by Andrea Crovetto.
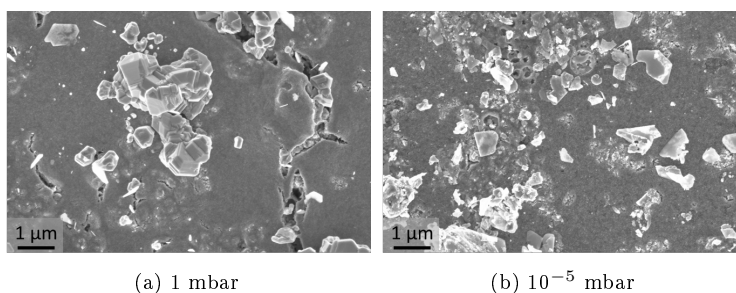

(a) 1 mbar   (b) 10^{-5} mbar

Figure E.4: Top view SEM micrographs for ligand-coated nanoparticle films annealed under different background pressure, with (a) 1 mbar, and (b) 10^{-5} mbar. Samples are annealed at $550°C$ for 30 min with 100 mg of S powder in the graphite box. Images acquired by Andrea Crovetto.

Table E.1:   Composition for samples annealed with different amounts of S added in the graphite box.

Sample	Cu/(Zn+Sn)	Zn/Sn	S (%)
As-synthesized	0.67	1.57	48.2
0 mg S	0.63	2.54	53.9
20 mg S	0.6	1.96	53.6
50 mg S	0.63	2.07	54.3
100 mg S	0.70	1.75	53.3
200 mg S	0.72	2.28	57.4